


Spring 1-1-2015

Application of the Na-DEMOF Atomic Filter to 3-Frequency Na Doppler Lidar Observations of Wind and Temperature in the Lower Atmosphere

Ian Forest Barry

University of Colorado Boulder, ian.barry@colorado.edu

Follow this and additional works at: https://scholar.colorado.edu/asen_gradetds

 Part of the [Atmospheric Sciences Commons](#), [Remote Sensing Commons](#), and the [Systems Engineering and Multidisciplinary Design Optimization Commons](#)

Recommended Citation

Barry, Ian Forest, "Application of the Na-DEMOF Atomic Filter to 3-Frequency Na Doppler Lidar Observations of Wind and Temperature in the Lower Atmosphere" (2015). *Aerospace Engineering Sciences Graduate Theses & Dissertations*. 126.
https://scholar.colorado.edu/asen_gradetds/126

This Thesis is brought to you for free and open access by Aerospace Engineering Sciences at CU Scholar. It has been accepted for inclusion in Aerospace Engineering Sciences Graduate Theses & Dissertations by an authorized administrator of CU Scholar. For more information, please contact cuscholaradmin@colorado.edu.

**Application of the Na-DEMOF Atomic Filter to
3-Frequency Na Doppler Lidar Observations of Wind and
Temperature in the Lower Atmosphere**

by

Ian Barry

B.S., University of Colorado Boulder, (Expected 2015)

A thesis submitted to the
Faculty of the Graduate School of the
University of Colorado in partial fulfillment
of the requirements for the degree of
Master of Science
Department of Aerospace Engineering Sciences
2015

This thesis entitled:
Application of the Na-DEMOF Atomic Filter to 3-Frequency Na Doppler Lidar Observations of
Wind and Temperature in the Lower Atmosphere
written by Ian Barry
has been approved for the Department of Aerospace Engineering Sciences

Xinzhao Chu

Dr. Wentao Huang

Dr. Zoltan Sternovsky

Date _____

The final copy of this thesis has been examined by the signatories, and we find that both the content and the form meet acceptable presentation standards of scholarly work in the above mentioned discipline.

Barry, Ian (MS, Aerospace Engineering Sciences)

Application of the Na-DEMOf Atomic Filter to 3-Frequency Na Doppler Lidar Observations of
Wind and Temperature in the Lower Atmosphere

Thesis directed by Prof. Xinzhao Chu

Lidar systems comprise one of several indispensable tools for derivation of wind, density, and temperature profiles in the atmosphere. 3-frequency resonance-fluorescence lidars are particularly useful for high-resolution profiles of all three quantities derived simultaneously. However, these lidars depend on atomic species restricted to the metal layers in the middle and upper atmosphere as frequency discriminators, and are not optimized for derivation of these quantities in the lower atmosphere. Rayleigh Doppler lidars typically applied to this region face other restrictions, such as dependence on high-power transmitted lasers, lack of absolute frequency references, and inability to derive multiple atmospheric quantities simultaneously without expensive additional transmitter and receiver channels.

A proposed solution to these difficulties is the sodium double-edge magneto-optic filter, (Na-DEMOf), which provides a frequency discriminator for the Rayleigh signal returned by the lower atmosphere and allows 3-frequency Na Doppler lidars to derive atmospheric quantity profiles within the lower atmosphere as well as within the mesospheric and lower thermospheric (MLT) metal layers.

This thesis describes the design, benefits, and restrictions of Na-DEMOfs, and uses the application methods and most recent results of the Na-DEMOfs constructed and tested by the Chu lidar group to demonstrate their successful application to simultaneous derivation of meridional and zonal winds along with temperature.

Acknowledgements

The guidance and encouragement of my advisor, Prof. Xinzhao Chu, has been indispensable throughout my graduate career at CU Boulder. I would also like to thank her for giving me the opportunity to join her research group during my undergraduate years, despite the complexity of our research and time conflicts between the course load of undergraduate work and research.

Dr. Wentao Huang has had a similarly inestimable impact on my research. I would not have been able to write this thesis without his help. Thank you also to Dr. John A. Smith for his help with everything from manufacturing and data acquisition to amateur astronomy. I would like to thank Cao "Chris" Chen, Xian Lu, Zhibin Yu, Jian Zhao, and Weichun Fong for their advice on operating the lidar, processing data, and graduate studies in general.

I would also like to thank Matt Rhode, Trudy Schwartz and the students working in the CU AES machine shop for their help in manufacturing cell ovens moving and cleaning lidar equipment. I would like to acknowledge the support of the CEDAR grant AGS 1042257 and CRRL/CTC grant 1136272 from the National Science Foundation, which allowed for this work to occur.

Finally, thank you to my family and friends, who supported me in every way they could, and I am very grateful for their places in my life.

Contents

Chapter	
1	Introduction 1
1.1	Motivations 1
1.2	Previous Work 2
1.3	Component Overview 3
2	Spectroscopy and Theoretical Formulation 6
2.1	Operating Concepts 6
2.1.1	Effects of External Magnetic Field on Complex Refractive Index 6
2.1.2	Resonance-Fluorescence and Rayleigh Lidars 9
2.2	DEMOF Theoretical Formulation 11
2.2.1	Temperature and Wind Uncertainties 14
2.3	IDL Simulations 15
2.4	Practical Considerations and Limitations 18
3	Detailed Design 19
3.1	Optics 19
3.2	Vapor Cell Oven and Housing 22
3.3	Heating Electronics 22
4	Calibration and Data Acquisition 25
4.1	Filter Function Measurement 25

4.1.1	Instrumentation and Setup	25
4.1.2	Procedure	27
4.1.3	Filter Function Processing	28
4.2	Data Acquisition	29
4.3	Nightly Calibration	34
5	Data Processing Scheme	36
5.1	STAR Lidar Data Pre-Processing	36
5.2	DEMOF-Specific Temperature and Wind Derivation	38
6	Results and Analysis	40
6.1	Results Obtained from 6/9/2015	41
6.1.1	30-Minute Temperature Profiles	42
6.1.2	30-Minute Wind Profiles	42
6.1.3	4.5-Hour Integrated Profiles	42
6.2	Results Obtained from 7/26/2015	47
6.2.1	30-Minute Temperature Profiles	47
6.2.2	30-Minute Wind Profiles	47
6.2.3	2.5-Hour Integrated Profiles	47
6.3	Results Obtained from 8/5/2015	52
6.3.1	30-Minute Temperature Profiles	52
6.3.2	30-Minute Wind Profiles	52
6.3.3	7-Hour Integrated Profiles	52
6.4	Simulation of Background Effects	57
6.5	Analysis	65
7	Conclusions	66
7.1	Effectiveness of DEMOF Atomic Filter	66

7.2 Remaining Challenges and Recommendations	67
7.3 Future Outlook	68
Bibliography	70
Appendix	
A Additional Error Simulation Results	72
B Off-Zenith Beam Alignment	79
C IDL Simulation Code	88

Tables

Table

4.1	Calibration Configuration Table	28
4.2	Receiver Calibration Constant Table	35
B.1	Beam Pointing Table	83

Figures

Figure

1.1	Simple DEMOF Setup	3
2.1	DEMOF Operating Principle	7
2.2	Example Calibration Mesh	13
2.3	Theoretical Na-DEMOF Transmission Spectrum	16
2.4	Zoomed Theoretical Na-DEMOF Transmission Spectrum	17
3.1	DEMOF Setup	20
3.2	DEMOF Housing	23
3.3	Vapor Cell Electronics	24
4.1	DEMOF Calibration Setup	26
4.2	Filter Functions Obtained on July 10, 2015	30
4.3	Full Na-DEMOF Receiver Configuration	31
4.4	Example Raw Photon Count Profile	33
5.1	Processing Scheme Flowchart	37
5.2	Use of Calibration Mesh	38
6.1	Cell 1 Temperature 6/9	42
6.2	Cell 2 Temperature 6/9	43
6.3	Cell 1 Wind 6/9	43

6.4	Cell 2 Wind 6/9	44
6.5	Cell 1 TW 6/9	44
6.6	Cell 2 TW 6/9	45
6.7	Cell 1 Temperature 7/26	47
6.8	Cell 2 Temperature 7/26	48
6.9	Cell 1 Wind 7/26	48
6.10	Cell 2 Wind 7/26	49
6.11	Cell 1 TW 7/26	49
6.12	Cell 2 TW 7/26	50
6.13	Cell 1 Temperature 8/5	52
6.14	Cell 2 Temperature 8/5	53
6.15	Cell 1 Wind 8/5	53
6.16	Cell 2 Wind 8/5	54
6.17	Cell 1 TW 8/5	54
6.18	Cell 2 TW 8/5	55
6.19	Raw Count Sim	58
6.20	Raw Ratio Sim	59
6.21	Integrated Count Sim	60
6.22	Integrated Ratio Sim	61
6.23	Smooth Count Sim	62
6.24	Smooth Ratio Sim	63
6.25	Real Ratios	64
A.1	Raw Count Sim	73
A.2	Raw Ratio Sim	74
A.3	Integrated Count Sim	75
A.4	Integrated Ratio Sim	76

A.5 Smooth Count Sim	77
A.6 Smooth Ratio Sim	78
B.1 Northward Beam Photograph	80
B.2 Westward Beam Photograph	81
B.3 Northward Star Field	81
B.4 Westward Star Field	82
B.5 Northward Beam Pointing Determination	84
B.6 Westward Beam Pointing Determination	85
B.7 Northward Beam Star Field Drift	85
B.8 Westward Beam Star Field Drift	86
B.9 Westward Beam Width Measurement	86

Chapter 1

Introduction

The goal of this thesis is to describe and evaluate the application of the sodium double-edge magneto-optic filter (Na-DEMOf) atomic filters to collection of atmospheric wind and temperature data in the lower atmosphere using resonance- fluorescence Doppler lidars which are designed for application to the metal layer present in the mesospheric and lower thermospheric (MLT) region. The Na-DEMOf was developed for the Chu lidar group's Student Training and Atmospheric Research (STAR) lidar. The design of the Na-DEMOf and results obtained from its application to three full nights of data collection will be discussed.

1.1 Motivations

Derivation of temperature and wind profiles from the stratosphere into the mesosphere are not unprecedented. Other techniques, such as interferometry and edge filters based on Fabry-Perot interferometers (FPIs), have also demonstrated the capability of measuring stratospheric winds [4][11][14]. Stratospheric temperatures have been measured extensively with Rayleigh lidars [10][17] and at even lower altitudes with Raman lidars [2]. These data have been instrumental in characterizing the effects of gravity wave breaking on general circulation through the middle atmosphere and gravity wave excitation sources from the lower atmosphere [18]. These systems generally require multiple instruments in order to measure both temperature and wind profiles.

However, the Na-DEMOf is unique in its ability to supplement an existing resonance-fluorescence lidar, allowing for derivation of wind and temperature profiles in both the lower atmo-

sphere and MLT region simultaneously. Additionally, resonance-fluorescence lidars generally have lower shot power and different transmitted wavelengths than the Rayleigh Doppler lidars that use interferometry or other edge filters to obtain the same profiles. These Rayleigh Doppler lidars often use bright green lasers with average powers of over 10 W, which can involve more eye safety concerns than resonance-fluorescence lidars operating at less than 500 mW at various optical wavelengths. The use of a resonance-fluorescence lidar also allows for more precise and stable laser wavelength locking, through the use of Doppler-free spectroscopy or similar spectroscopic methods which can be applied at resonant wavelengths. Finally, the three-frequency Na Doppler lidar to which the Na-DEMOF was applied for the purposes of this thesis allows for simultaneous derivation of wind and temperature profiles with the same lidar system, whereas previous techniques have required separate wind and temperature lidar channels [2], which can be costly and difficult to maintain.[8]

In order to achieve reasonable wind and temperature profiles using Na-DEMOFs, it is important to prove the stability of the double-edge filter functions achieved, as the radiosonde and MSIS data used for calibration are only available at low resolutions and can only be relied upon for nightly calibrations, rather than on the 30-minute intervals that would be required for calibration of each integrated temperature and wind profile under the methods used here. It is also important to ensure that the calibration constants obtained are independent of altitude, as altitude dependence would indicate unaccounted effects in addition to the unavoidably uneven optical setups between channels, which would imply an incomplete understanding of the return signals and reduce trust in the derived results.

1.2 Previous Work

As mentioned in Section 1.1, separate measurements of stratospheric temperature and wind profiles have been accomplished through various methods [2][4][10][11][14][17], including Mach-Zehnder interferometry for the downward extension of wind measurements obtained using the advanced Fe Doppler lidar [16]. However, simultaneous derivation with a single instrument is so far limited to the Na-DEMOF developed by the Chu lidar group at the University of Colorado

Boulder [8]. Double-edge vapor-cell filters like the Na-DEMOf provide greater stability than many interferometers due to the inherent frequency dependence of the vapor cells. Additionally, past comparisons of wind measurements by various edge filters have shown that double-edge vapor filters result in lower wind uncertainties than FPI-based edge filters [14].

Magneto-optic filters themselves have found other applications as narrow-bandwidth filters for solar imaging [1] or for background reduction in daytime lidar observations [6] and as Na Doppler nightglow analyzers [19]. The Chu lidar group has constructed multiple Na-DEMOfs as well as a Faraday anomalous dispersion filter for use in conjunction with the group's existing STAR Na Doppler resonance-fluorescence lidar. The theory behind transmission through heated Na vapor cells is understood well enough to simulate both of these kinds of filters [7]. Improvements to the STAR receiver [15] and Na-DEMOf data retrieval algorithm [5] have allowed for past measurements of temperature and vertical winds extending from 10-45 km.

1.3 Component Overview

A detailed description of this setup will be provided in Chapter 3. However, it is useful to introduce the key components here for ease of discussion.

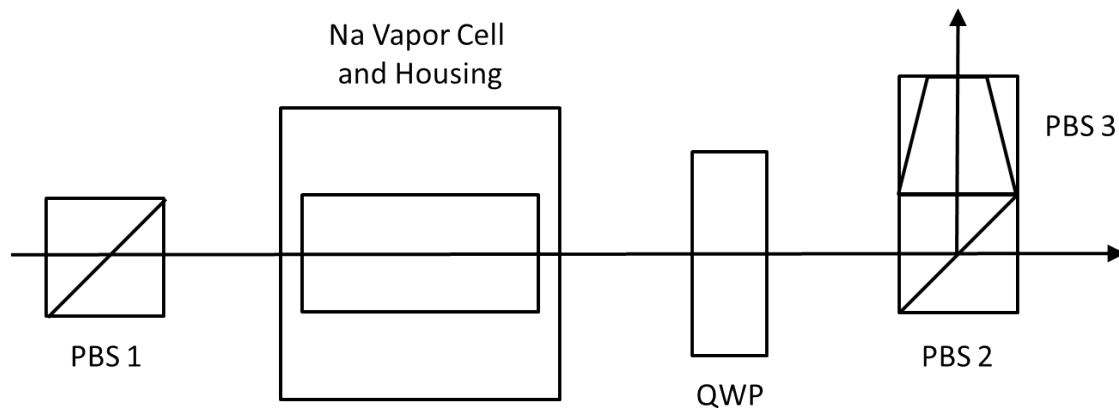


Figure 1.1: A simplified diagram of the optical setup of the Na-DEMOf. The beam conditioning optics and light transducers have been removed in order to display only the components which are specific to the Na-DEMOf and affect polarization and frequency-dependent transmission.

Use of the Na-DEMOF requires no change to the transmitter portion of the three-frequency Na Doppler lidar capable of transmitting three different frequencies of laser centered on the Na D2a peak, in the zenith direction, 20° off zenith toward the North and West, or in all three directions simultaneously. The three frequencies of laser light are transmitted in subsequent thirds of a three-second acquisition time for each stored photon count profile, meaning that only one frequency is transmitted at one time but the collection of profiles using each frequency is effectively simultaneous on the scale of the 30-minute integration windows used for Na-DEMOF wind and temperature profile derivation.

The incorporation of the Na-DEMOF into the receiver of the Na Doppler lidar requires more extensive modifications, in order to collect four different channels of photon counts passed through various paths of the Na-DEMOF setup. A diagram of the Na-DEMOF itself is shown in Figure 1.1, with more detailed optical layout provided in Figure 3.1. Each Na-DEMOF consists of a Na vapor cell, a quarter-wave plate (QWP) following the vapor cell, collimating optics and one polarizing beam splitter (PBS) before the vapor cell, two PBSs and focusing optics after the QWP, and two photomultiplier tubes (PMTs) for collecting photon count profiles. Before the collimating optics are a mechanical chopper, optical fiber holder, optical fiber, and light collecting Dobsonian telescope which are common to both the Na-DEMOF and the normal STAR lidar configurations. Because the current Na-DEMOF is intended for derivation of both meridional and zonal wind profiles, two receiving Na-DEMOF setups are used, including two telescopes, fibers, and vapor cells. The mechanical chopper is shared between the two optical setups, in order to ensure accurate timing for all received data collection. The rotation of the chopper, which cuts out high-intensity low-altitude light that would otherwise saturate the PMTs and interfere with higher altitude measurements, activates an electrical signal that is used to trigger the Na Doppler lidar's transmitted pulses and the start of data collection.

The vapor cell and QWP absorb the incoming photons in a way that allows for their use as a double-edge filter, with each edge acting on a different polarization component of the received light. The PBS preceding the vapor cell polarizes this light so that it can be reliably decomposed

into two orthogonal polarization components by the two PBSs following the QWP. The third of these PBSs acts only to clean up the polarization component transmitted by the second PBS, as the reflected component can have some leaked remnants of the transmitted component. Each of the two PMTs collects a separate component of this polarization, which effectively results in independent collection of the same received light passed through two frequency-dependent filters. The collimating and focusing optics are based on John Smith's ZEMAX-aided receiver design for minimizing the light lost after exiting the optical fiber, passing through the filter in a column, and being focused onto the aperture of the PMTs[15].

Chapter 2

Spectroscopy and Theoretical Formulation

This chapter discusses the concepts which govern the operation of the sodium double-edge magneto-optic filter (Na-DEMOF). A conceptual description of the spectroscopic effects involved and the resonance fluorescence lidar to which they are applied will be followed by the detailed analytical theory of the filter, and a summary of the computational algorithm used to approximate the theoretical behavior. The chapter concludes with a discussion of the limitations of the theory presented here.

2.1 Operating Concepts

The section provides an explanation of the optical behavior of the DEMOF, and describes the operation of a resonance-fluorescence lidar such as the STAR lidar used to collect the results presented in Chapter 6.

2.1.1 Effects of External Magnetic Field on Complex Refractive Index

The key element in the DEMOF is a heated magneto-optic vapor cell through which the received laser light is transmitted. This cell is heated in order to vaporize an appreciable amount of atomic vapor within the cell. Each cell oven uses a set of permanent magnets to create a roughly uniform magnetic field aligned with its transmission axis, which has several significant effects on the light transmitted through the vapor cell.

One way to understand the effects of magnetic fields on the spectroscopic behavior of atoms

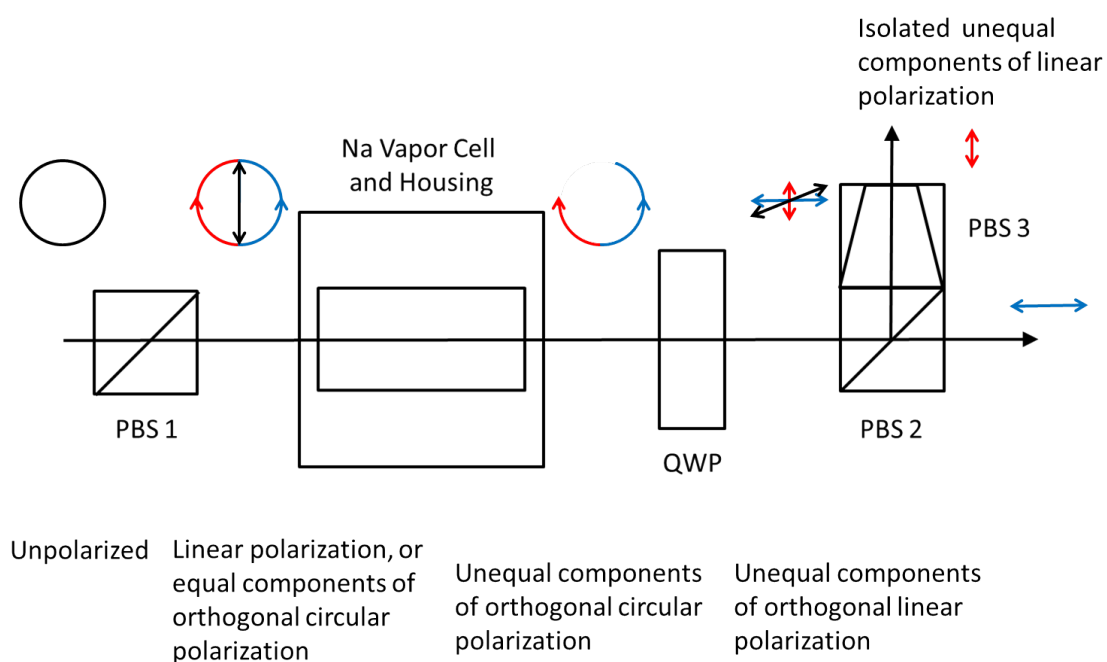


Figure 2.1: Diagram showing the polarization components present in the light transmitted by the DEMOF, before and after each component affecting these polarizations.

is through the idea of the complex refractive index χ , which combines absorption and dispersion into one complex quality. The real part of the complex refractive index corresponds to dispersion, similarly to the common real-valued refractive index, and the imaginary part corresponds to the absorption. The presence of a strong magnetic field creates a frequency-dependent perturbation in the complex refractive index of the Na vapor within the cell, resulting in absorption and dispersion spectra that differ between the circular polarization components of the transmitted light [7].

The Na-DEMOF uses the asymmetric absorption of the two circular polarization components to establish a double-edge filter that is applied to the received light after it is linearly polarized. The linearly polarized light coming into the vapor cell can also be understood as the sum of two equal components of orthogonal circular polarization. These two equal components are absorbed by the Na vapor to different extents, depending sensitively on the wavelength of the transmitted light. Each of these two components is converted to a linearly polarized component by the quarter-wave plate and isolated by the following polarizing beam splitter.

The difference in absorption spectra for the two circular polarization components is due to the energy shift known as the Zeeman Effect, and appears in plots of the spectra as translation of the absorption valleys away from the Na D2 absorption line. The intermediate magnetic field strength necessitates the use of the full theoretical solution [7], which yields vapor cell transmissions of the two circular polarizations given by Equations 2.1 and 2.2, where χ_M and χ_P are the complex refractive indices of the polarization components receiving reduction and increase in energy, respectively, L is the vapor cell length, and λ is the wavelength of transmitted light. These complex refractive indices must be calculated as the complex Voigt profile, or Faddeeva function, which can be numerically approximated [13]. The algorithm used for these calculations is provided in Appendix C.

$$T_-(\lambda) = e^{-\frac{2\pi L}{\lambda} \text{Im}(\chi_M)} \quad (2.1)$$

$$T_+(\lambda) = e^{-\frac{2\pi L}{\lambda} \text{Im}(\chi_P)} \quad (2.2)$$

2.1.2 Resonance-Fluorescence and Rayleigh Lidars

Atmospheric lidars (or laser radars) are one of the most versatile tools available for investigating atmospheric dynamics. The use of lasers to probe the atmosphere results in greater capabilities for high-resolution data acquired at high repetition rates over a broader range of the atmosphere than is possible with any other technique. Radar is restricted to observations of ionospheric variations and meteoric head echoes. Sonar is restricted to tropospheric observations where the atmospheric density is high enough for both propagation and reflection of sound waves. Sounding rockets provide single passes of acquisition through the atmosphere and require expensive refueling and refurbishment of the sounding rockets and on-board instruments. Other types of in-situ measurements, such as balloon-borne instruments and low-Earth orbiting atmospheric satellites present logistical limitations similar to those of sounding rockets. All-sky imagers are generally passive and cannot provide range resolution, although the wider field of view does allow for some discoveries not possible with lidars without time-intensive scanning schemes.

By contrast, atmospheric lidars present no difficulties with repeated acquisition of data over large ranges of the atmosphere. The probe wavelengths available to lidars allow for investigation throughout the entirety of the atmosphere, without restriction to the troposphere or ionosphere like other remote range-resolved instruments. Lidar's active sensing nature and range resolution provide data with high signal levels that are useful for research in dynamics that vary with altitude. Although there are many types of atmospheric lidars, the common operating principle is the stimulation of some part of the atmosphere with a laser beam and the collection of scattered or fluoresced return photons with timing gates to provide for range resolution.

The Na-DEMOP allows for the application of a resonance-fluorescence lidar, which would normally confine observations to the neutral metal layer in the mesosphere and lower thermosphere (MLT), to the stratosphere and lower mesosphere.

Resonance fluorescence lidars, like the STAR lidar to which the Na-DEMOP is being applied, depend on resonant absorption of transmitted laser light by metal atoms left behind in the upper

atmosphere by meteors and cosmic dust entering the atmosphere. These excited metal atoms fluoresce, emitting photons isotropically that are detected in ways that allow for the determination of the Doppler broadening and shift of the resonating population of metal atoms. This Doppler broadening and shift correlate directly to the temperature and line-of-sight wind in the resonant atom population, allowing for the derivation of atmospheric density, temperature, and wind profiles that are essential for studying wave dynamics, fundamental dynamical parameters, and numerous other burgeoning fields of atmospheric research.

Rayleigh lidars involve scattering of the transmitted laser light by high-density molecular vapors in the lower atmosphere. Many of these lidars transmit a single wavelength of high-power laser light and allow for the inference of temperature profiles by integration of the hydrostatic equation from a known or assumed calibration temperature at the upper boundary of temperature derivation. These lidars are unable to derive wind velocities simultaneously, instead requiring separate systems or reconfiguration to use other edge filters (such as Iodine filters or Fabry-Perot etalons) or interferometers to obtain this data. By contrast, the Na-DEMOf provides a method for simultaneous derivation of temperature and line-of-sight wind speed, by application to a three-frequency resonance-fluorescence lidar. This method reduces complexity and cost by giving a single lidar the power to derive temperature, wind, and density in both the MLT region and the lower atmosphere, with modifications only to the receiver. The use of a resonance-fluorescence lidar as the transmitter also allows for the use of a second Na vapor cell as an absolute frequency reference using Doppler-free spectroscopy, ensuring stable and precisely controlled wavelengths of laser light for both atmospheric stimulation and measurement of the Na-DEMOf filter function.

The general form of the lidar equation for Rayleigh scattering lidars is given by Equation 2.3, in which the volume backscatter coefficient β is given by Equation 2.4. N_R is the number of photons with wavelength λ collected over the interval Δt under stimulation of a region of the atmosphere Δz at range z_R with Rayleigh scatterer number density n_R by a laser with transmit pulse power P_L . The individual Rayleigh scatterers each have an effective Rayleigh backscatter cross-section of σ_R . The photon collecting telescope has area A ; the total receiver efficiency is η ; and the background

count rate is N_B . The one-way atmospheric transmission is T_a , and the geometric overlap of the lidar beam with the telescope's field of view is G . $P(z)$ and $T(z)$ represent the pressure in millibars and temperature in Kelvin at altitude z [3].

$$N_R(\lambda, z_R) = \left(\frac{P_L(\lambda)\Delta t}{hc/\lambda} \right) (\sigma_R(\pi, \lambda)n_R(z_R)\Delta z) \left(\frac{A}{z_R^2} \right) (\eta(\lambda)T_a^2(\lambda, z_R)G(z_R)) + N_B\Delta t \quad (2.3)$$

$$\beta(\pi, \lambda, z) = \sigma_R(\pi, \lambda)n_R(z) = 2.938 \times 10^{-32} \left(\frac{P(z)}{T(z)} \right) \frac{1}{\lambda^{4.0117}} \quad (2.4)$$

Subtracting the background from the raw photon count profiles and taking ratios between the background-removed photon count profiles allows for the isolation of the effects of the filter function on the Doppler-broadened and shifted return signal. Because Rayleigh scattering is frequency-independent over the 900-MHz transmission frequency variability of the STAR lidar, the Na-DEMOF acts as the primary frequency selector. Thus, the temperature and line-of-sight wind speed of each altitude bin under scrutiny only affect the received photon count ratios through their effects on the return signal spectra, and these ratios can be simulated as long as the Na-DEMOF filter function and atmospheric return spectra are known for any given temperature and wind speed.

2.2 DEMOF Theoretical Formulation

The Gaussian shape of the Doppler-broadened photon return spectrum is defined by Equation 2.5, with the RMS Doppler linewidth defined by Equation 2.6. ν_L is the transmitted laser frequency, ν_R is the radial wind velocity, T is the average Rayleigh scatterer temperature, and M is the average Rayleigh scatterer molecular mass.

$$\sigma_{scat}(\nu) = \frac{1}{\sqrt{2\pi}\sigma_D} e^{-\left(\nu - \nu_L \left(1 - \frac{2\nu_R}{c} \right) \right)^2}{2\sigma_D^2} \quad (2.5)$$

$$\sigma_D = 2\sqrt{\frac{k_B T \nu_L^2}{Mc^2}} \quad (2.6)$$

Convolution of this simulated atmospheric return with the lineshape of the pulsed-dye amplifier (PDA) that is the final stage of the STAR lidar transmitter, and then with the measured filter function described in Chapter 4, yields the expected background-removed photon counts for a parcel of air with a given temperature and radial velocity, allowing for the construction of ratio metrics that depend primarily either on wind or on temperature. These ratios are given by Equations 2.8 and 2.7, in which N_R^+ represents the number of photon counts received or simulated after transmission through the right edge filter of the Na-DEMOF (and after removing the background photon counts), with the laser frequency increased by AOM frequency shifting. N_L^- represents the same quantity, transmitted through the left side of the filter at the reduced laser frequency. c_W and c_T are calibration constants required to compensate for asymmetric efficiencies experienced throughout the receiver by light transmitted through the two independent filter optical paths. These asymmetries are independent of altitude and are most affected by variations in quantum efficiency among the photomultiplier tubes (PMTs) used to measure the received photons. The method by which these calibration constants may be obtained is discussed in Chapter 4.

$$R_T(V_{LOS}, T) = \frac{N_L^-}{c_T \times N_R^-} \quad (2.7)$$

$$R_W(V_{LOS}, T) = \frac{c_W \times N_R^+ - N_L^+}{c_W \times N_R^+ + N_L^+} \quad (2.8)$$

These ratio metrics are chosen in an attempt to isolate sensitivity to either temperature or wind from the other measured quantity. Figure 2.2 shows the wind and temperature ratios calculated for simulated atmospheric returns corresponding to temperatures between 160 K and 350 K, and for radial winds between -70 m/s and +70 m/s.

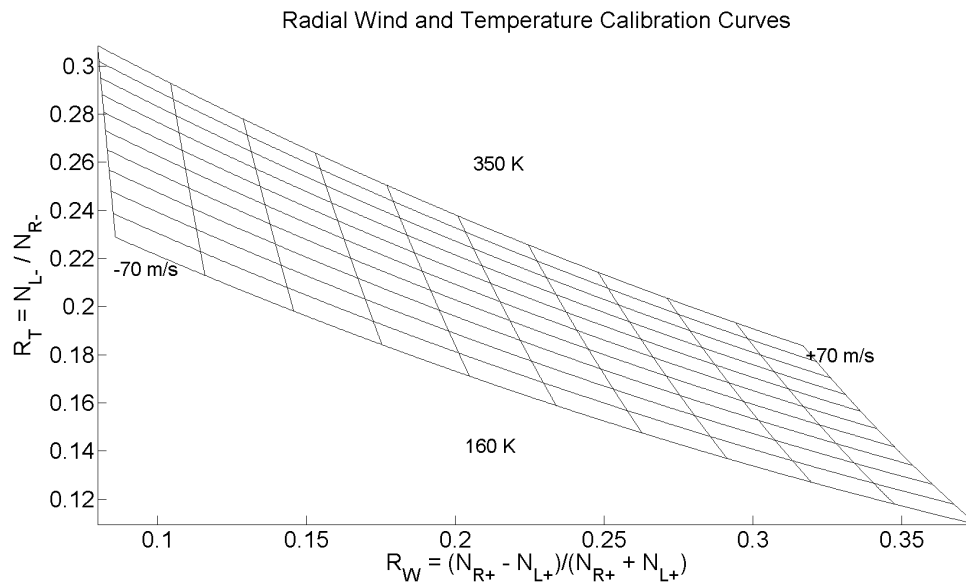


Figure 2.2: A calibration mesh generated by calculation of wind and temperature ratios for simulated atmospheric returns at various probe points of temperature and radial wind velocity. The approximately vertical lines are isotachs representing constant wind values from -70 m/s to +70 m/s, while the downward-sloping horizontal lines are isotherms representing constant temperature from 160 K to 350 K.

2.2.1 Temperature and Wind Uncertainties

Photon shot noise limits the precision of temperature and radial wind measurements. The relative uncertainties in the temperature and wind ratios are given by Equations 2.9 and 2.10, statements of the quadrature sums of the uncertainties from each photon count number involved in the corresponding ratio [3]. B_R^+ refers to the background counts collected within a defined range and time integration period, transmitted through the right edge filter during the amount of time allotted to transmission of the laser frequency shifted down by the AOMs.

$$\frac{\Delta R_T}{R_T} = \frac{1}{N_L^-} \sqrt{N_L^- (1 + c_T R_T) + B_L^- + c_T^2 R_T^2 B_R^-} \quad (2.9)$$

$$\frac{\Delta R_W}{R_W} = \frac{2c_w}{(c_w N_R^+)^2 - (N_L^+)^2} \sqrt{(N_L^+)^2 (N_R^+ + B_R^+) + (N_R^+)^2 (N_L^+ + B_L^+)} \quad (2.10)$$

The impact of these uncertainties in ratio metrics on temperature and wind measurements are given by the inverses of Equations 2.11 and 2.12, in which σ is the simulated Rayleigh return for a given set of temperature and wind coordinates, including convolution with PDA lineshape and Na-DEMOF filter function.

$$\frac{\partial R_T}{\partial T} = R_T \left(\frac{\partial \sigma_L^-}{\partial T} (\sigma_L^-)^{-1} - \frac{\partial \sigma_R^-}{\partial T} (\sigma_R^-)^{-1} \right) \quad (2.11)$$

$$\frac{\partial R_W}{\partial W} = (\sigma_R^+ + \sigma_L^+)^{-1} \left((1 - R_W) \frac{\partial \sigma_R^+}{\partial W} - \frac{\partial \sigma_L^+}{\partial W} \right) \quad (2.12)$$

The sensitivities of Rayleigh backscatter cross-section to variations in temperature and wind can be calculated for a given set of temperature and wind coordinates via Equations 2.13 and 2.14.

$$\frac{\partial \sigma_R}{\partial T} = \frac{\sigma_R}{2T} \left(\frac{(\nu - \nu_L)^2}{\sigma_L^2} - 1 \right) \quad (2.13)$$

$$\frac{\partial \sigma_R}{\partial W} = \frac{2\nu(\nu - \nu_L)\sigma_R}{c\sigma_L^2} \quad (2.14)$$

These backscatter cross-section sensitivities must be convolved with the PDA lineshape and measured Na-DEMOF filter function before application to the ratio sensitivities stated in Equations 2.11 and 2.12. Once these sensitivities are determined, multiplication of the ratio uncertainties (Equations 2.9 and 2.10) by the inverse of the ratio sensitivities (Equations 2.11 and 2.12) yields the corresponding uncertainties in temperature and radial wind measurements.

Several integration operations are applied to the photon count profiles in order to improve the photon signal SNR and the reliability of the corresponding wind and temperature profile derivations. Temporal integration results in the increase of the photon count numbers at all altitudes, improving the SNR and reducing the uncertainties of derived wind and temperature by decreasing the relative uncertainties given in Equations 2.9 and 2.10. The photon count SNR increases as the square root of the total integrated photon count signal. Similarly, vertical summing of subsequent bins increases the number of photon counts used for a given set of wind and temperature measurements, roughly as the square root of the number of bins summed together. Vertical Gaussian smoothing of these photon count profiles likewise improves the SNR by a factor roughly equivalent to the square root of the number of bins spanning half the FWHM of the Gaussian smoothing profile.

2.3 IDL Simulations

An algorithm developed by Sean D. Harrell and David A. Krueger to simulate the quantum mechanical effects determining the transmission of a Faraday anomalous dispersion optical filter was modified by Wentao Huang to simulate the transmission of the Na-DEMOF. The revised algorithm is provided in Appendix C,

This simulation makes several key assumptions about the vapor cell and housing. The vapor cell is assumed to be held at a uniform temperature upon reaching steady state, with perfectly transmissive windows and exactly 5 cm of uniformly heated vapor to absorb the transmitted light. The magnetic field is assumed to be constant and parallel to the beam of transmitted light along the entire vapor cell. The algorithm is capable of an exact numeric solution accurate even in the case of intermediate-strength magnetic field [12] [13], and nuclear magnetic dipole shifts are included [7].

Doppler broadening of the vapor absorption cross-sections is not yet included in this algorithm.

By testing various strengths of magnetic field and vapor temperature, the theoretical optimal conditions can be determined to be a temperature greater than or equal to 160 °C and a magnetic field close to 1400 G. These conditions result in a crossover height between the two edges of the filter at approximately 50% transmission, with close to 100% absorption in the extinction band.

Figures 2.3 and 2.4 show the simulated transmission functions of the Na-DEMOPF, with emphasis on the entire filter spectrum and the subset used for the Na-DEMOPF applied to the STAR lidar.

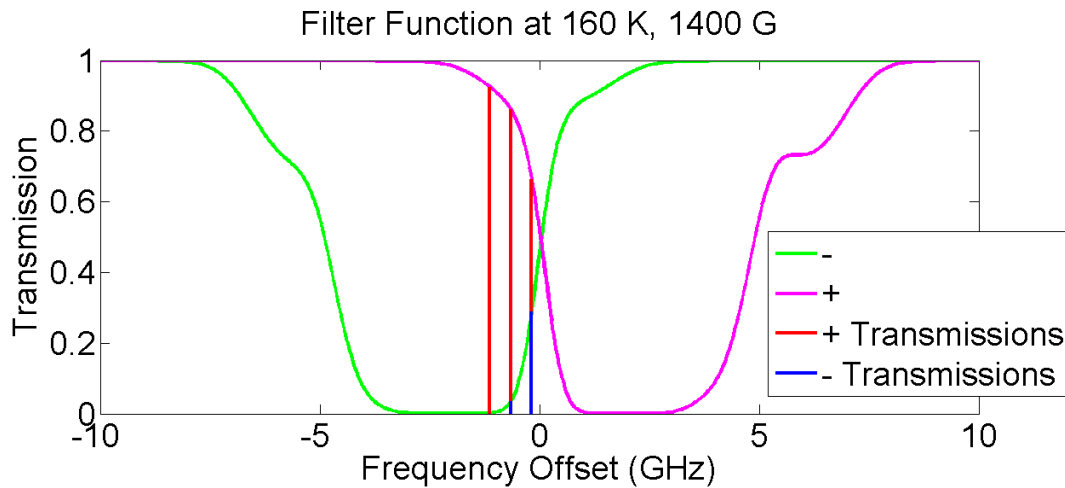


Figure 2.3: Theoretical transmission of Na-DEMOPF over entire D2 lineshape.

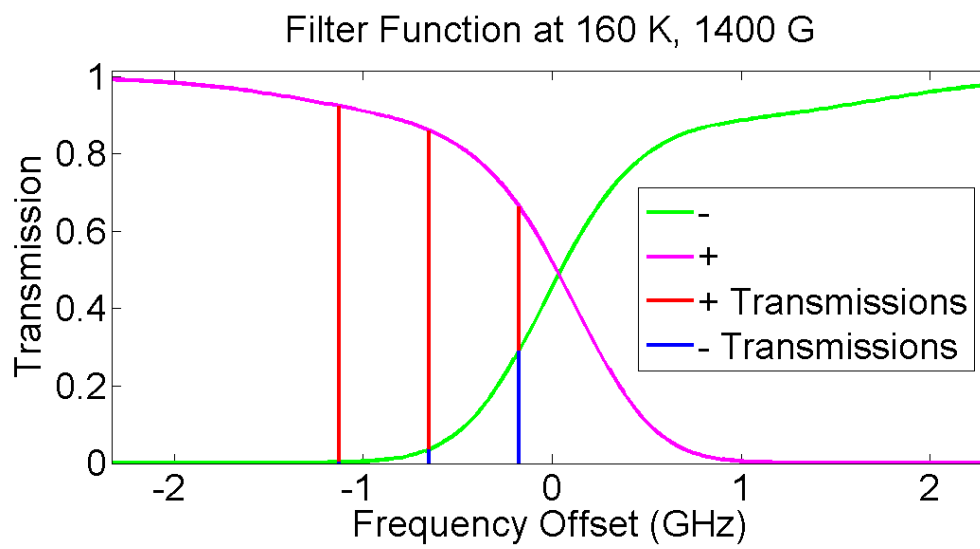


Figure 2.4: Theoretical transmission of Na-DEMOf, enhanced for emphasis on the frequencies transmitted by the STAR Na Doppler lidar.

2.4 Practical Considerations and Limitations

Practical experience with the Na-DEMOf suggests several limitations of this theory and practical challenges in maintaining nominal operation. The vapor cell housing, when fully tightened to the vapor cell and heated, has been seen to cause stress on the cell windows resulting in anisotropic birefringence and depolarization of the transmitted light. Instability in vapor cell temperature can cause variations of the transmission function, along with hysteresis of the ferromagnets and condensation of Na vapor on the cell windows or within the cell's Na sample-bearing tip. The magnetic field permeating the Na sample is not perfectly constant in either strength or orientation along the entire length of the cell. Finally, polarization effects from the method of coupling light into the filter have demonstrated some effect on the measured filter function. These limitations necessitate the empirical measurement of the true Na-DEMOf filter functions and design and construction with the limitations in mind. The filter function measurement is described in Chapter 4, and the design is outlined in Chapter 3.

Chapter 3

Detailed Design

This chapter details the most current designs of the Na-DEMOF, beginning with the optics surrounding the vapor cell housing and then describing the internal structure of the heated vapor cell and housing.

3.1 Optics

Figure 3.1 displays the detailed optical design of the Na-DEMOF atomic filter. The atmospheric return is coupled into the filter on the left from a fiber connected to the collecting telescope, passes through the mechanical chopper which blocks the high-intensity returns from the troposphere and lower stratosphere at the beginning of each photon collection, and is collimated through the first polarizing beam splitter (PBS1) by two lenses, L1 and L2. This linearly polarized light passes through the Na vapor cell, experiencing frequency-dependent differential absorption of the two initially equal circular polarization components which compose the linear polarization. These two orthogonal circular components of polarization are converted into orthogonal linear components of polarization by the quarter-wave plate (QWP) before being separated by PBS2 into two distinct optical paths, each of which is focused onto the corresponding photomultiplier tube's (PMT's) sensor by L3 or L4. PBS3 ensures that the light focused onto PMT2 is cleanly composed of only one of the two polarization components, as the ThorLabs PBS cubes used provide better polarization extinction by a factor of ten in the transmitted beam compared to the reflected beam.

This optics setup will be refined as the project moves forward, to minimize background

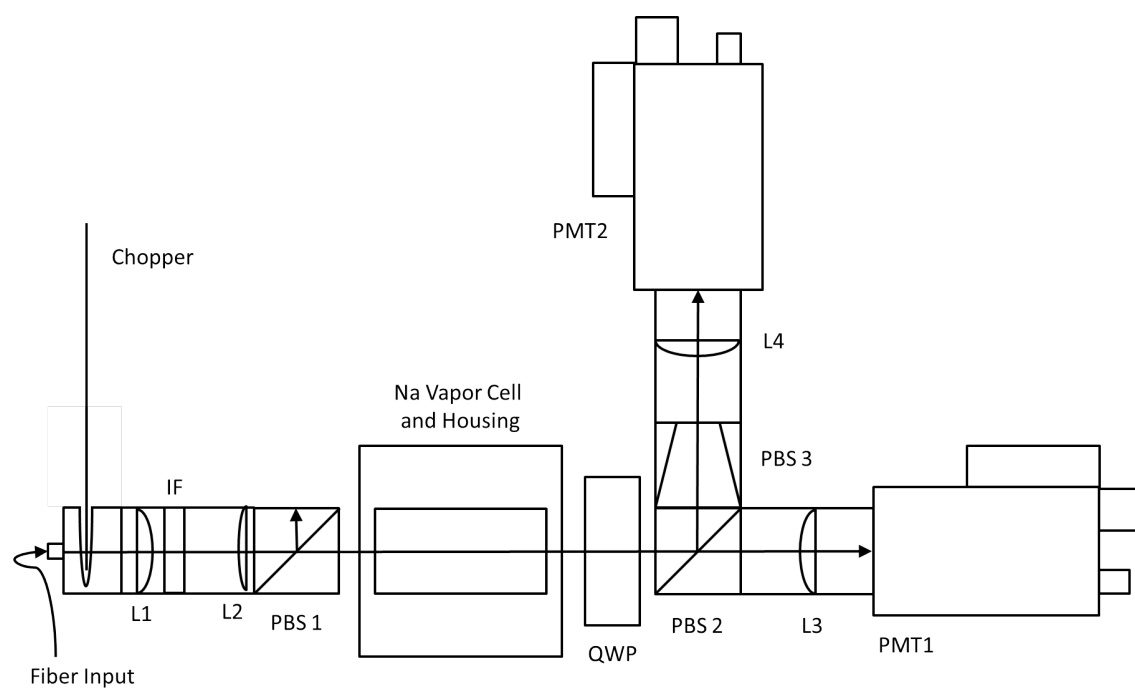


Figure 3.1: The nominal optical setup of the DEMOF filter involves optical fiber injection, beam collimation and focusing, three polarizing beam splitters (PBS), two photomultiplier tubes (PMTs), a quarter-wave plate (QWP), and the atomic vapor cell itself.

by keeping the path light-tight between the interference filter and the PMTs. However, several temporary measures have been used to reduce the background levels quickly without extensive design and construction work. The ambient light within the receiver container is reduced by ensuring that all lit displays or LEDs used to monitor equipment status are covered with black electrical tape. Black electrical tape also covers the open faces of each PBS that do not lie on the optical path, and thick black cloth is draped over the optics setup during data acquisition in order to reduce the amount of ambient light that can be admitted to the detectors through any aperture except that of the collecting telescope.

3.2 Vapor Cell Oven and Housing

The vapor cell requires stably elevated temperatures to achieve the required Na vapor pressure, in addition to a strong permanent magnetic field, in order to function as designed [7] [9]. The magnetic field is provided by a set of five annular NdFeB ferromagnets stacked end to end, forming a cavity into which the cell oven, or heater block, can be placed. The oven consists of a cylindrical copper block with cavities for the vapor cell, four resistive cartridge heaters, and a resistance temperature detector. The vapor cell itself is a hollow tube of Pyrex with a reservoir filled with solid Na metal jutting out of the side by about 1 cm. The cell oven is clad in a block of Teflon insulation, and the entire assembly fits into an aluminum housing with room for further insulation on both ends and for the wires connecting the cell oven to an external temperature control box.

The cartridge heaters within the copper heater block must be placed near the ends in order to discourage Na condensation on the windows, and the windows must not be compressed by the heater block, as this mechanical stress can cause anisotropic birefringence in the windows and disrupt the polarization of incoming light.

3.3 Heating Electronics

The electronics used to monitor the vapor cell temperature and control the heaters are shown in Figure 3.3. The temperature is measured by the PXR3 microcontroller, which reads the resistance of the RTD embedded in the copper heater block and controls the current through the heaters by activating or deactivating the solid-state relay (SSR). This current to the SSR and heaters is provided by the power supply. The EMI filter, fuse, and power switch provide various forms of protection for the power supply from the wall socket into which the power box must be connected.

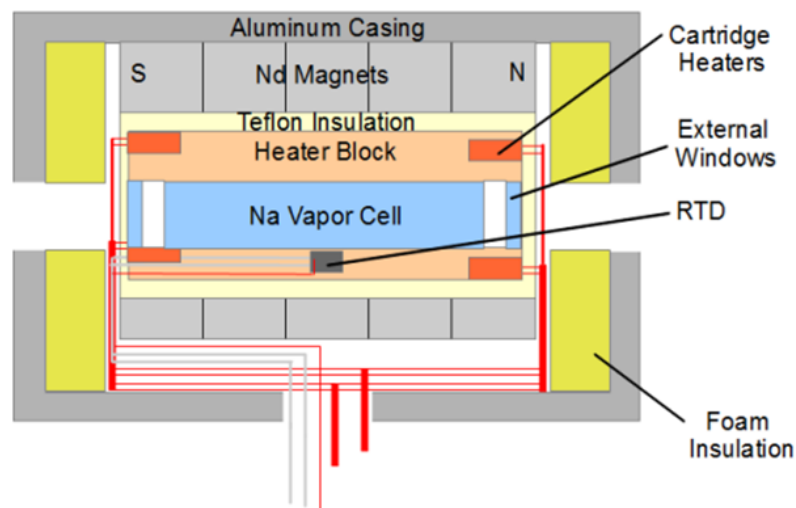


Figure 3.2: The aluminum housing of the DEMOF holds an annular array of NdFeB rare-earth permanent magnets, insulation, and the copper heater block which in turn houses the heated Pyrex vapor cell, resistance temperature detector (RTD), and four resistive heaters. The sodium sample within the vapor cell partially vaporizes when heated.

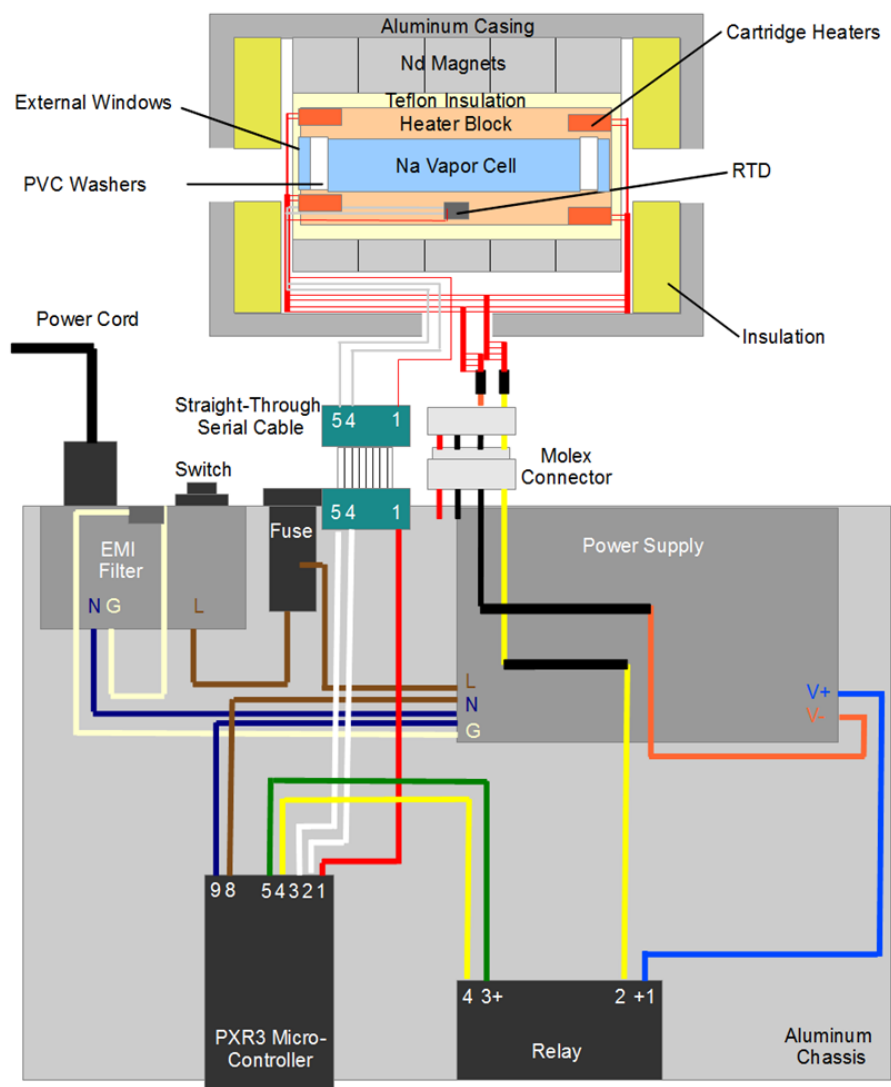


Figure 3.3: The power conditioning and temperature detection electronics box is shown connected to a vapor cell within the DEMOF housing.

Chapter 4

Calibration and Data Acquisition

This chapter discusses the method by which the Na-DEMOf can be calibrated, by measuring its transmission over a range of frequencies and determining the values of two calibration constants for each Na-DEMOf, which are independent of altitude and time and derive from differences in the receiver optics.

Each filter optical setup must be tested in several configurations to obtain accurate filter functions used in processing data collected with the filters, and each night of data must be calibrated in order to eliminate the biases resulting from optical effects outlined in Section 4.3 This section details the procedures for testing and processing filter functions and calibrating each night of data.

4.1 Filter Function Measurement

In order to analyze the photon count signals returned through the Na-DEMOf, it is necessary to measure accurately the filter functions describing the variation of transmission with frequency of the transmitted light.

4.1.1 Instrumentation and Setup

The DEMOf setup splits one optical fiber input into three usable outputs, as can be seen in Figure 4.1. Photodiode (PD) 1 is used during filter function testing to measure the power of the beam entering the DEMOf for normalization purposes. PD2 and PD3 are the beams transmitted and reflected by polarizing beam splitter (PBS) 2, and represent the two independent components

of DEMOF transmission. PBS 1 polarizes the unpolarized light input to the filter and splits off the power normalization signal for filter function testing. PBS 2 splits the two independent linear polarizations of light present after the Quarter Wave Plate (QWP), and PBS 3 ensures the purity of the light reflected by PBS 2.

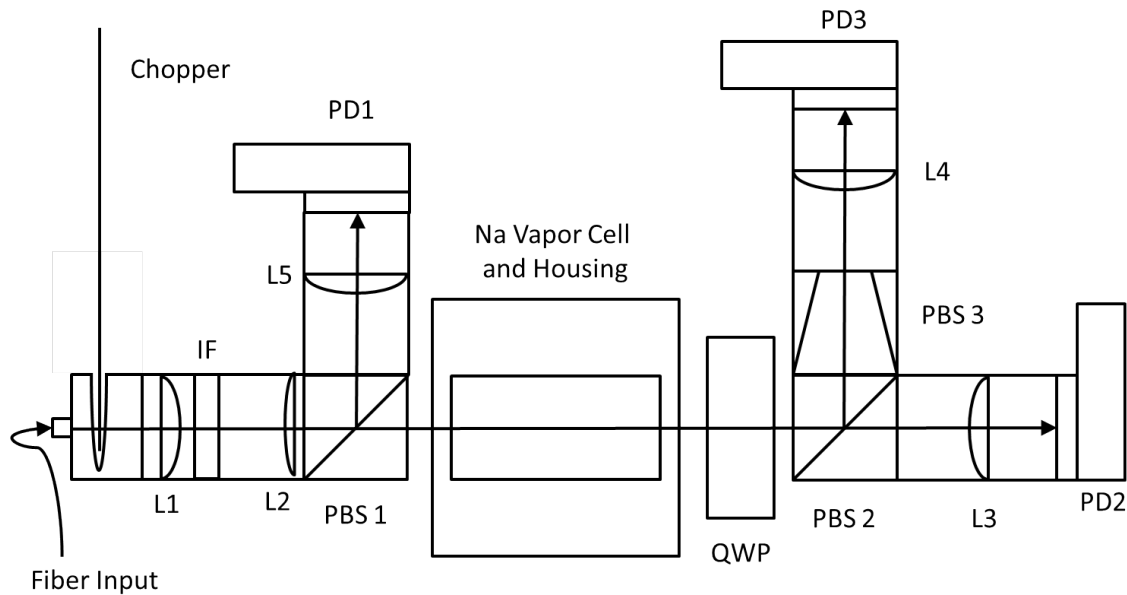


Figure 4.1: Filter function testing for the DEMOF involves an optical fiber input similar to the nominal configuration, but photodiodes are used in place of PMTs and the optical fiber carries a CW input directly from the STAR lidar optical path.

In order to measure the filter function of the DEMOF, The optical fiber input is generated by diverting the 589.159-nm STAR laser beam into an optical fiber. A neutral density filter is employed to prevent saturation of the photodiodes affixed to the DEMOF, and a mode scrambler was constructed by sandwiching optical tissues between two flat pieces of glass, in order to scramble the polarization of the light entering the optical fiber. This mode scrambler is included to ensure accurate correlation between the power normalization readings and the true input power to the DEMOF, by reducing the impact of frequency-dependent polarization on the proportions of light transmitted to the filter and the power normalization photodiode.

Four DET110A photodiodes are used to convert the visible light into voltage levels that can

be measured and recorded by a Tektronix oscilloscope. The photodiodes are used to measure four independent visible laser power levels. The Doppler-free transmission signal used by the STAR lidar to lock the beam precisely to the D2a peak of the sodium spectrum is measured for relation of oscilloscope scan time to frequency. PD1 in Figure 4.1 measures the power input to the DEMOF in order to eliminate in processing the effects of fluctuating laser power. PD2 and PD3 measure the light transmitted through the filter and transmitted or reflected by PBS2.

4.1.2 Procedure

Complete filter calibration requires the measurement of transmission, over a 19-GHz range of frequencies centered on the Na D2 line center, with the Na-DEMOF placed in six distinct configurations. Depending on the sensitivity of the instruments used and the amount of electrical noise in the test facility, it may be necessary to obtain multiple trials of each test, although the tests intended to measure background levels are less crucial and do not generally need to be repeated.

The first measurement requires the vapor cell and housing to be removed from the optical table, providing a baseline measurement for complete transmission. The second test mimics the setup of the first, with the exception of the input beam being blocked in order to measure the background level which must be removed from the first test results to accurately measure only the transmitted power levels.

The remaining tests all require the presence of the Na vapor cell within its housing, although the third and fourth tests make use of the unheated vapor cell without vaporized Na atoms present. This allows for the measurement of the cell window transmission efficiencies and provides the possibility of identifying any birefringent effects in the windows caused by mechanical stresses induced by the housing. The third test measures the power levels with the input beam unblocked, while the fourth test again involves blocking the input beam in order to measure the background power level for removal in processing.

The fifth and sixth tests are conducted after allowing the Na vapor cell to reach its nominal temperature, and again differ from one another only in that the fifth test uses the input beam while

the sixth test measures background levels with the input beam blocked. These six configurations are summarized in Table 4.1.

Table 4.1: Summary of configurations used to test the filter function of a single Na-DEMOf.

Configuration	Vapor Cell Present?	Input Beam Blocked?	Vapor Cell Heated?
1	No	No	N/A
2	No	Yes	N/A
3	Yes	No	No
4	Yes	Yes	No
5	Yes	No	Yes
6	Yes	Yes	Yes

These tests may also be used to optimize the nominal temperature, which depends on the effective strength of the ferromagnets and Na abundance within the cell. Practical experience suggests that various Na-DEMOfs will operate well at a certain temperature between 150°C and 165°C, but that unavoidable variations in vapor cell construction and ferromagnet strength necessitate the empirical determination of the optimal temperature for each new cell. The optimal temperature provides a flat extinction region for the frequency bands of maximum absorption through each edge filter, as well as a "crossover point" at which the two filter edges intersect near 50% transmission [5]. At least fifteen minutes should be provided between setting a new control temperature and inspecting the filter function, as the temperatures must reach steady state in order to ensure that the Na vapor within the cell is held at a constant temperature. Data collection from multiple beams requires replication of this calibration process for each Na-DEMOf that is to be used simultaneously.

4.1.3 Filter Function Processing

The effective filter transmission spectrum is derived by isolating it from the other factors affecting the optical power measured by the photodiodes. Before any comparison of the six test measurements is made, all of the functions are smoothed in order to mitigate the effects of digitizer

noise and allow for more precise identification of peaks in the Doppler-free spectrum. The time coordinates recorded during these scans are then correlated to absolute frequencies by comparison of the peaks in the Doppler-free spectrum to the known frequencies of the Na D2a and D2b peaks, assuming a constant rate of scanning in order to allow for linear extrapolation from these points.

After correlating the spectral scans to their corresponding frequency ranges, the background is removed from each of the three non-background configurations (configurations 1, 3, and 5 from Table 4.1) and the filter transmission scans are normalized by the corresponding input power measurements (from PD1 in Figure 4.1) in order to remove fluctuations from the STAR lidar transmitter generating the input beam. Multiple trials (three for each non-background configuration are sufficient for the results shown here) are then summed together to improve the signal-to-noise ratio, and the filter transmissions are determined by comparing the normalized transmitted power levels from the heated vapor cell configuration (5) to that from the cold-cell configuration (3). Figure 4.2 shows the filter functions obtained on July 10, 2015 which are used to generate the results in Chapter 6.

The normalized power levels from configuration 1 with the vapor cell absent can be compared to those from the cold-cell configuration to obtain estimates of the vapor cell window transmission efficiency, but this quantity is more useful for verifying that the windows are clean and free of condensed Na atoms than it is necessary for processing of the filter function. The cold vapor cells in the two Na-DEMOFs used to obtain these results have transmission efficiencies of 84.4% to 87.9%.

4.2 Data Acquisition

The results shown in Chapter 6 make use of data acquired on three separate nights in the year 2015: June 9th, July 26th, and August 5th. The data acquisition method for all three nights involved normal operation of the STAR lidar transmitter to transmit three frequencies of light in two off-zenith directions toward the north and west. The center transmission frequency ν_c is locked to the Na D2a peak, and the high and low frequencies ν_+ and ν_- are located symmetrically above

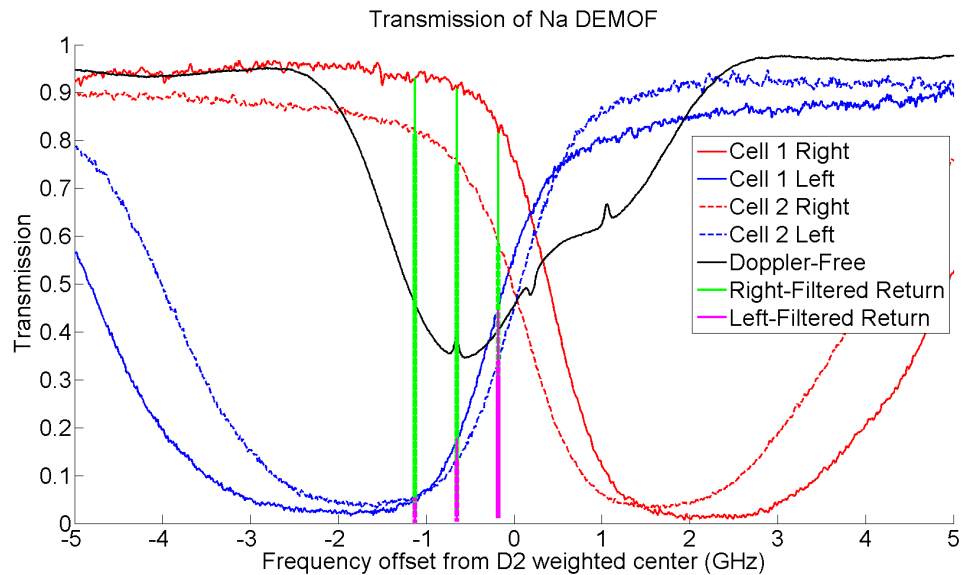


Figure 4.2: Processed filter functions measured for the two Na-DEMOFs used for this thesis, with STAR transmission frequencies highlighted. The black line represents the Doppler-free spectrum, displaying clearly the D2a and D2b peaks and crossover dip. The names "Right" and "Left" have been given to the edge filters with absorption valleys shifted to the right and to the left on this frequency spectrum.

and below this center frequency by 474-MHz acousto-optic modulator (AOM) shifts. The method for aligning the output beams 20° off zenith toward the north and the west is provided in Appendix B.

The receiver of the STAR lidar is modified for low-altitude Na-DEMOf observations by replacing the typical receiver optics following the optical fiber with the setup shown in Figure 4.3. The same chopper must be used for both channels, in order to ensure that the mechanical blocking of the high-intensity lower atmosphere signal does not drift relative to the laser pulse transmission timing or the photon counting profile acquisition timing. The height at which each fiber input is held must be aligned precisely to ensure that the chopper stops blocking the signals at close to the same altitude for both beams. The data acquisition program has been modified to collect four separate profiles, one from each of the PMTs present.

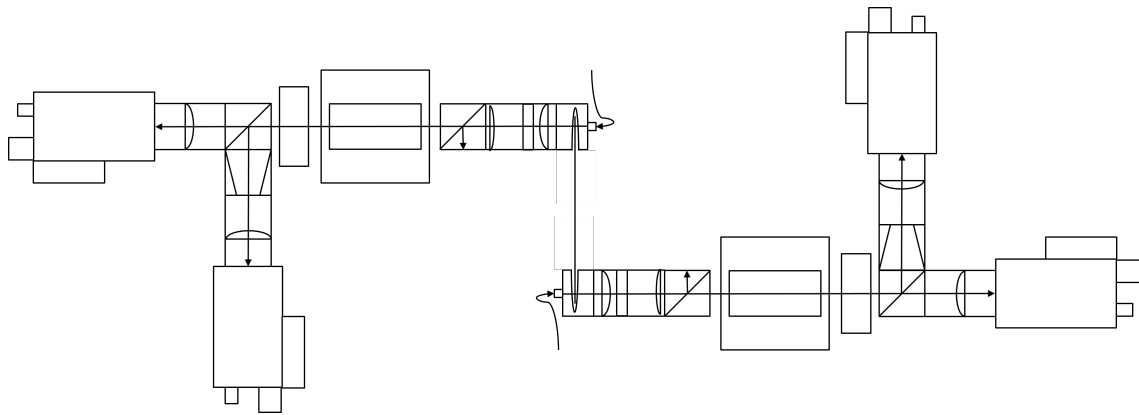


Figure 4.3: Diagram showing two-beam receiver setup for simultaneous data acquisition using two Na-DEMOfs. Compare to Figure 3.1 for individual components.

The photon count profiles from each beam are integrated over 3-second periods with a pulse repetition rate of approximately 30 Hz and 1 second devoted to each transmission frequency, recording a new profile containing all three transmission frequencies and both edge filter transmissions (yielding 12 total photon count profiles for two-beam operation) every 3 seconds. These raw profiles have a range resolution of 42 m. These recorded profiles are later processed according to the procedure outlined in Chapter 5 in order to calculate temperature and wind. Figure 4.4 shows an example photon count profile after removal of background and integration to allow for comparison of the return signal levels among frequencies and between edge filters.

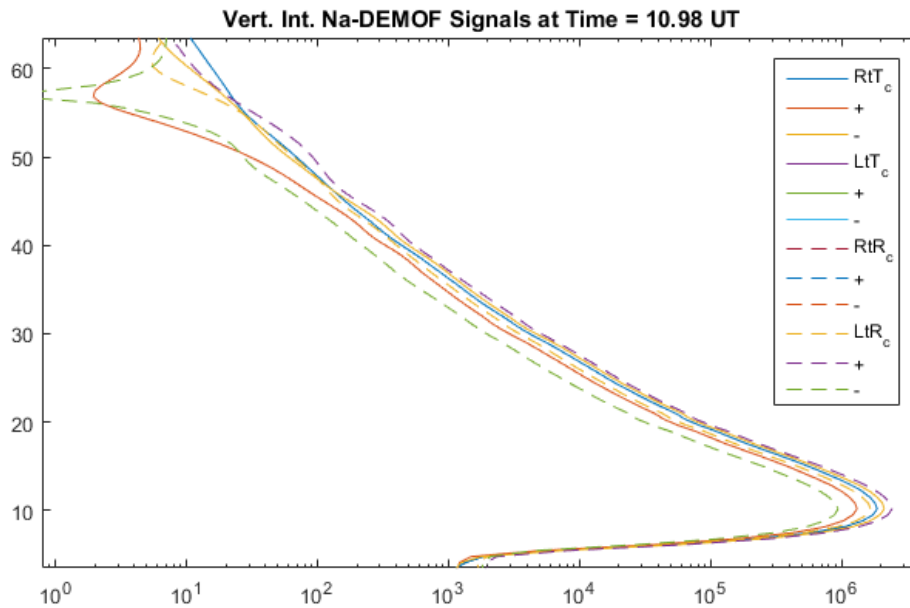


Figure 4.4: Example of a photon count profile collected on August 5, 2015. This profile has been integrated over 30 minutes of acquisition and vertically smoothed following removal of the background. The six lines shown represent the three frequencies of STAR transmission (c,+,-), transmitted through the right edge filter and transmitted through PBS2 (RtT) or transmitted through the left edge filter and reflected by PBS2 (LtR). As can be predicted from Figure 4.2, the left edge filter results in larger signal levels for greater laser frequencies, and the right edge filter has the opposite effect. The signal levels from the right edge filter are not as large as would be predicted from Figure 4.2 because the PMT collecting those photon counts has a significantly lower quantum efficiency than that collecting photons from the left edge filter.

4.3 Nightly Calibration

The calibration constants c_T and c_W shown in Equations 2.7 and 2.8 must be determined during data processing following data acquisition. The current method is to derive temperature and wind profiles with several test constants and to iteratively refine these test constants to eliminate the altitude-independent biases caused by uneven PMT quantum efficiencies, background levels, anisotropic birefringence introduced by stresses on the windows of the Na vapor cells, and total maximum transmission efficiencies of the different paths of each filter. These biases are determined by comparing the derived temperature to the relatively low-resolution MSIS model, and the derived winds to data from the nearby radiosonde located at station 72469 DNR, which can be obtained on a twelve-hour basis from the University of Wyoming Department of Atmospheric Science.

This comparison is performed for various test calibration constants, over a set range of altitudes in order to reduce processing time and minimize the impact of higher uncertainties in regions of lower signal strength or of aerosol contamination at lower altitudes. For all three nights discussed in this thesis, 30 km is an appropriate upper bound due to range-reduction of signal strength. However, variations in background and chopper trigger timing amongst the three nights require that the lower bound be set at 25 km for 6/9/2015, 12 km for 7/26/2015, and 20 km for 8/5/2015. Below these lower bounds, either the temperature or the wind profiles diverge wildly from the models and radiosonde measurements and can not necessarily be trusted for calibrating the filter.

The calibration constants required to eliminate these biases are calculated at 30-minute intervals and averaged over the entire night, in order to obtain both a single calibration constant for each night and a measure of the drift in the optics due to temperature changes or degradation of the Na vapor cell. This method yields different results for the three nights of acquisition described in this thesis, due to changes in the optical setups. The calibrations constants A_1 and B_1 corresponding to Vapor Cell 1 and A_2 and B_2 for Cell 2 are provided in Table 4.2 for each of the three nights.

The drastic difference in calibration constants between 6/9/2015 and 7/26/2015 resulted

Table 4.2: Averaged receiver optics calibration constants.

Date	A_1	B_1	A_2	B_2
6/9/2015	0.5073 ± 0.0059	0.5856 ± 0.0056	1.2036 ± 0.0107	1.3860 ± 0.0067
7/26/2015	1.1318 ± 0.0255	1.1675 ± 0.0121	2.0106 ± 0.0193	2.5100 ± 0.0125
8/5/2015	1.1807 ± 0.0260	1.1796 ± 0.0133	2.1920 ± 0.0354	2.5985 ± 0.0181

from switching the pair of PMTs used for northward observations with that used for westward observations. One of the PMTs associated with Cell 1 for northward observations on 6/9/2015 has been used more than the other three, resulting in significant degradation of quantum efficiency by a factor of about 2. Apart from that difference, it can be seen from this table that the calibration constants vary by less than 10% between subsequent nights. More data will be required to determine whether this variation is a consistent drift caused by depletion of the sodium reservoir or a random variation around constant values.

Chapter 5

Data Processing Scheme

Processing the photon count profiles collected by the STAR system involves two primary phases: general lidar pre-processing and DEMOF-specific derivation of temperature and wind velocities.

5.1 STAR Lidar Data Pre-Processing

The initial pre-processing procedure for the photon count profiles is common to both DEMOF data and that generated by the STAR system during normal Na resonance- fluorescence operation. Figure 5.1 outlines the procedure for processing the data.

Common to the procedures for both DEMOF data and typical STAR data is the isolation and conditioning of photon count profiles, shown as the first two rows in Figure 5.1. This begins with the initialization of key constants, loading of data files used to compensate for PMT saturation and to compare the derived temperature and wind profiles to the measurements of other nearby instruments. The lidar data files are then identified and categorized to remove any profiles corrupted by clouds or changing lidar configurations and to divide the list of files into 30-minute segments for integration. Each file is pre-processed to remove PMT saturation effects, signal reduction by the mechanical chopper, and background (measured as the signal seen between 120 km and 150 km) before being integrated over 30-minute intervals and 720-m range bins. These integrated profiles are then spatially smoothed using Gaussian smoothing profiles with widths increasing gradually with altitude to compensate for decreasing signal levels.

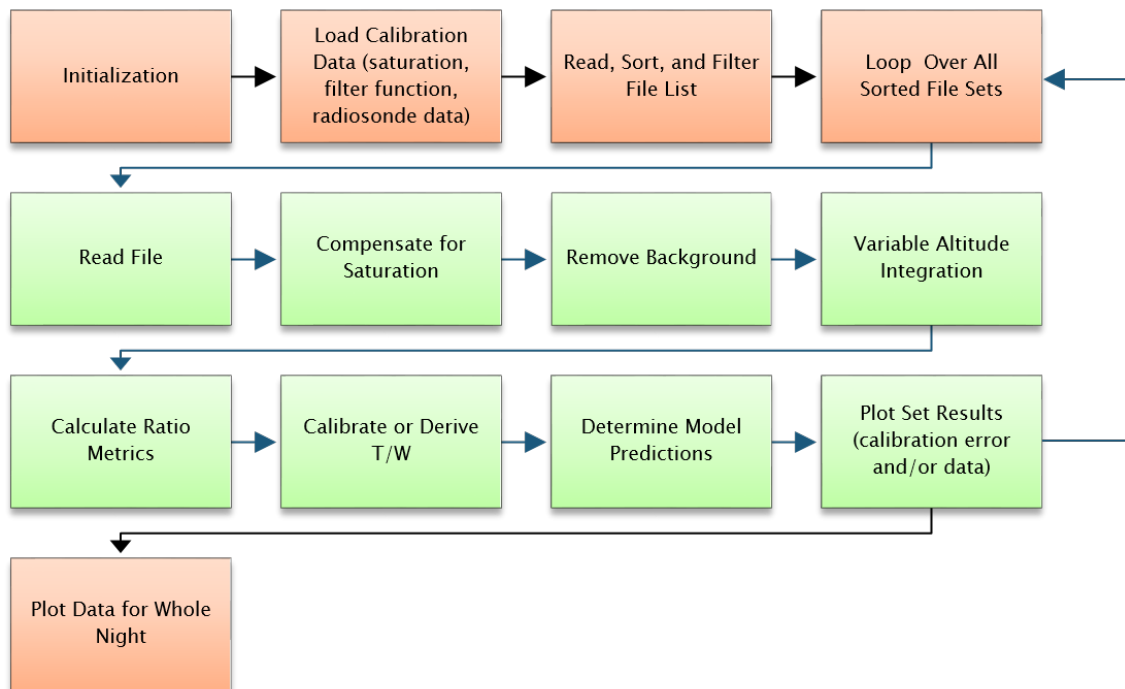


Figure 5.1: Flowchart outlining basic steps for processing Na-DEMOP data. The first two rows are also used for processing STAR data, but the Na-DEMOP processing scheme is unique starting with the calculation of the ratio metrics.

5.2 DEMOF-Specific Temperature and Wind Derivation

The general lidar pre-processing results in smoothed and integrated profiles of background-removed photon counts which can be compared between the two filters using the temperature and wind ratio metrics R_T and R_W defined in Chapter 2. Removing the background and inspecting only the ratios between the photon counts transmitted through each edge filter (with differing edge filter transmission efficiencies compensated for by the calibration constants) allows for isolation of the effects of Doppler broadening and shift on the return signal. Thus, the ratios defined in Chapter 2 may be applied to the simulated photon counts used to generate the calibration curves demonstrated in Chapter 2 as well as to the real background-removed photon count profiles obtained from the lidar data. These measured ratio metrics can be compared at each given altitude to the simulated calibration meshes produced by simulation, similar to the correlation of temperatures to ratio metrics shown in Figure 5.2, in order to derive temperature and radial wind speed profiles.

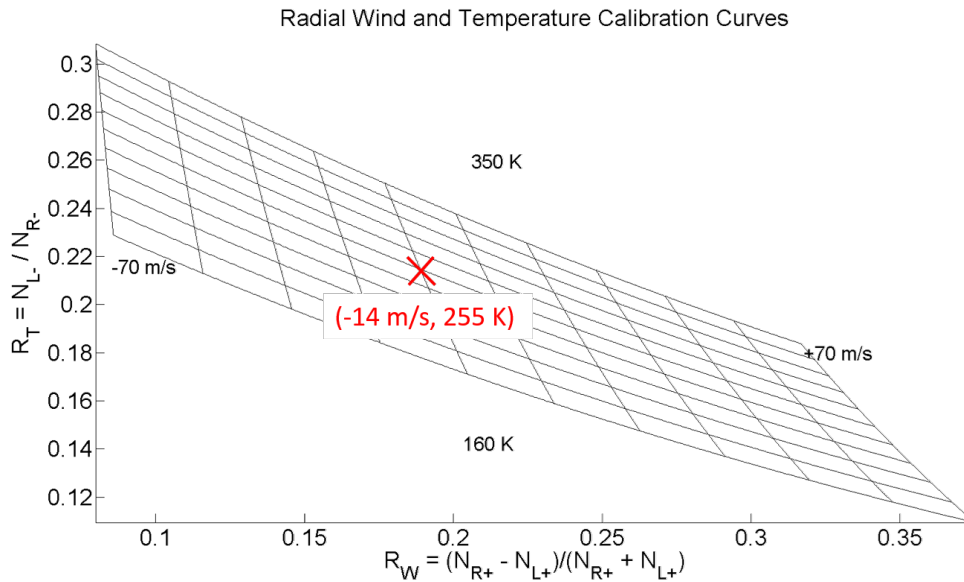


Figure 5.2: Example of mapping from ratio metrics R_T and R_W to temperature and radial wind coordinates. Mapping of the ratio metrics at each altitude in this fashion allows for derivation of range-resolved temperature and wind profiles.

Uncertainties in temperature and wind measurements incurred by this method can be deter-

mined by the method described in Chapter 2. Correlation of radial wind speeds measured by the northward and westward off-zenith beams to zonal and meridional winds either requires a third beam pointing toward zenith to remove vertical winds or depends upon the assumption that vertical winds average to zero over 30-minute intervals.

If the radial winds w'_N and w'_W are measured with beams aligned to elevation angles el_N and el_W , with error angles θ_N and θ_W (measured clockwise from true north and true west), Equation 5.1 can be used to determine the true northerly and westerly wind speeds w_N and w_W , under the assumption of zero vertical wind. Equation 5.2 gives the matrix translating the true northerly and westerly winds to the radial winds seen by the northern and western beams.

$$\begin{pmatrix} w_N \\ w_W \end{pmatrix} = R(\theta_N, \theta_W)^{-1} \begin{pmatrix} w'_N \\ w'_W \end{pmatrix} \quad (5.1)$$

$$R(\theta_N, \theta_W) = \begin{pmatrix} \cos(\theta_N) \cos(el_N) & -\sin(\theta_N) \cos(el_N) \\ \sin(\theta_W) \cos(el_W) & \cos(\theta_W) \cos(el_W) \end{pmatrix} \quad (5.2)$$

Chapter 6

Results and Analysis

This chapter summarizes the results obtained throughout the three full nights of data collection using the Na-DEMOf so far. The vertical resolution for all three nights is 672 m, with altitude-varied smoothing as outlined in Chapter 5. All three nights were calibrated according to the procedures outlined in Chapter 4. The error bars associated with the all-night integrations shown in Figures 6.5, 6.6, 6.11, 6.12, 6.17, and 6.18 represent three standard deviations of the mean profiles, obtained by comparing the multiple 30-minute integrated sets of derived profiles. As such, they do not purely represent the true error of the derived profiles, including true variations of the wind and temperature throughout the night and excluding biases remaining after calibration and any other errors which might affect all the 30-minute sets in the same way. One such unaccounted error is the divergence of some profiles in regions of low signal strength due to the increasing importance of background, which is discussed in Section 6.4.

The error bars displayed on each plot reflect the uncertainty in wind and temperature measurements due to shot noise, calculated as described in Chapter 2. Unaccounted for in this metric are errors from filter function drift overnight or between calibration and data collection due to temperature variation, fading permanent magnetic field, Na vapor deposition, or physical shifts in the receiver optics; from uncertainties in the PDA lineshape and offset, from contamination of the Rayleigh return by aerosol backscattering, and from the effect of residual background photon counts on the ratio technique as discussed in Section 6.4. Although no variations in factors related to filter function or PDA effects have been noted, the altitude-dependent divergence of the temperature

and wind ratios and measurements at lower altitudes suggest the existence of residual background photon counts that should be mitigated for future measurements. Aerosol contamination can also explain low-altitude divergence, but background mitigation will improve the SNR at all altitudes and also allow for derivation of temperature and wind profiles at higher altitudes. Throughout the three nights, the minimum temperature error for either beam ranges from 0.34 K to 0.81 K, and the minimum wind error ranges from 0.60 m/s to 1.1 m/s. The temperature errors at 40 km range from 4.0 K to 18.8 K, and the wind errors at 40 km range from 7.1 m/s to 16.4 m/s.

The three alternative data sources provided for comparison are the MERRA assimilative model, ECMWF model, MSIS model, and data collected by a radiosonde at station 72469 DNR in Denver, CO. MERRA data is provided on a daily basis with 1.25° spatial resolution in both latitude and longitude, corresponding to 86.5-mile meridional resolution and 66.2-mile zonal resolution. ECMWF data is provided on a six-hour basis with 0.25° spatial resolution corresponding to 17.3-mile meridional resolution and 13.2-mile zonal resolution. Radiosonde data is collected every twelve hours, and the station is 31.7 miles southeast of the STAR lidar at Table Mountain. The MERRA and ECMWF models can be interpolated to the location of the Table Mountain lidar facility where the STAR lidar is located, but the low resolutions of all three data sources preclude detection of gravity waves with periods shorter than twice the temporal resolution of the source. These low resolutions also make the comparisons more useful for longer integration times than for the half-hour integrated data presented for each night, so the nightly calibration procedure outlined in Chapter 4 depends on minimizing the bias between the all-night integrated wind and temperature profiles and the low-resolution MSIS or radiosonde data and results in one calibration constant per ratio metric per cell filter per night of data collection.

6.1 Results Obtained from 6/9/2015

The configuration for 6/9/2015 differs from the following two nights discussed here, as the PMTs used to collect photon counts from the northward-pointing beam were the older of the two sets of PMTs, and they have suffered some degradation with use (one by about 50% quantum

efficiency) which caused the resulting profiles to have lower signal-to-noise ratios (SNRs) compared to the profiles derived from the northward-pointing beam on the other two nights. However, the westward beam profiles had a higher SNR on 6/9 than on the other nights. The lower boundaries of the derived profiles occur at higher altitudes on this night because the chopper was set up to open at a higher altitude, until it was realized that the chopper opening altitude could be lower by several kilometers without over-saturating the PMTs.

6.1.1 30-Minute Temperature Profiles

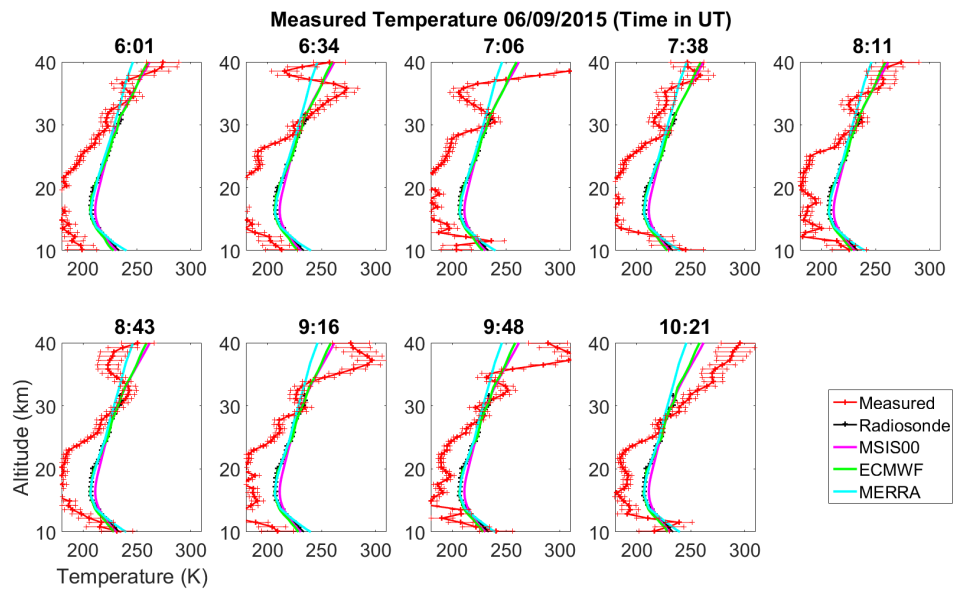


Figure 6.1: Temperature profiles derived with 30-minute integration times from Cell 1 data, pointed 20.075° off zenith at a true azimuth of 359.984° .

6.1.2 30-Minute Wind Profiles

6.1.3 4.5-Hour Integrated Profiles

The wind and temperature profiles derived for 6/9/2015 diverge at low altitudes below 25 km and at high altitudes above 50 km. Outside these altitudes, the diverging measurements quickly reach saturation values that represent the maximum test values used in simulating ratio metrics

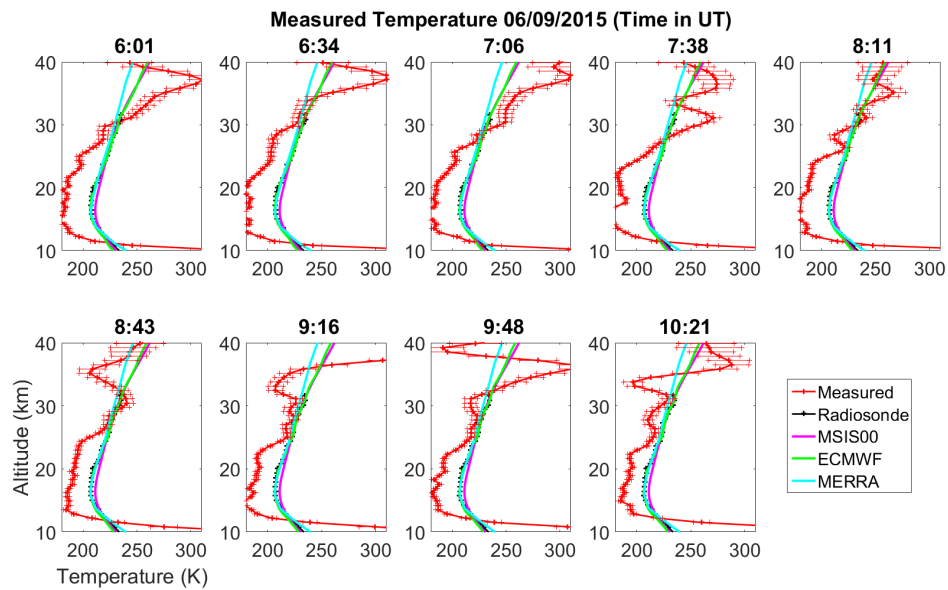


Figure 6.2: Temperature profiles derived with 30-minute integration times from Cell 2 data, pointed 20.142° off zenith at a true azimuth of 269.967° .

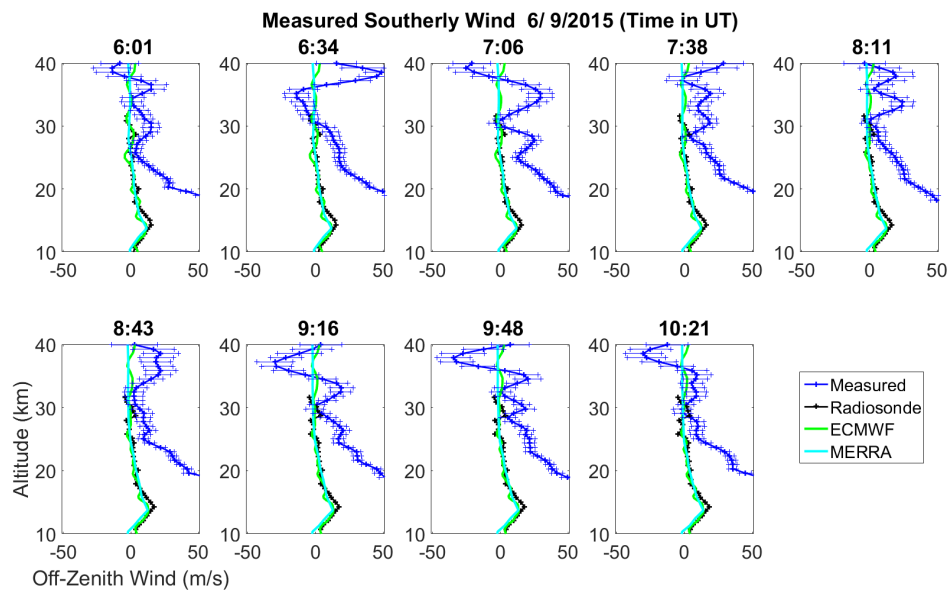


Figure 6.3: Wind profiles derived with 30-minute integration times from Cell 1 data, pointed 20.075° off zenith at a true azimuth of 359.984° .

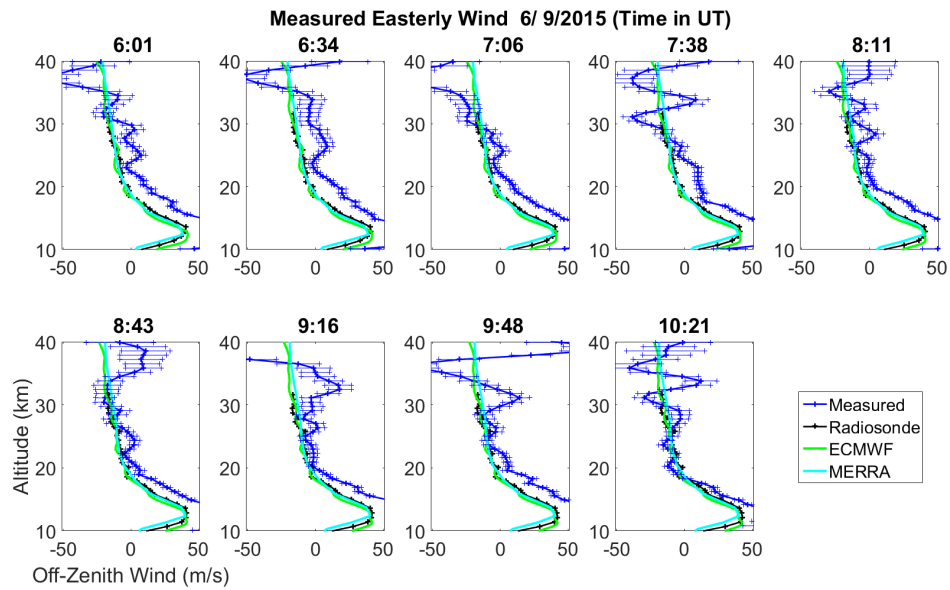


Figure 6.4: Wind profiles derived with 30-minute integration times from Cell 2 data, pointed 20.142° off zenith at a true azimuth of 269.967° .

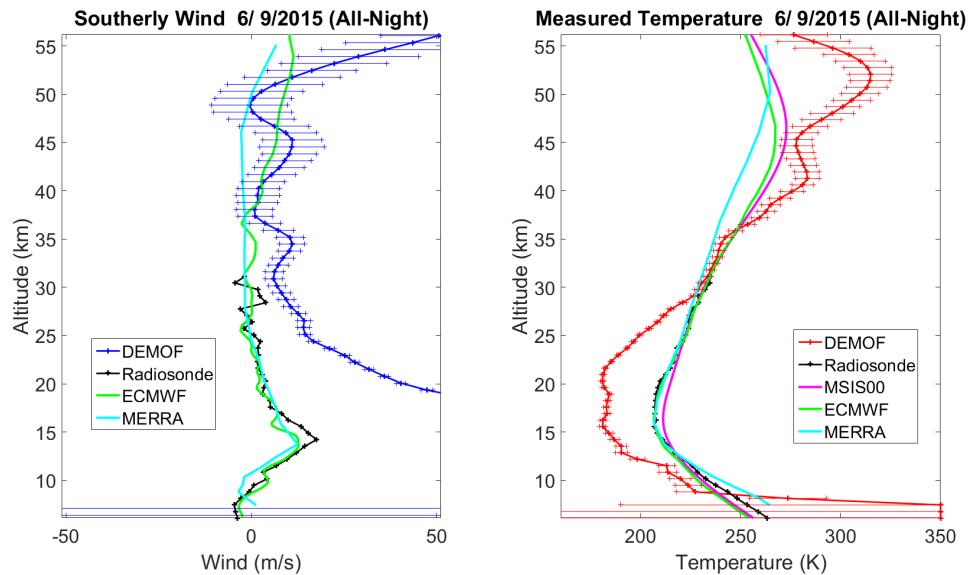


Figure 6.5: Temperature and wind profiles derived with 4.5-hour integration times from Cell 1 data, pointed 20.075° off zenith at a true azimuth of 359.984° .

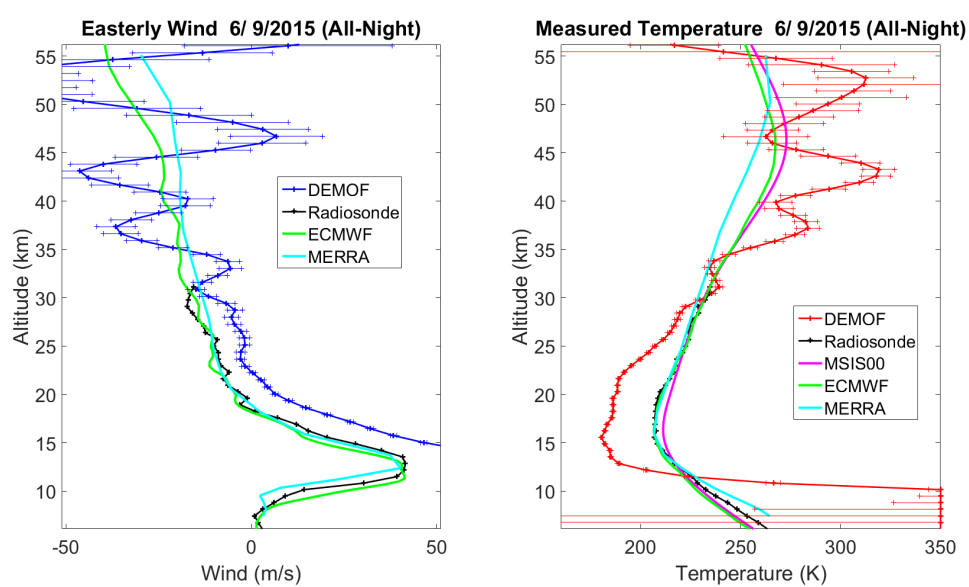


Figure 6.6: Temperature and wind profiles derived with 4.5-hour integration times from Cell 2 data, pointed 20.142° off zenith at a true azimuth of 269.967° .

to generate the calibration meshes used for temperature and wind derivations. The meshes used for these nights saturate at radial wind speeds greater than ± 70 m/s and at temperatures below 160 K or above 350 K. The delay between the chopper trigger and the start of each laser pulse was reduced after 6/9/2015, lowering the altitude at which the chopper fully opens and increasing the signal levels at low altitudes. The PMTs were also rearranged to collect data from channels with lower signal levels using PMTs with higher quantum efficiencies. This also means that data collected on nights after 6/9/2015 involve lower signal levels used for the derivation of profiles along the westward beam collected through the Cell 2 filter.

6.2 Results Obtained from 7/26/2015

Data from the MSIS, MERRA, and ECMWF models are displayed, as well as radiosonde data, for comparison to the derived temperature and wind profiles.

6.2.1 30-Minute Temperature Profiles

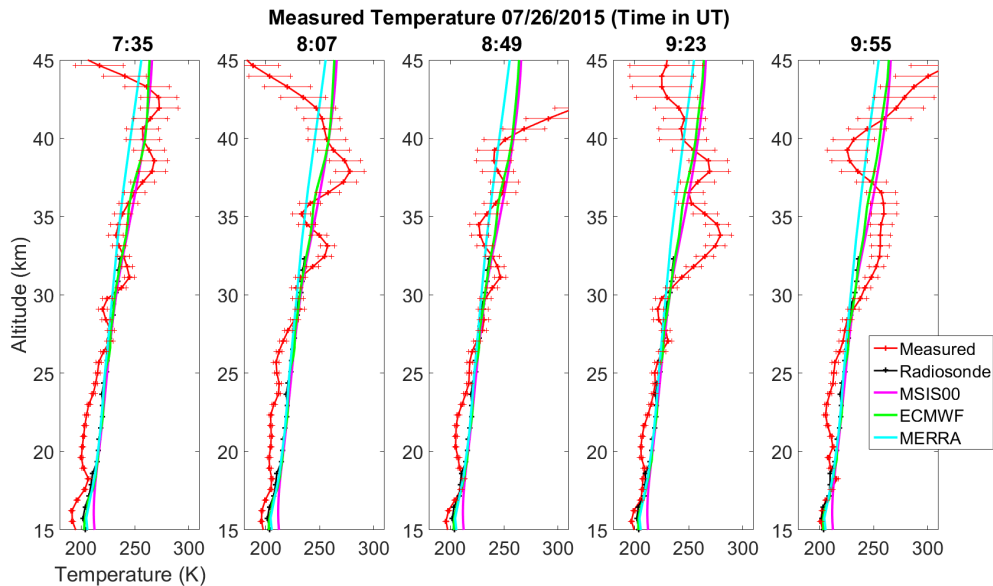


Figure 6.7: Temperature profiles derived with 30-minute integration times from Cell 1 data, pointed 20.075° off zenith at a true azimuth of 359.984° .

6.2.2 30-Minute Wind Profiles

6.2.3 2.5-Hour Integrated Profiles

The profiles derived for 7/26/2015 agree with the models and radiosonde down to low altitudes of 10-15 km, lowered by the lower chopper cutoff altitude. As noted in Section 6.1, the rearrangement of PMTs improved the profiles derived using Cell 1 and the northward beam while diminishing the profiles derived using Cell 2 and the westward beam. However, the increased amount of time devoted to zenith data before collecting off-zenith data reduces the available all-

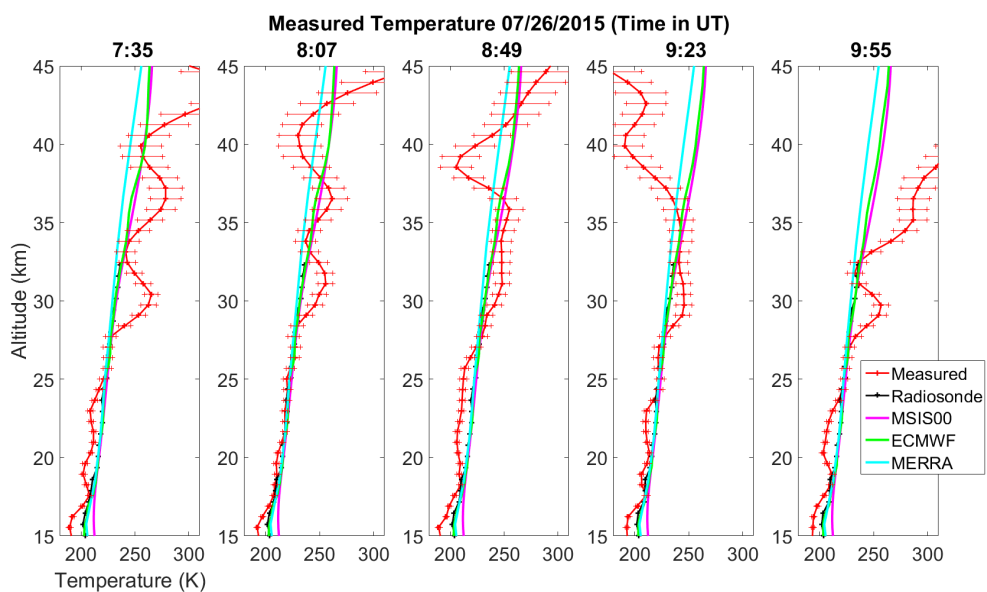


Figure 6.8: Temperature profiles derived with 30-minute integration times from Cell 2 data, pointed 20.142° off zenith at a true azimuth of 269.967° .

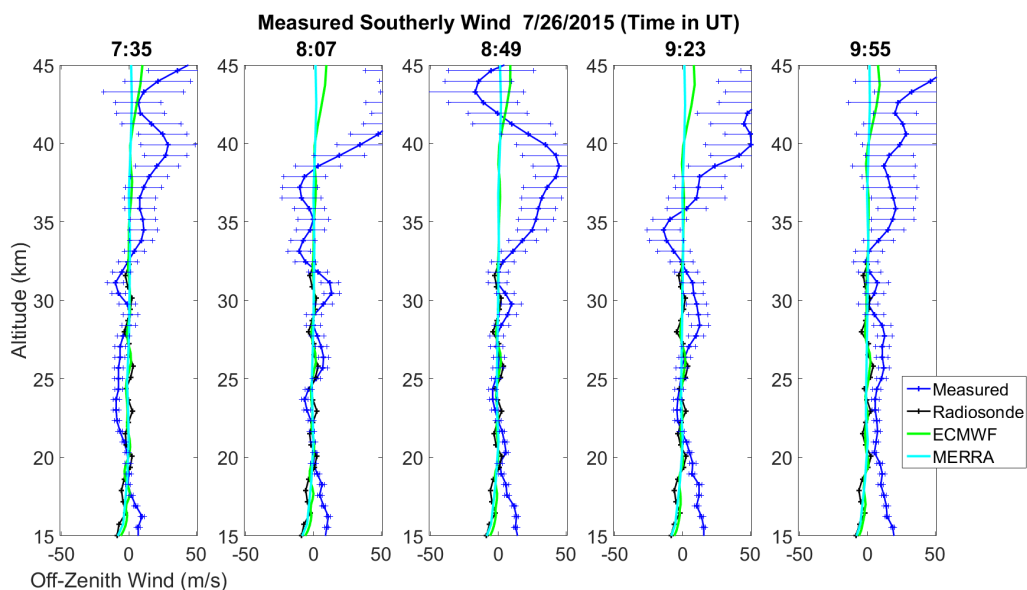


Figure 6.9: Wind profiles derived with 30-minute integration times from Cell 1 data, pointed 20.075° off zenith at a true azimuth of 359.984° .

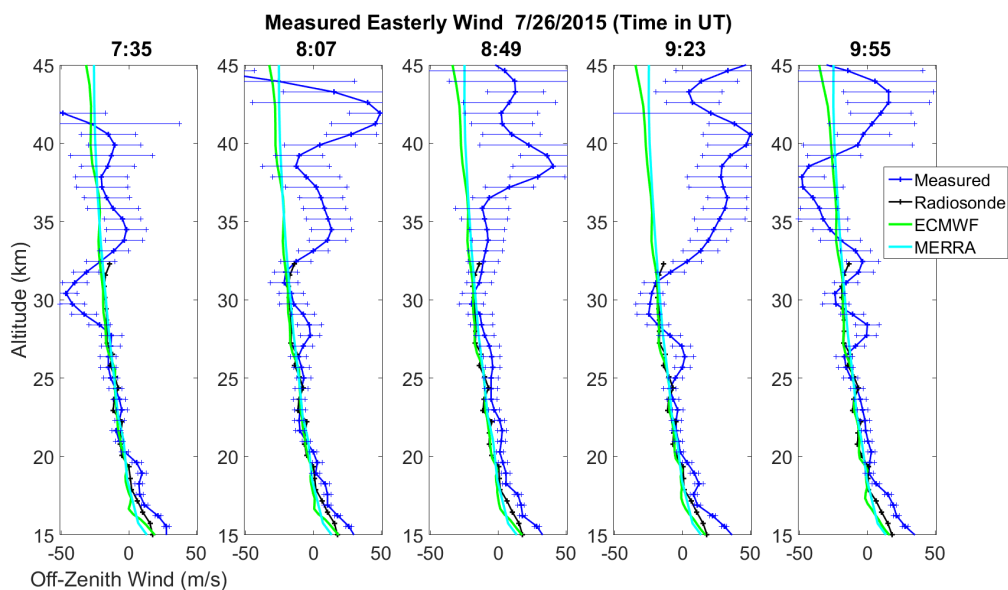


Figure 6.10: Wind profiles derived with 30-minute integration times from Cell 2 data, pointed 20.142° off zenith at a true azimuth of 269.967° .

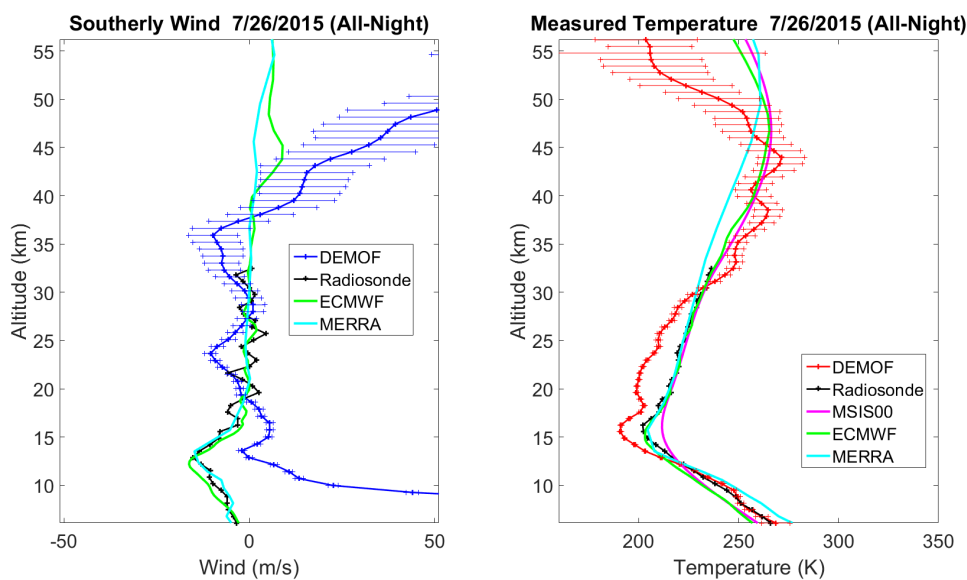


Figure 6.11: Temperature and wind profiles derived with 2.5-hour integration times from Cell 1 data, pointed 20.075° off zenith at a true azimuth of 359.984° .

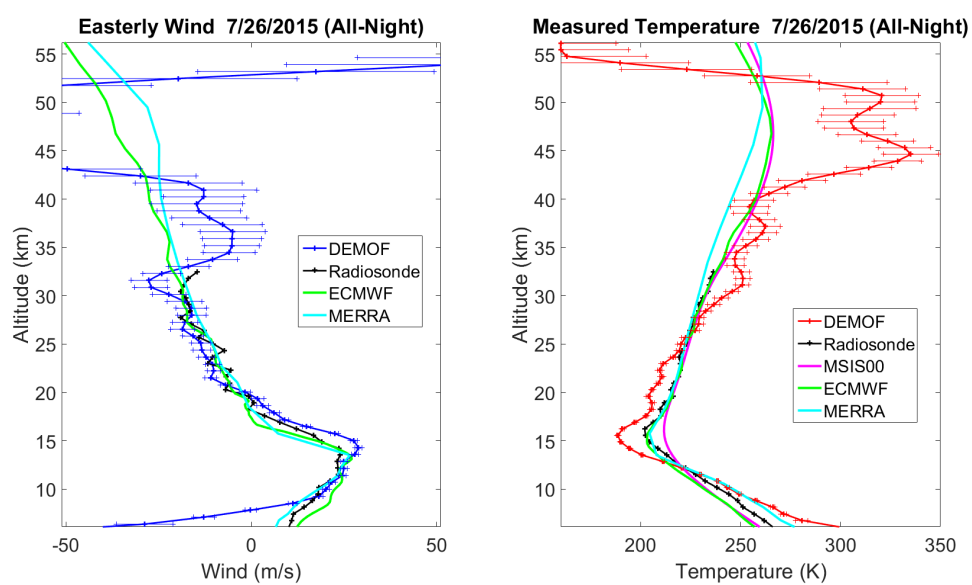


Figure 6.12: Temperature and wind profiles derived with 2.5-hour integration times from Cell 2 data, pointed 20.142° off zenith at a true azimuth of 269.967° .

night integration time to 2.5 hours. This limits the altitude range over which temperature and wind profiles can be derived, even after integrating over the entire night.

6.3 Results Obtained from 8/5/2015

By eliminating a 2-hour set of calibration data that had been included at the start of each night of acquisition until it was deemed to be of little use, the total length of data acquisition was extended on 8/5/2015 from 4.5 hours to 7 hours. However, ECMWF data are not available for comparison as of 12/1/2015.

6.3.1 30-Minute Temperature Profiles

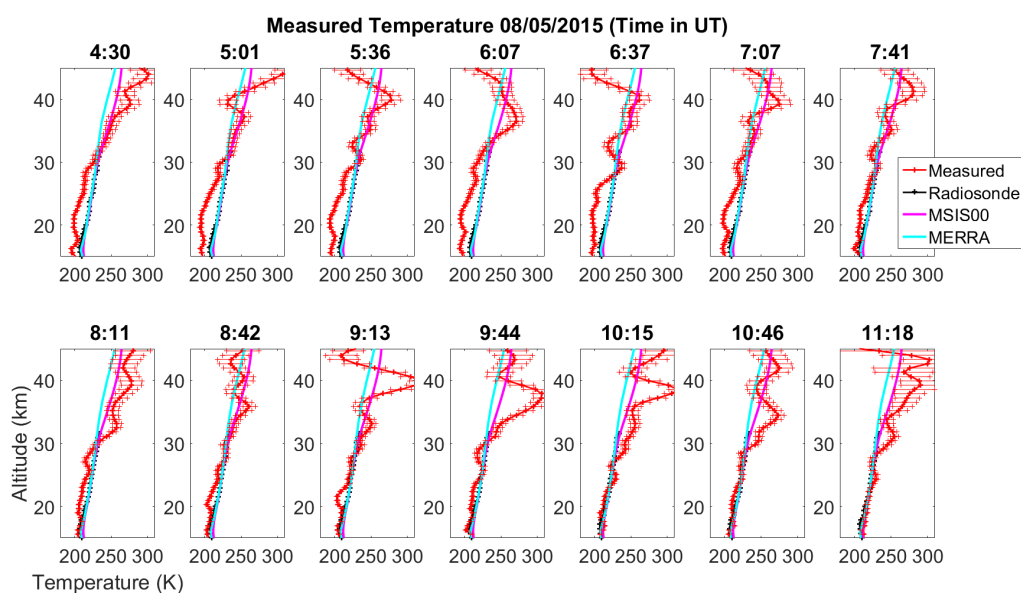


Figure 6.13: Temperature profiles derived with 30-minute integration times from Cell 1 data, pointed 20.075° off zenith at a true azimuth of 359.984° .

6.3.2 30-Minute Wind Profiles

6.3.3 7-Hour Integrated Profiles

Eliminating the zenith data collection time allows for 7 hours of off-zenith data collection and makes the all-night integration more effective, allowing for derivation of wind and temperature using Cell 1 and the northward beam from 8-70 km. However, the use of older PMTs with lower quantum

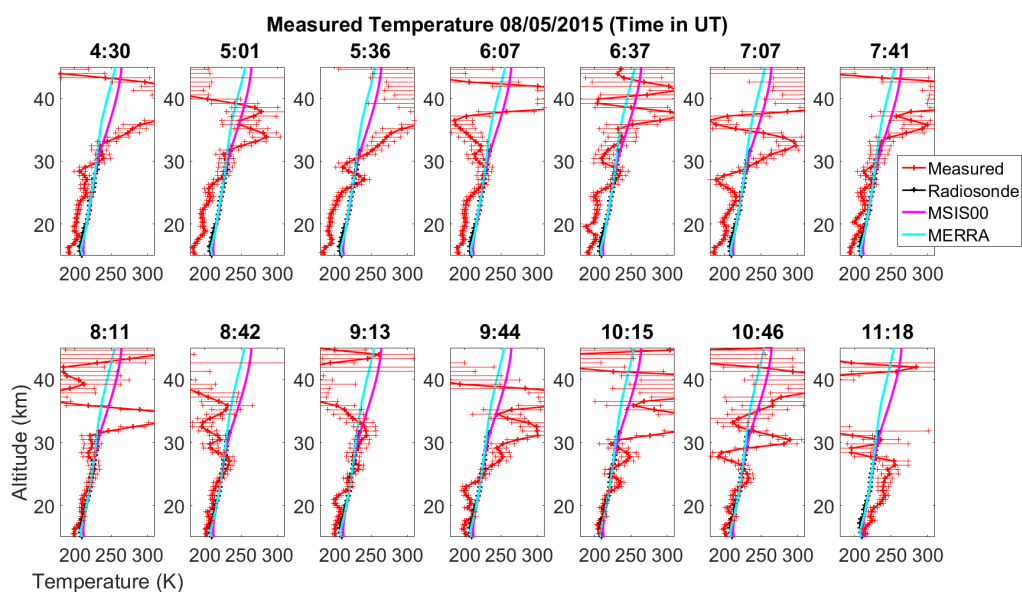


Figure 6.14: Temperature profiles derived with 30-minute integration times from Cell 2 data, pointed 20.142° off zenith at a true azimuth of 269.967° .

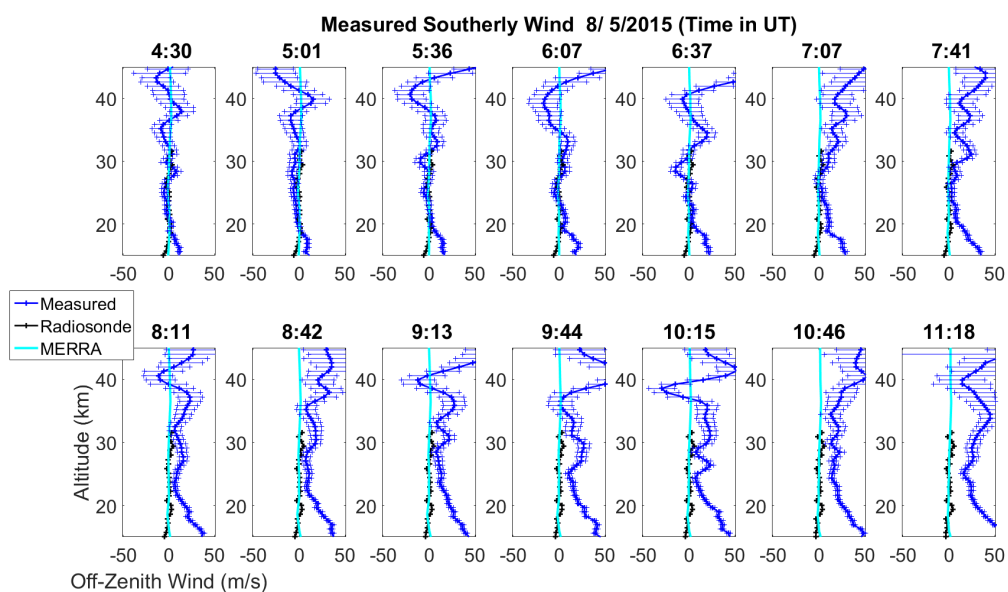


Figure 6.15: Wind profiles derived with 30-minute integration times from Cell 1 data, pointed 20.075° off zenith at a true azimuth of 359.984° .

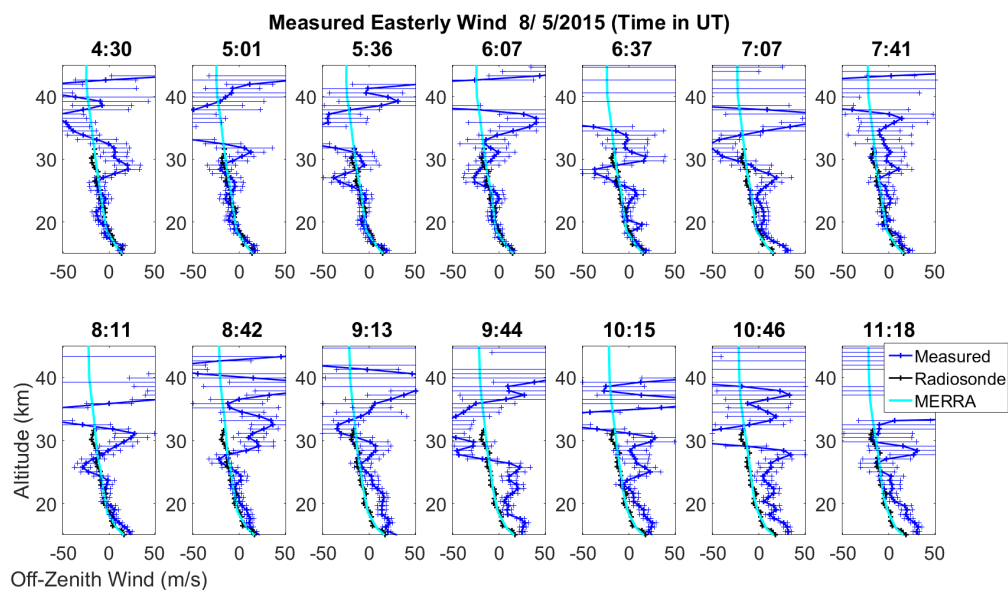


Figure 6.16: Wind profiles derived with 30-minute integration times from Cell 2 data, pointed 20.142° off zenith at a true azimuth of 269.967° .

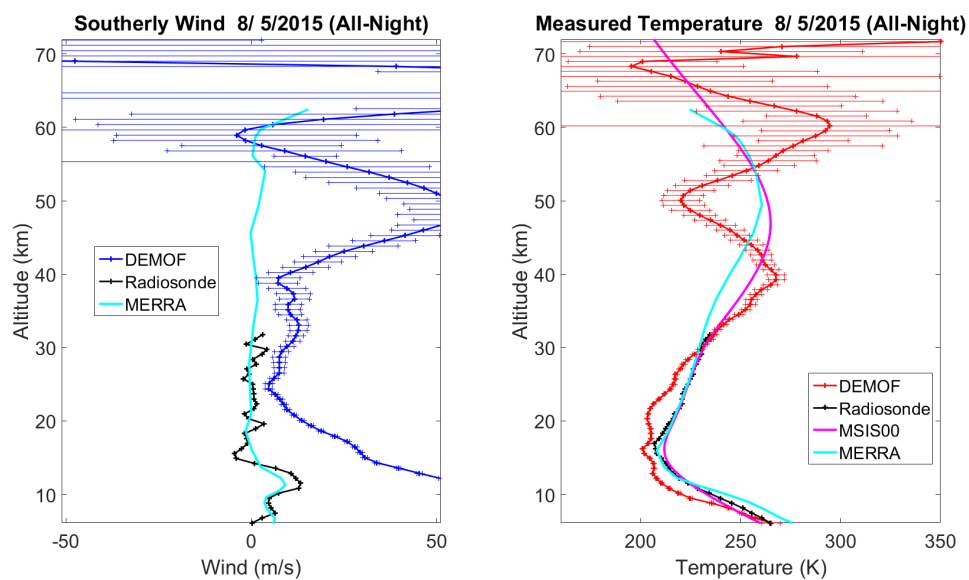


Figure 6.17: Temperature and wind profiles derived with 7-hour integration times from Cell 1 data, pointed 20.075° off zenith at a true azimuth of 359.984° .

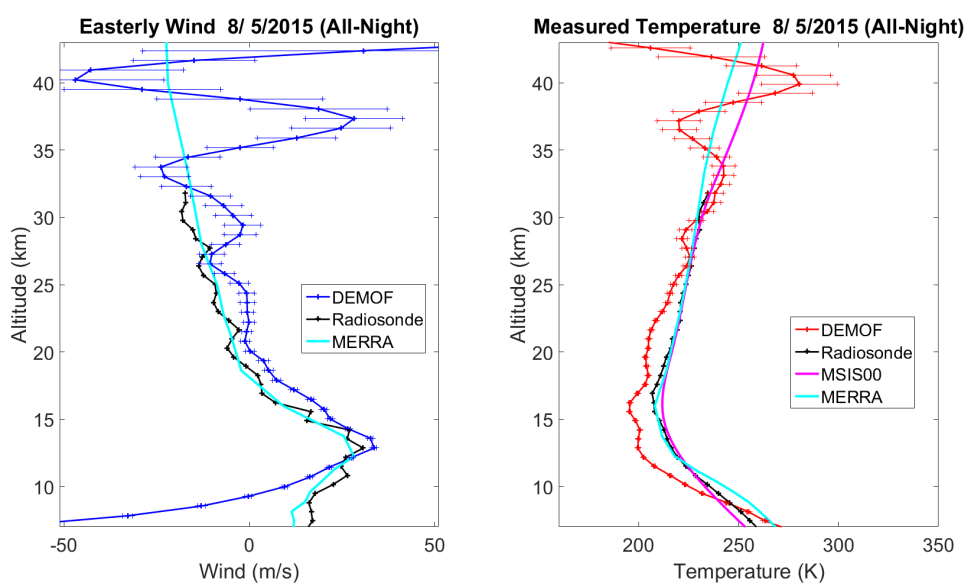


Figure 6.18: Temperature and wind profiles derived with 7-hour integration times from Cell 2 data, pointed 20.142° off zenith at a true azimuth of 269.967° .

efficiency with Cell 2 and the westward beam results in significantly lower SNR and reduces the range of reliable profile derivation to 12-40 km. Outside these bounds, the ratio metrics saturate the calibration meshes due to noisy photon count profiles and the measurements become unreasonable.

Another possible factor affecting the two cells differently and varying from night to night is the background due to ambient light within the receiver container, because the method of background cancellation is currently to cover the cells with thick dark blankets and any sources of light with electrical tape. Any inconsistency in these coverings could affect the background and limit the detection ranges, so a primary concern for future data acquisition will be redesigning the receiver chain to be light-tight between the interference filter and the PMTs. This design will have to account for the sensitivity of the optics near the vapor cell to the heat generated by the vapor cell, which would be conducted much more efficiently between the two if the air gaps between components are bridged using conventional, thermally conductive lens tubes.

6.4 Simulation of Background Effects

The effects of various phenomena on photon count ratios like those used to derive temperature and wind were simulated to identify the cause of the large errors that develop rapidly at the upper and lower boundaries of the region of reasonable results. After including linear and logarithmic signal strength variation due to the chopper and path loss, photon count noise, background, vertical integration, and altitude-varied smoothing such as those present in the Na-DEMOP data obtained, the background was determined to be the cause of this rapid divergence from reasonable results. Therefore, reducing the background to the minimum possible levels may help to improve future results.

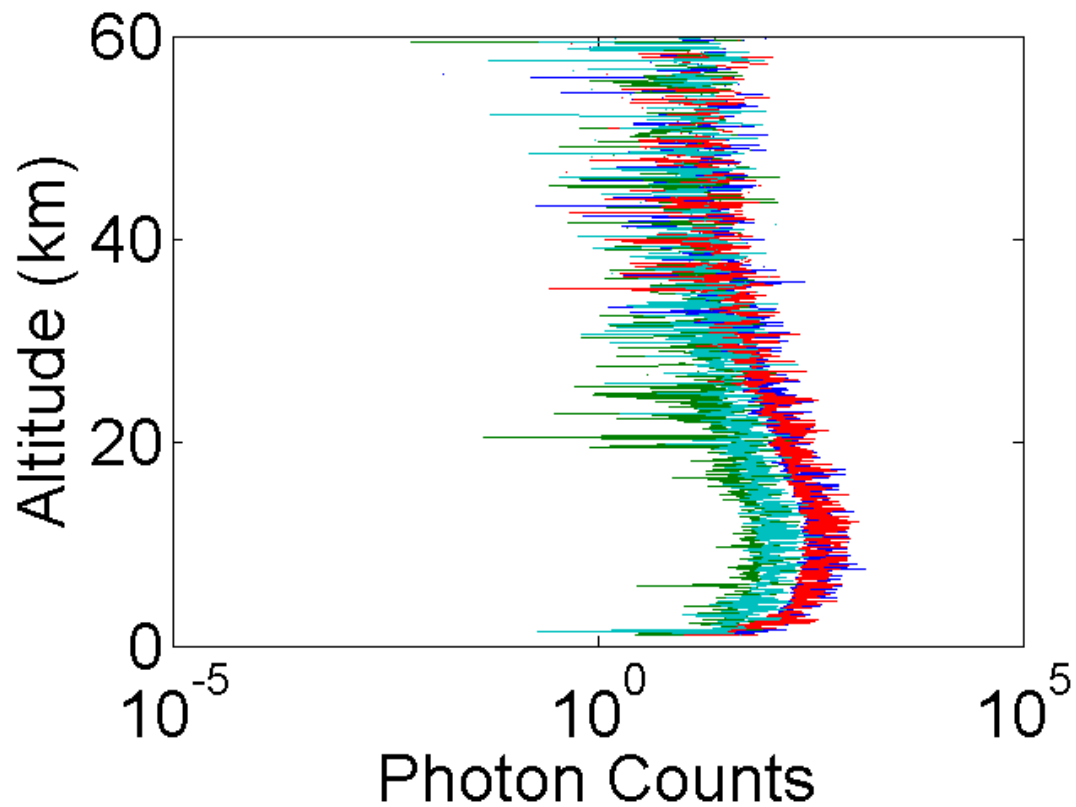


Figure 6.19: Simulated photon count profile including artificially constructed R_T and R_W ratios of 0.25 and 0.5, respectively. The logarithmic plot shows the decrease of SNR as signal strength decreases, due to photon counting noise (which increases as $\sqrt{(N)}$), and background (which is independent of signal strength).

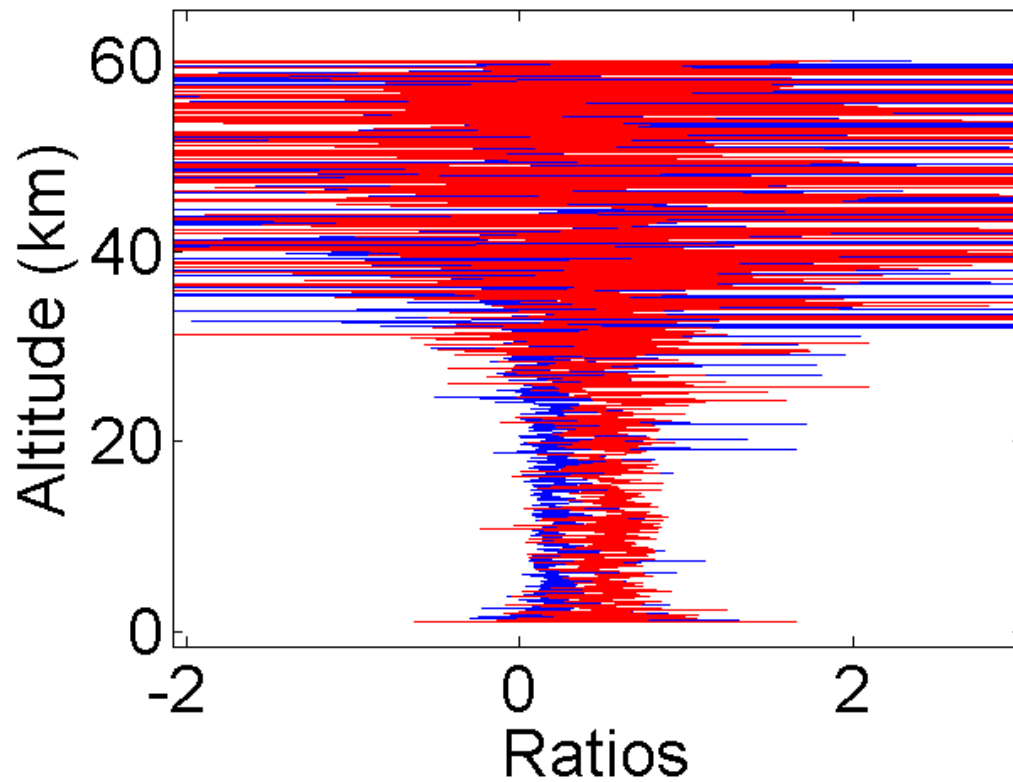


Figure 6.20: Simulated reconstruction of artificial R_T and R_W ratios of 0.25 and 0.5. It can be seen that the loss of SNR above and below a certain range carries through from the simulated raw photon counts, but it is not yet obvious that there is a bias introduced in these ratios, due to the noise.

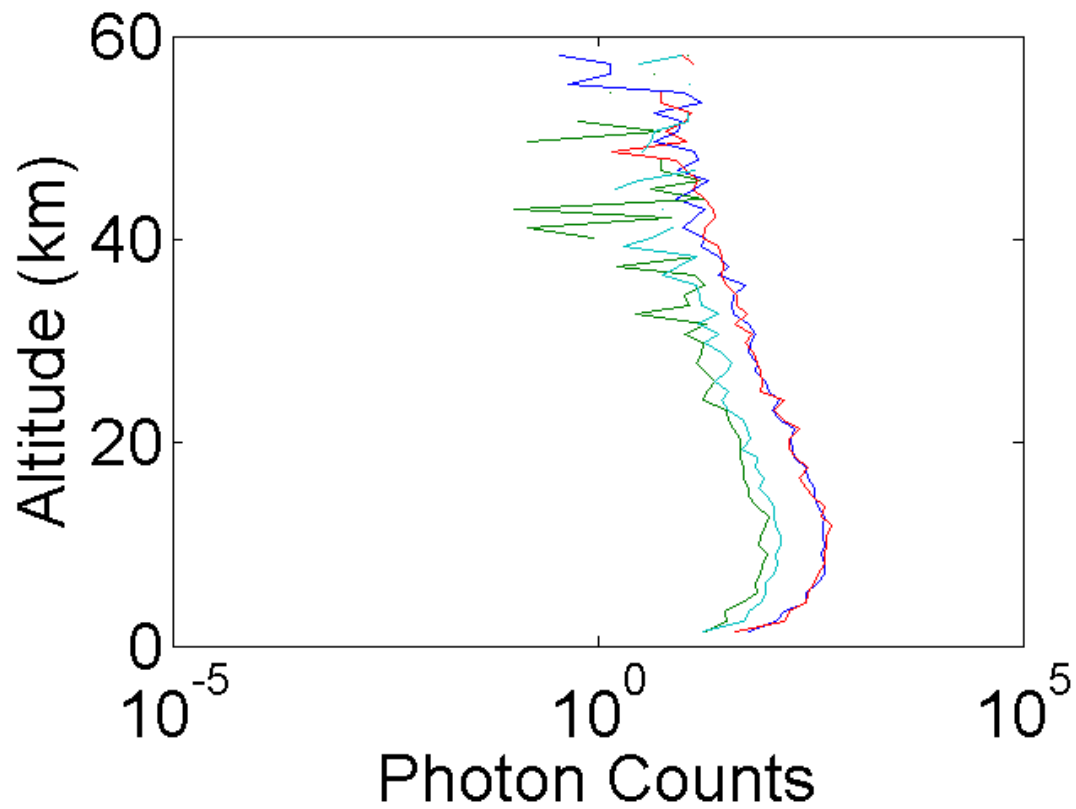


Figure 6.21: Simulated photon count profiles following vertical integration reducing the vertical resolution from 59 m to 944 m. Much of the apparent noise has been removed, but the profiles remain rough.

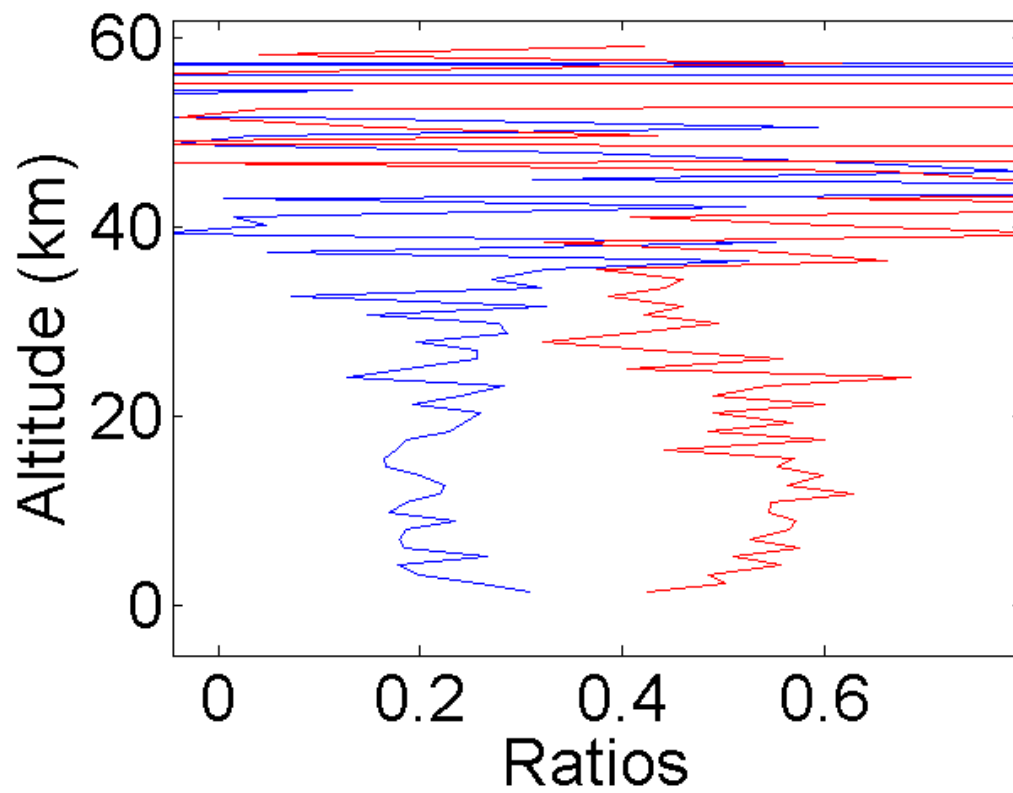


Figure 6.22: Simulated reconstruction of artificial ratios following vertical integration. The rapid divergence from the expected values can begin to be seen here, though it is not yet clear whether these divergences could be removed by smoothing.

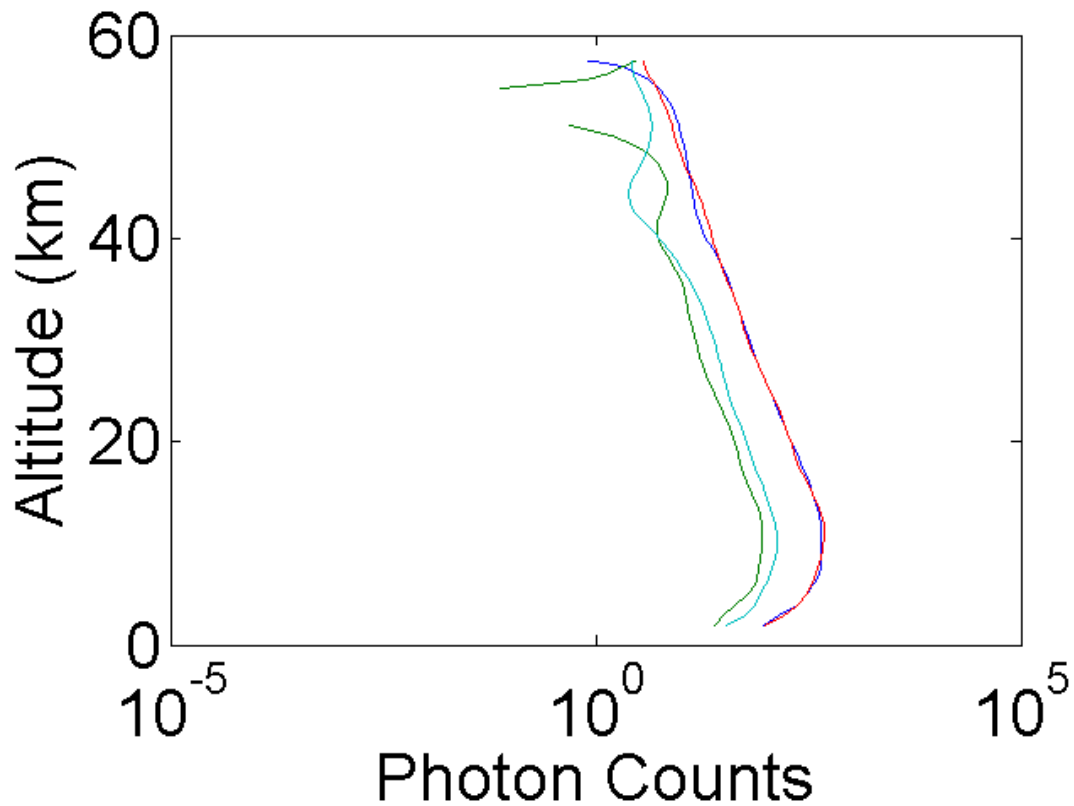


Figure 6.23: Simulated photon count profiles following smoothing with width increasing by one 944-m bin every 5 km from 0 to 30 km, inclusive. At the highest altitudes, this smoothing is clearly insufficient to maintain reasonable photon count ratios, as there is even a region in one profile which become negative after attempts to remove the background (appearing as a break in the line). At lower altitudes, however, it is not obvious that a bias remains.

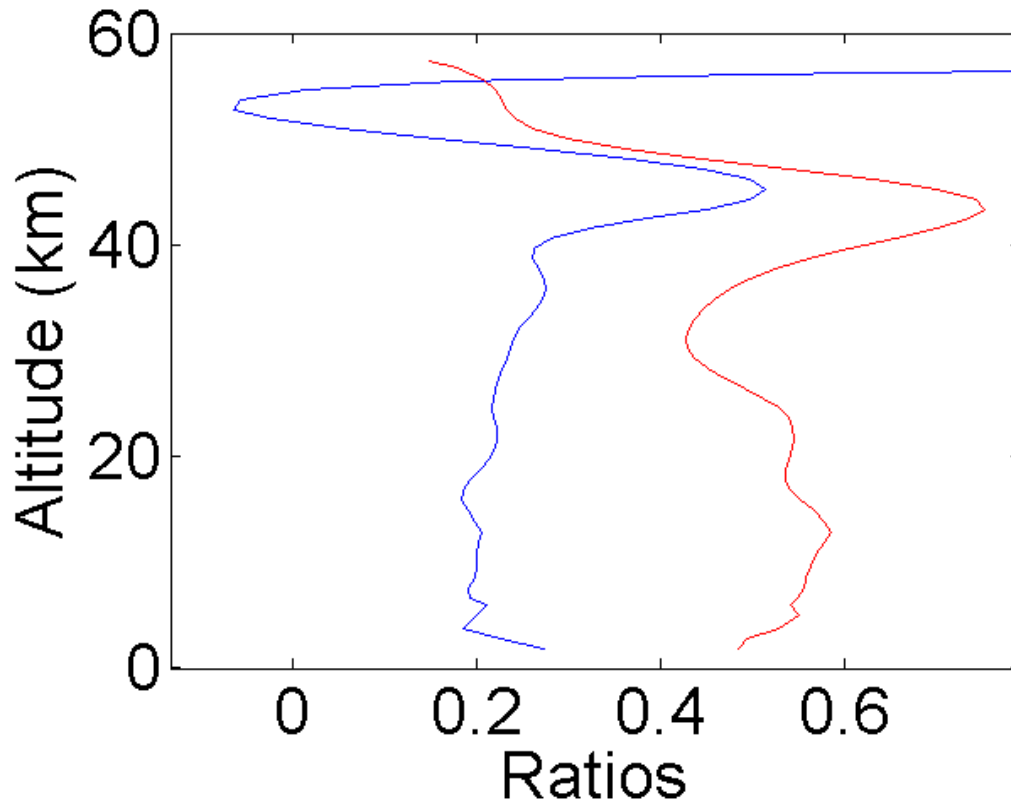


Figure 6.24: Simulated reconstruction of artificial ratios showing divergence from expected values more clearly after smoothing and integration of the photon count profiles. Although the rapid divergence at higher altitudes may be improved by wider smoothing (despite involving a full width of 7.55 km or FWHM of about 4 km by those altitudes), no amount of smoothing would eliminate the biases caused at the lower altitudes by high background levels relative to the signals. This phenomenon was not observed when only photon noise was considered (see Appendix C), implying that background is the limiting factor in the current measurements and should be minimized to expand the bounds of reasonable wind and temperature profile derivation.

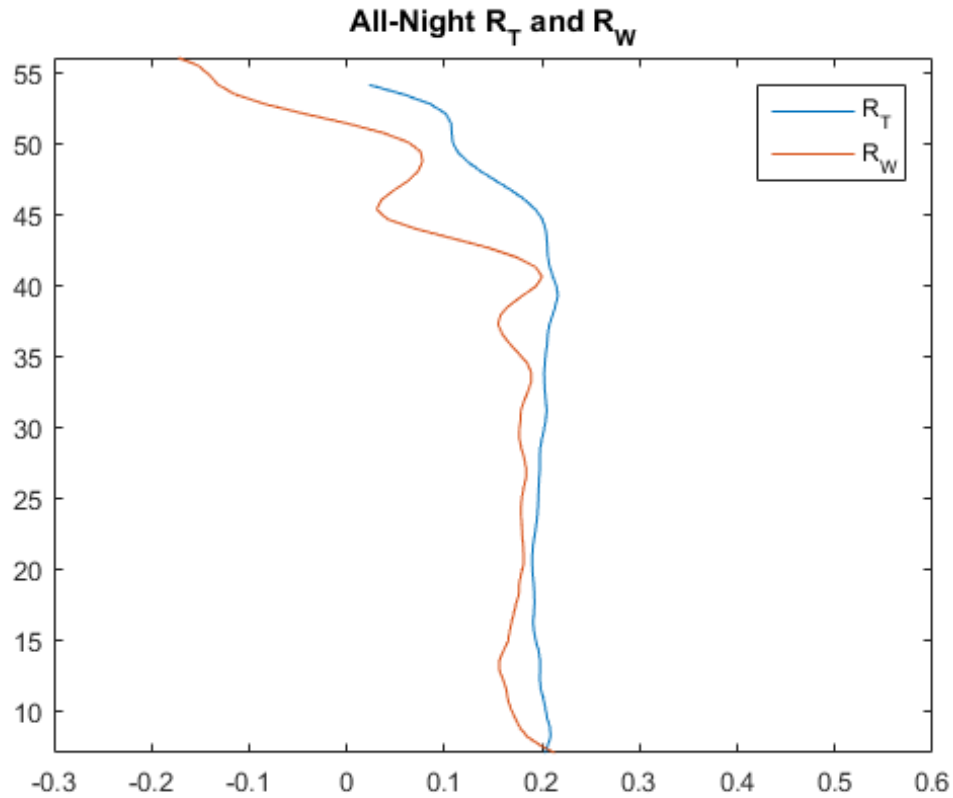


Figure 6.25: For comparison, the real ratios used for deriving the all-night westward wind and temperature profiles for 8/5/2015 shown in Figure 6.18 are plotted here. It can be seen that, although there is slight variation in the ratios at the upper altitudes where the derived profiles begin to vary more wildly, there is a much more rapid divergence of the two ratios from their average values at lower altitudes, where the derived wind profile diverges rapidly from the MSIS and radiosonde profiles and the derived temperature increases more rapidly than the MSIS model. This phenomenon, according to the simulation, appears to occur due to background biases which have greater effect as the signal strength decreases due to the chopper.

6.5 Analysis

The uncertainties in derived wind and temperature may be incomplete due to the difficulty of measuring residual background and consequent inability to determine the effects of this residual background on the ratio technique. However, these three nights of data demonstrate the capability of the Na-DEMOF to derive wind and temperature profiles reliably from 20-55 km using the STAR Na resonance-fluorescence lidar system, and they suggest the possibility of deriving these profiles from 10-70 km after improvements to the design of the receiver chain. Although these capabilities were primarily demonstrated with data integrated over an entire night of collection, reasonable profiles were also derived between 15-45 km using half-hour integration times, particularly with Cell 1 on the night of 8/5/2015. The two primary challenges to reliable derivation of profiles over this range at half-hour resolution are the background leaking into the receiver chain and the degradation of the older PMTs used for the data collected over these three nights.

The rearrangement of PMTs between 6/9/2015 and 7/26/2015 demonstrated a substantial impact on the altitude bounds of reliable wind and temperature profile derivation, as did lowering the chopper cutoff altitude to increase signal levels at lower altitudes. The simulated impacts of residual background on profiles derived using this ratio technique suggest its presence in the data collected over these three nights. Mitigation of this background by designing a light-tight but thermally insulating receiver chain, in addition to the use of undamaged PMTs, may extend the range of reliably derived wind and temperature profiles even beyond the 10-20 km bounds demonstrated here.

Chapter 7

Conclusions

In order to identify the future outlook of Na-DEMOfs as a method of deriving temperature and horizontal wind profiles, it is important to evaluate their effectiveness as a tool and to identify the challenges remaining to refine their effectiveness.

7.1 Effectiveness of DEMOf Atomic Filter

As discussed in Chapter 6, wind and temperature profiles derived using data collected with the Na-DEMOf have demonstrated reasonably low uncertainties from shot noise below 50 km (about 13 K, 16 m/s) and above 10 km (about 0.6 K, 0.8 m/s at minimum uncertainty). The profiles derived from the northward beam on 8/5/2015 in particular show that the derived profiles do not saturate the calibration meshes below 70 km and above 8 km, meaning that the photon count profiles have high enough SNR to derive reasonable temperature and wind values (with enough integration and vertical smoothing) up to the Na layer which begins to contaminate the return signals starting at 60 km.

The half-hour integrated profiles demonstrate reasonable measurements for all three nights from 20-45 km, and for the nights with lowered chopper cutoff altitude and high quantum efficiency PMTs (on Cell 1 for the northward beam) from 15-45 km. The upper limit of this range exceeds that of the nearest radiosonde station measurements by 10-15 km, and the lower limit is low enough for studies of gravity wave propagation and the transfer of momentum and energy in the lower atmosphere [2].

The Na-DEMOP allows for simultaneous temperature and horizontal wind measurements by adding two custom heated vapor cells, two PMTs, and some common optics to the receiver chain already established for a two-beam Na Doppler resonance-fluorescence lidar, without modifications to the transmitter (although 480-MHz AOMs were added alongside the existing 750-MHz AOM path to improve performance for these results) or the addition of a separate system for either temperature or wind measurements. Its application is no without challenges; calibration of the filter requires measurement of the transmission spectrum and empirical determination of calibration constants with dependence on PMT relative quantum efficiencies along with vapor cell temperature, magnetic field, and optical alignment. These calibration processes both required extensive testing and rethinking in order to arrive at the methods presented here, which in turn add time required for preparatory testing and processing of the data. Design of the vapor cells, cell heater blocks, and aluminum housings has required multiple iterations to reduce depolarization caused by mechanical stress on the cell windows, to eliminate deposition of Na atoms on the cell windows, and to extend Na cell lifetime by shortening the solid Na sample tip and coating the inside of the cell to prevent oxidation and retreat into the sample tip of the Na sample. Inclusion of a heated vapor cell into the receiver chain results in either heating of the nearby optics to temperatures near 160 °C or increased background levels allowed by air gaps close to the PMTs.

7.2 Remaining Challenges and Recommendations

The primary remaining challenge for application of the Na-DEMOP is the redesign of the receiver chain to eliminate unnecessarily high background levels by creating a light-tight path for the photons between the telescope fiber input and the PMTs. This crucial factor was omitted from earlier designs due to concerns over possible damage to or stress on the optics near the heated vapor cell caused by conduction from the cell through the light-tight lens tubes to the nearby optics. Mechanical stresses from thermal expansion of the vapor cell housing itself have already created issues with depolarization of the return photons by anisotropic birefringence from the vapor cell windows. This suggests that the final receiver chain will need to make use of thermally insulating

materials to isolate the beam path between the vapor cell and the nearby optics, rather than the typical steel lens tubes, and this may raise further difficulties of thermal expansion opening small gaps or creating stresses on the lens tubes.

A secondary improvement to the application of the Na-DEMOP to the STAR lidar system in particular is the use of new PMTs not exhibiting degradation of quantum efficiency. The older pair of PMTs significantly reduced the altitude ranges over which reasonable wind and temperature values could be derived by lowering the return signal levels. Remediation of this concern will allow for collection of reliable data from both beams and derivation of reasonable profiles for temperature and zonal and meridional winds over altitudes similar to the 15-45 km half-hour time-resolved profiles or the 8-70 km all-night profiles derived from the northward beam data collected on 8/5/2015.

Although the Na-DEMOP has allowed for reasonable derivation of radial winds and temperatures down to altitudes below 8 km, reliable and consistent measurements below 20 km will require derivation of aerosol backscattering along with temperature and wind [9]. Along with the lowered chopper cutoff altitude and reduced background from a light-tight receiver chain, measurement of aerosol presence and consideration of Rayleigh-Brillouin scattering may extend these measurements downward below 10 km.

A final recommendation is to better insulate the vapor cell housing near the sample tip to reduce the possibility of temperature fluctuations affecting the filter function. Although these temperature fluctuations were not observed during testing, this improvement may further ensure the stability of the filter function throughout the night and help extend the vapor cell lifetime by reducing temperature gradients from the cell windows to the sample tip, in turn decreasing the possibility of irreversible condensation of solid Na within the tip.

7.3 Future Outlook

The Na-DEMOP has demonstrated the capacity to derive temperatures and horizontal winds extending from low altitudes where aerosol scattering contaminates simple Rayleigh scattering to

high altitudes where the return signal is contaminated by Na resonance-fluorescence returns. This capacity makes the Na-DEMOf an exciting new technology to complement other atmospheric instruments with its ability to investigate gravity wave propagation and energy and momentum transfer through the stratosphere and mesosphere through inexpensive modifications to the receiver of a Na Doppler resonance-fluorescence lidar. After the receiver chain is redesigned to be light-tight and aerosol scattering is included in the measurement scheme, the Na-DEMOf may fully mature as an effective tool for measuring temperature and wind throughout the stratosphere and mesosphere at higher spatial and temporal resolutions over a greater range of altitudes than possible with other measurement devices. Further splitting of the return signal into standard Na Doppler receiver channels could also allow for extension of simultaneous wind and temperature measurements up into the mesosphere and lower thermosphere, bringing the possibility of a whole-atmosphere lidar closer to fruition. All told, the application of the Na-DEMOf to measurements in the lower atmosphere using three-frequency Na Doppler lidar transmitters holds exciting possibilities for the future of atmospheric science.

Bibliography

- [1] G. Agnelli, A. Cacciani, and M. Fofi. The magneto-optical filter 1: Preliminary observations in Na D lines. *Solar Physics*, 44:509–518, 1975.
- [2] M. L. Chanin, A. Hauchecorne, A. Garnier, and D. Nedeljkovic. Recent lidar developments to monitor stratosphere-troposphere exchange. *J. Atmos. Terr. Phys.*, 56:1073–1081, 1994.
- [3] Xinzhao Chu and George C. Papen. Resonance fluorescence lidar for measurements of the middle and upper atmosphere. In Takashi Fujii and Tetsuo Fukuchi, editors, *Laser Remote Sensing*. Taylor & Francis Group, 2005.
- [4] Cristina Flesia and C. Laurence Korb. Theory of the double-edge molecular technique for Doppler lidar wind measurement. *Applied Optics*, 38:432–440, 1999.
- [5] Weichun Fong, Wentao Huang, Zhangjun Wang, Brendan Roberts, Bo Tan, Chihoko Yamashita, Xinzhao Chu, T. Yuan, S. D. Harrell, and C.-Y. She. Wind and temperature from 10 to 45 km simultaneously measured with a Na-DEMOF-based 3-frequency Doppler lidar. In *25th International Laser Radar Conference Proceedings*. ILRC, 2010.
- [6] J. S. Friedman, D. Maldonado, I. Gonzalez, J. Lautenbach, X. Chu, J. A. Smith, and W. Huang. High spectral resolution test and calibration of an ultra-narrowband Faraday anomalous dispersion optical filter for use in daytime mesospheric resonance Doppler lidar. *Journal of Atmospheric and Solar-Terrestrial Physics*, 80:187–194, 2012.
- [7] S. D. Harrell, C.-Y. She, T. Yuan, D. A. Krueger, H. Chen, S. S. Chen, and Z. L. Hu. Sodium and potassium vapor Faraday filters revisited: theory and applications. *J. Opt. Soc. Am.*, 26:659–670, 2009.
- [8] Wentao Huang, Xinzhao Chu, Johannes Wiig, Bo Tan, Chihoko Yamashita, T. Yuan, J. Yue, S. D. Harrell, C.-Y. She, B. P. Williams, J. S. Friedman, and R. M. Hardasty. Field demonstration of simultaneous wind and temperature measurements from 5 to 50 km with a Na double-edge magneto-optic filter in a multi-frequency Doppler lidar. *Optics Letters*, 34:1552–1554, 2009.
- [9] Wentao Huang, Xinzhao Chu, B. P. Williams, S. D. Harrell, Johannes Wiig, and C.-Y. She. Na double-edge magneto-optic filter for na lidar profiling of wind and temperature in the lower atmosphere. *Optics Letters*, 34:199–201, 2009.
- [10] Jaya Khanna, Justin Bandoro, R. J. Sica, and C. Thomas McElroy. New technique for retrieval of atmospheric temperature profiles from Rayleigh-scatter lidar measurements using nonlinear inversion. *Applied Optics*, 51:7945–7952, 2012.

- [11] C. Laurence Korb, Bruce M. Gentry, and Chi Y. Weng. Edge technique: theory and application to the lidar measurement of atmospheric wind. Applied Optics, 31:4202–4213, 1992.
- [12] M. Kuntz. A new implementation of the Humlicek algorithm for the calculation of the Voigt profile function. J. Quant. Spectrosc. Radiat. Transfer, 57:819–824, 1997.
- [13] F. Schreier. The Voigt and complex error function: A comparison of computational methods. J. Quant. Spectrosc. Radiat. Transfer, 48:743–762, 1992.
- [14] Chiao-Yao She, Jia Yue, Zhao-Ai Yan, Johnathan W. Hair, Jin-Jia Guo, Song-Hua Wu, and Zhi-Shen Liu. Direct-detection Doppler wind measurements with a Cahannes-Mie lidar: A. comparison between iodine vapor filter and Fabry-Perot interferometer methods. Applied Optics, 46:4434–4443, 2007.
- [15] John A. Smith and Xinzhao Chu. High-efficiency receiver architecture for resonance-fluorescence and Doppler lidars. Applied Optics, 54:3173–3184, 2015.
- [16] John A. Smith and Xinzhao Chu. Investigation of field-widened Mach-Zehnder receiver to extend Fe Doppler lidar wind measurements from the thermosphere to the ground. Applied Optics (submitted), 2015.
- [17] Leda Sox, Vincent B. Wickwar, Chad Fish, and Joshua P. Herron. Rayleigh scatter lidar observations of the midlatitude mesosphere’s response to sudden stratospheric warmings. In Space Grant Consortium Symposium. NASA, 2014.
- [18] Toshitaka Tsuda. Characteristics of atmospheric gravity waves observed using the MU (middle and upper atmosphere) radar and GPS (Global Positioning System) radio occultation. In Proceedings of the Japan Academy Ser. B, volume 90. The Japan Academy, 2014.
- [19] Bifford P. Williams and Steven Tomczyk. Magneto-optic Doppler analyzer: a new instrument to measure mesopause winds. Applied Optics, 35:6494–6503, 1996.

Appendix A

Additional Error Simulation Results

The following figures display the results of the simulation described in Section 6.4, with the background noise removed, in order to demonstrate the dependence of the phenomenon of wild profile divergence at upper and lower boundaries upon the presence of background noise. Photon noise is still present in these results.

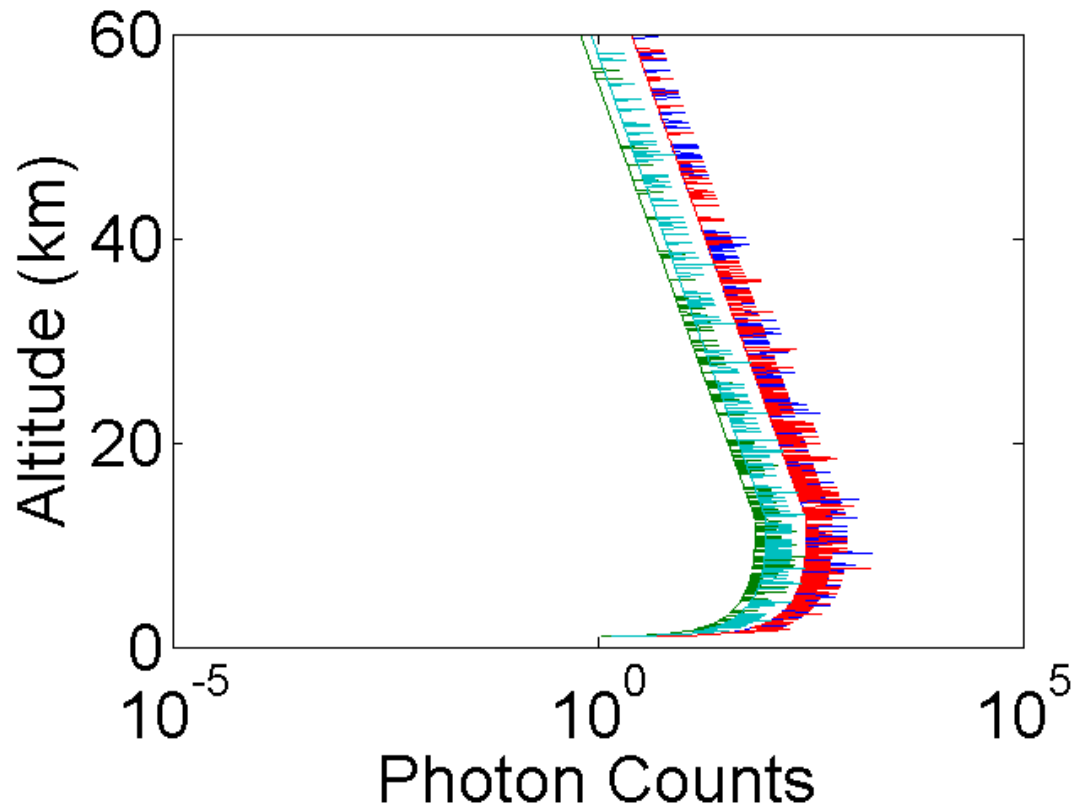


Figure A.1: Simulated photon count profile including artificially constructed R_T and R_W ratios of 0.25 and 0.5, respectively. The logarithmic plot shows that photon noise actually increases with signal strength, although SNR does still increase with increasing signal levels due to the relatively slow rise in noise levels.

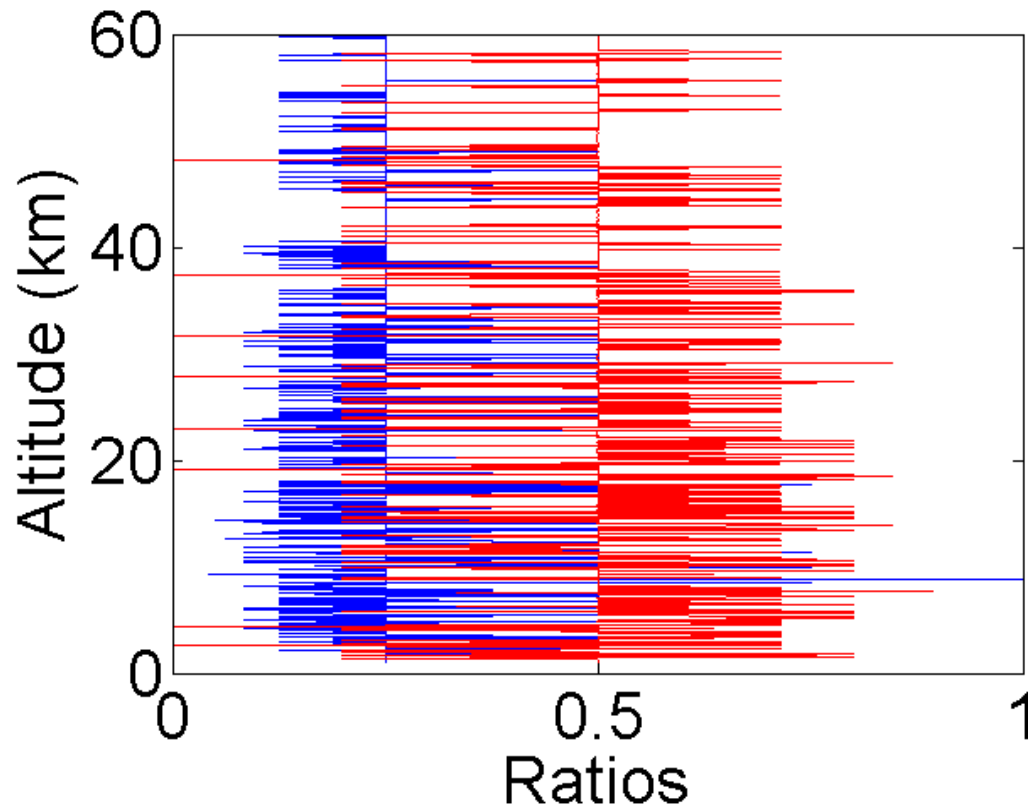


Figure A.2: Simulated reconstruction of artificial R_T and R_W ratios of 0.25 and 0.5. It is not clear from this plot whether or not there is a bias introduced at any altitude range, although the lower middle altitudes with higher signal strength have greater noise.

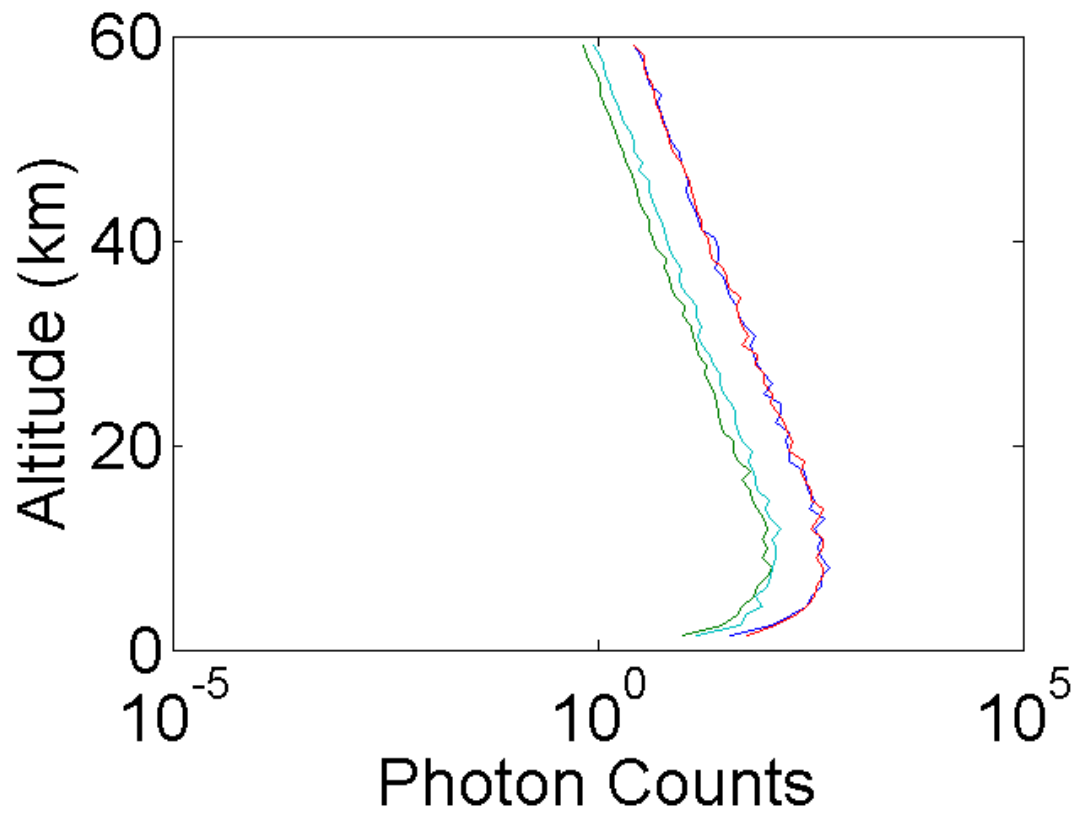


Figure A.3: Simulated photon count profiles following vertical integration reducing the vertical resolution from 59 m to 944 m. Much of the apparent noise has been removed, but the profiles remain rough.

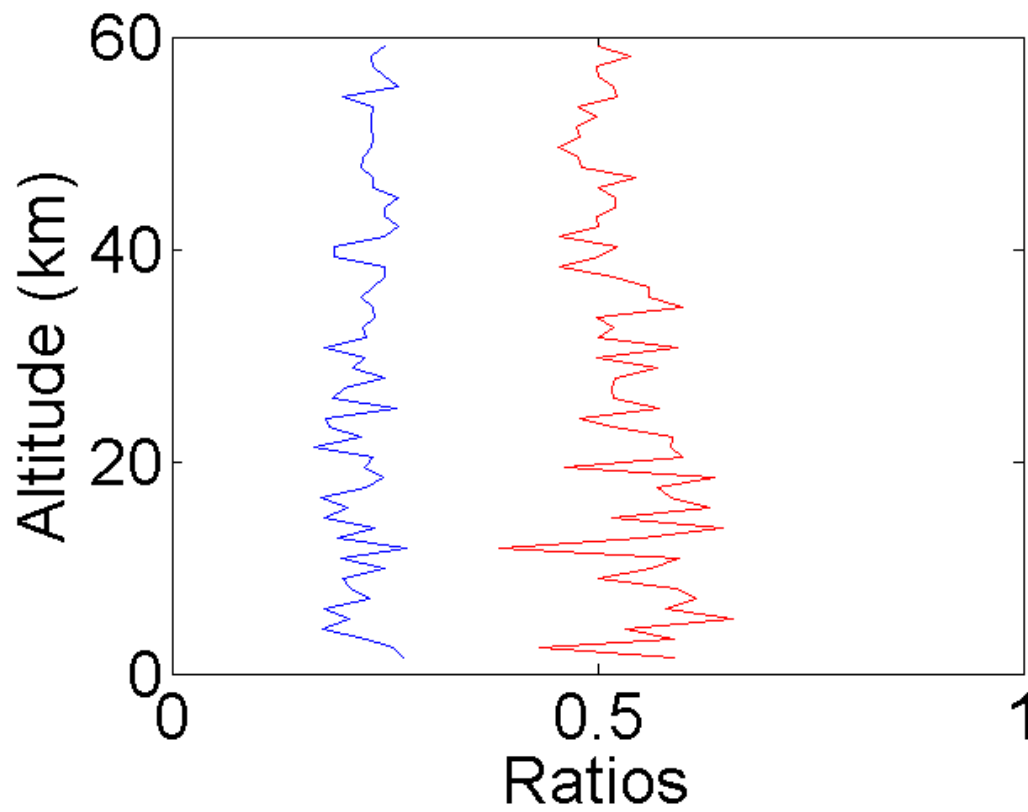


Figure A.4: Simulated reconstruction of artificial ratios following vertical integration. There appear to be no biases introduced already, despite the noisy variations in each constant.

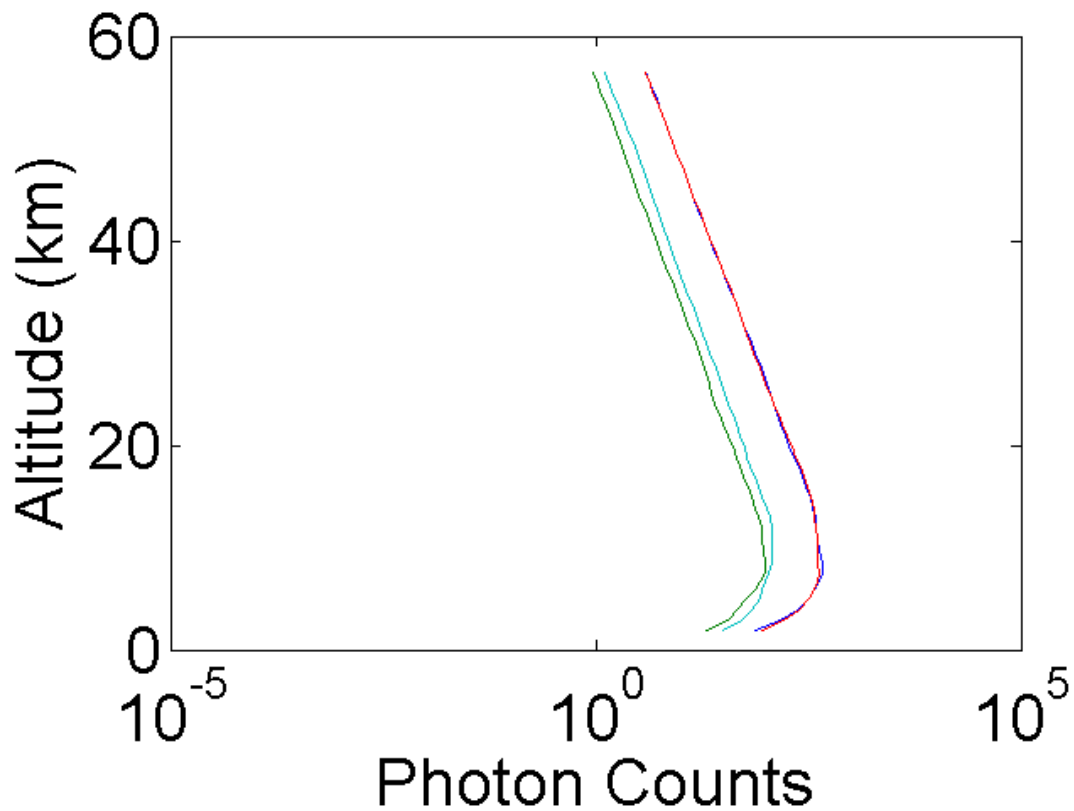


Figure A.5: Simulated photon count profiles following smoothing with width increasing by one 944-m bin every 5 km from 0 to 30 km, inclusive. The photon count profiles, at least, are smooth, and appear to exhibit constant ratios above the altitude where the chopper has finished opening.

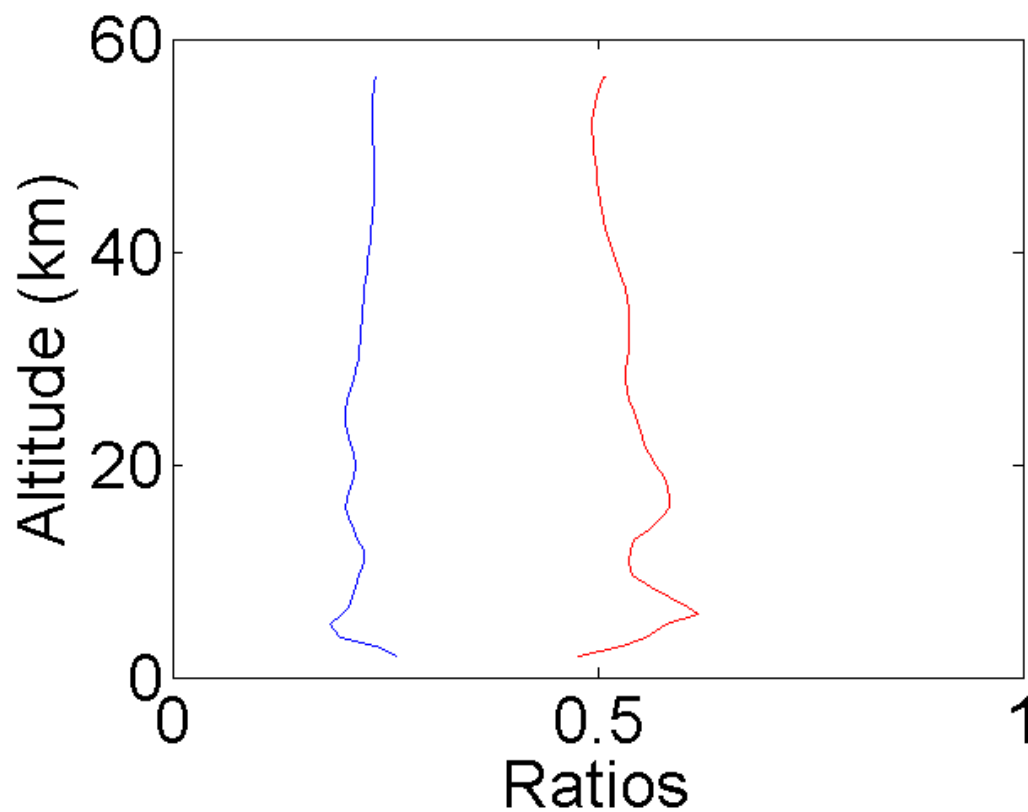


Figure A.6: Simulated reconstruction of artificial ratios showing divergence from expected values more clearly after smoothing and integration of the photon count profiles. No rapid divergence like that seen in the real data and the simulations including background is visible here, indicating that background levels are limiting the accuracy of the derived wind and temperature profiles in the current configuration of the Na-DEMOP

Appendix B

Off-Zenith Beam Alignment

In order to obtain measurements of zonal and meridional winds, it is necessary to align two off-zenith beams. The measurements presented in this thesis are aligned to the north and west, with an elevation angle of 70° to compromise between two competing factors: the reduction of signal strength at a given altitude and the improved sensitivity of wind measurements to horizontal winds with reduced elevation angle.

The method used for this alignment involves an amateur astronomical telescope with an adapter for holding a DSLR camera, used to verify alignment of the beam by localization within the star field, and a sight scope mounted to the collecting telescopes, for guidance in aligning the telescopes to the beam.

The telescope with mounted camera can be focused, and the camera field of view determined, by imaging of the moon or other similarly distant and easily identified astronomical objects. The images in this appendix come from an imaging setup with a field of view roughly 1° across on the narrower side.

Figures B.1 and B.2 show images of the beam used to confirm proper alignment.

Figures B.3 and B.4 show the star fields visible with 1° field of view, predicted by the Stellarium amateur astronomy and star map software.

Proper alignment of the beams can be achieved roughly at first by comparison of the apparent end of the beam seen with the naked eye to constellations or other reference objects in the sky, such as the moon or visible planets. The beam's alignment must then be iteratively refined using

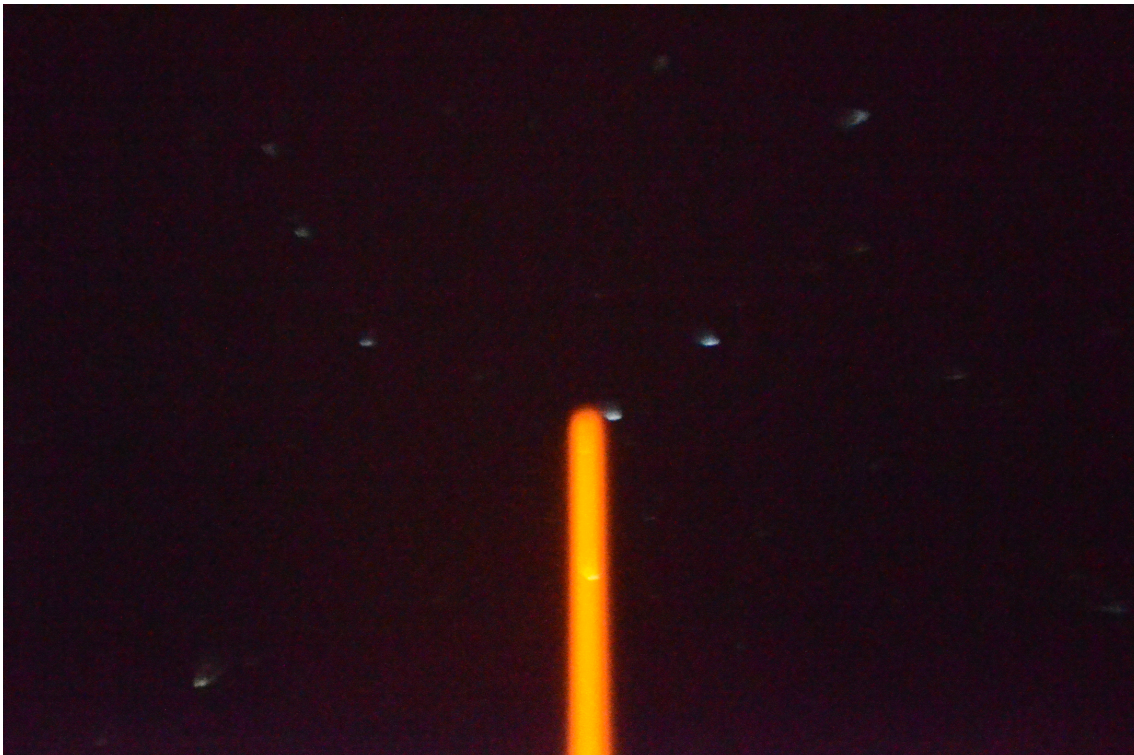


Figure B.1: Photograph of northward beam through telescope.



Figure B.2: Photograph of westward beam through telescope.

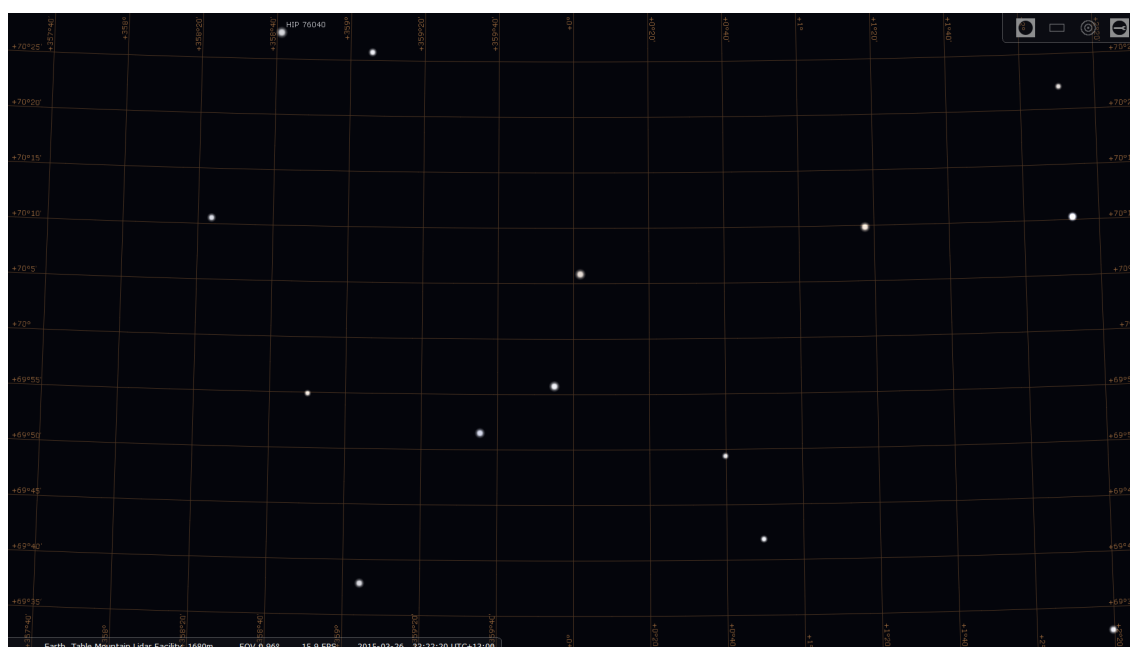


Figure B.3: Star field predicted for northward beam using Stellarium star map software.

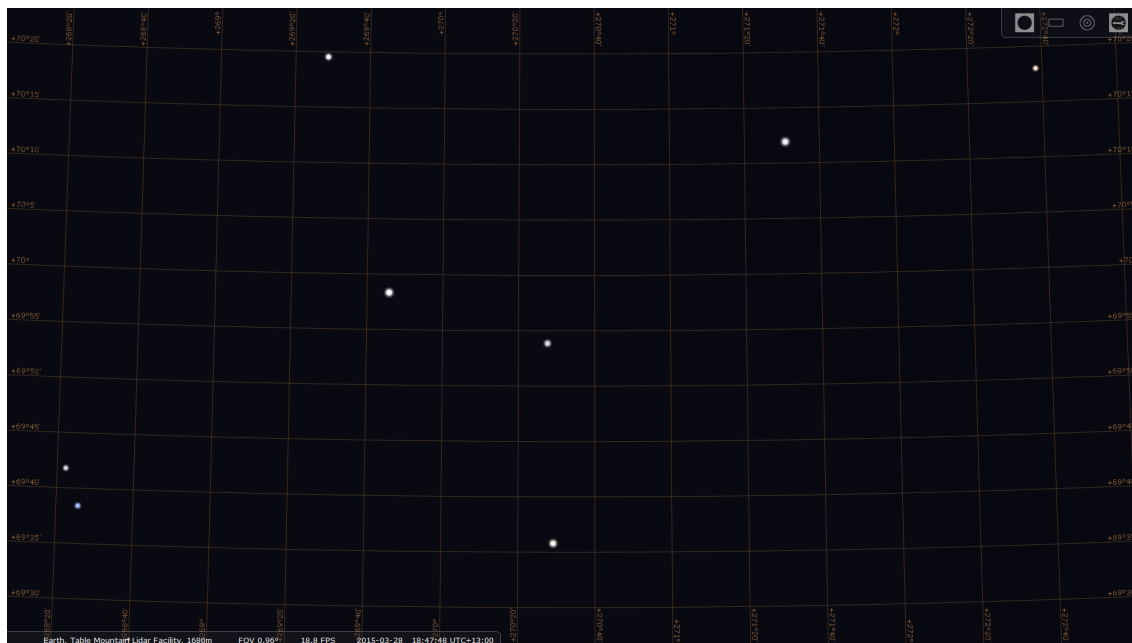


Figure B.4: Star field predicted for westward beam using Stellarium star map software.

the amateur astronomy telescope and camera to check the location of the apparent beam tip within the star field shown in the Stellarium software.

Figures B.5 and B.6 show the beam photographs superimposed on the predicted star fields to allow for confirmation of alignment and precise measurement of the azimuth and elevation of each beam.

One source of error in this method is the drift of stars through the camera field of view during exposure. Figures B.1 and B.2 exhibit motion blur corresponding to a 5-second exposure time, while Figures B.7 and B.8 show the star field drift predicted by Stellarium over one-minute periods. This motion blur over a 5-second exposure time can result in alignment determination errors of up to one minute or 0.3 mrad in either azimuth or elevation angles for the westward beam, or of 2 minutes (0.5 mrad) only in azimuth angle for the northward beam.

The other dominant source of error is in localizing the tip of the beam. The apparent beam width within the star field at an elevation angle of 70° can be determined, by comparison to the Stellarium azimuthal grid as in Figure B.9, to be 7 minutes (2 mrad) in azimuth, and 2 minutes (0.6 mrad) in elevation angle. The uncertainties given in Table B.1 reflect the quadrature sum of these two uncertainties.

Table B.1: Beam alignment results obtained on 3/26/2015 (northward beam) and 3/27/2015 (westward beam).

Beam	Elevation	Uncertainty	Azimuth	Uncertainty
North	$69^\circ 55'$	2'	$359^\circ 59'$	7'
West	$69^\circ 52'$	2'	$269^\circ 58'$	7'

After aligning the off-zenith laser beams, it is possible to align the receiving telescopes to optimize light collection from the beam tips. The sight scope mounted on each telescope must be aligned to the telescope's field of view when the beam and telescope are both still pointed toward zenith. Then, after alignment of the beams, the telescopes may be adjusted so that the beam tip appears in the sight scope the same way it did during zenith sight scope calibration. This provides

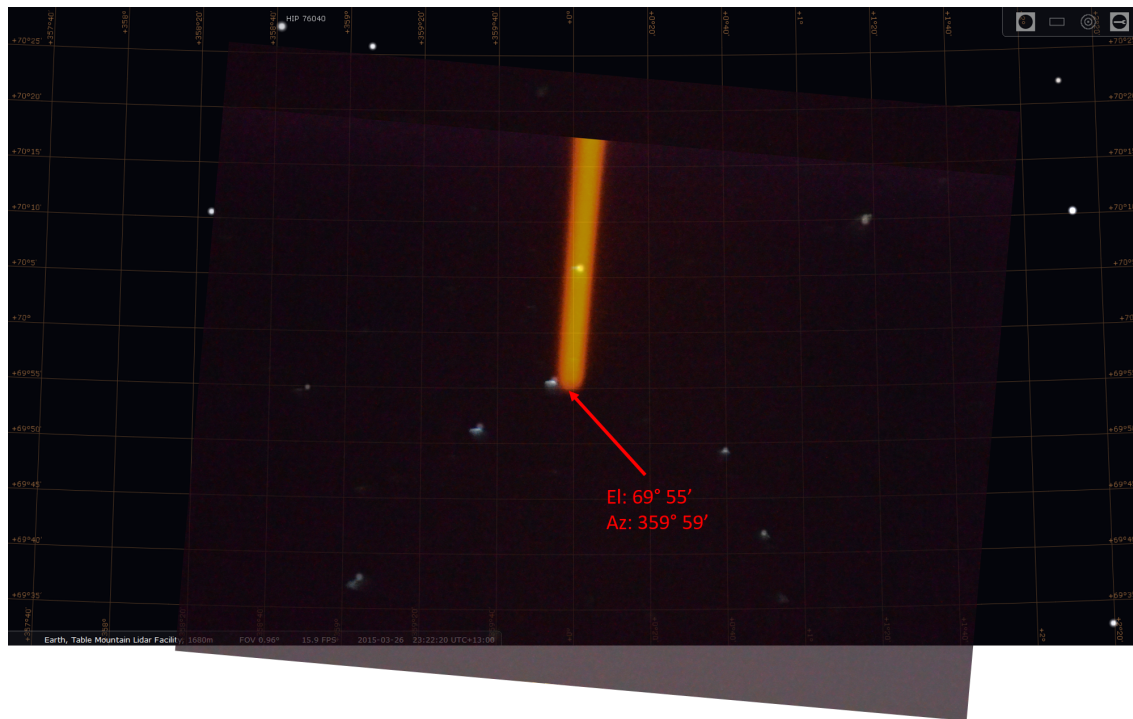


Figure B.5: Overlay of photo from northward beam onto Stellarium screenshot corresponding to UTC 10:22:10 AM on March 26, 2015.

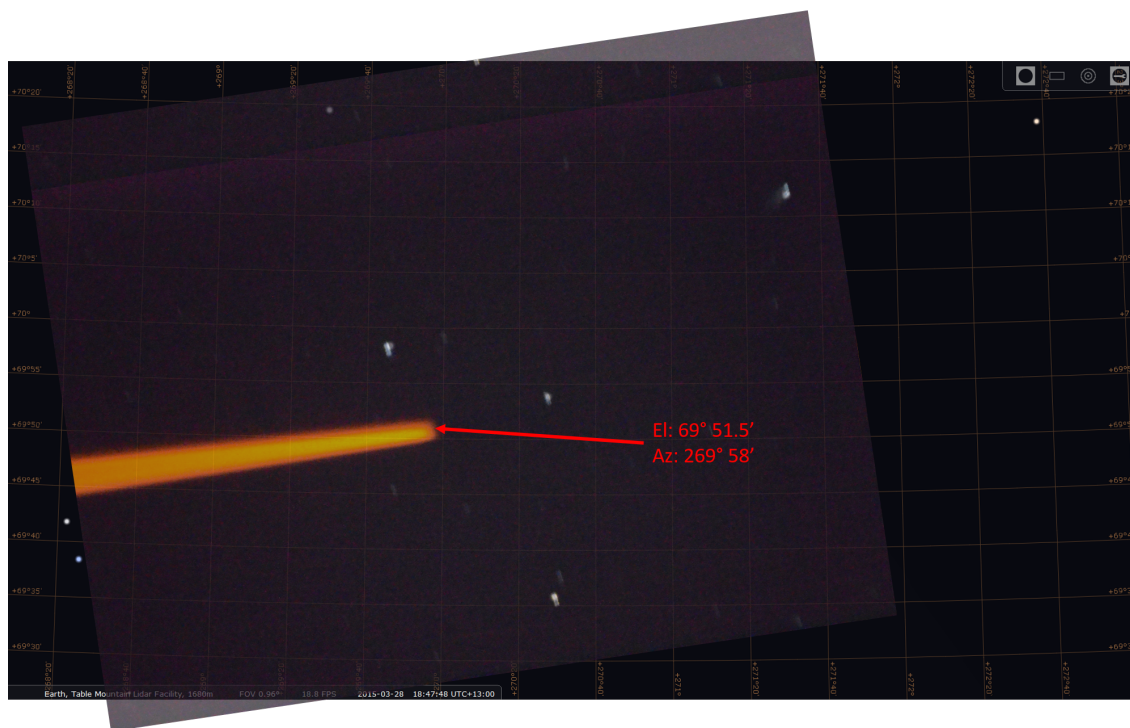


Figure B.6: Overlay of photo from westward beam onto Stellarium screenshot corresponding to UTC 5:47:48 AM on March 27, 2015.



Figure B.7: Drift of star field predicted by Stellarium over sixty seconds while observing northward beam.

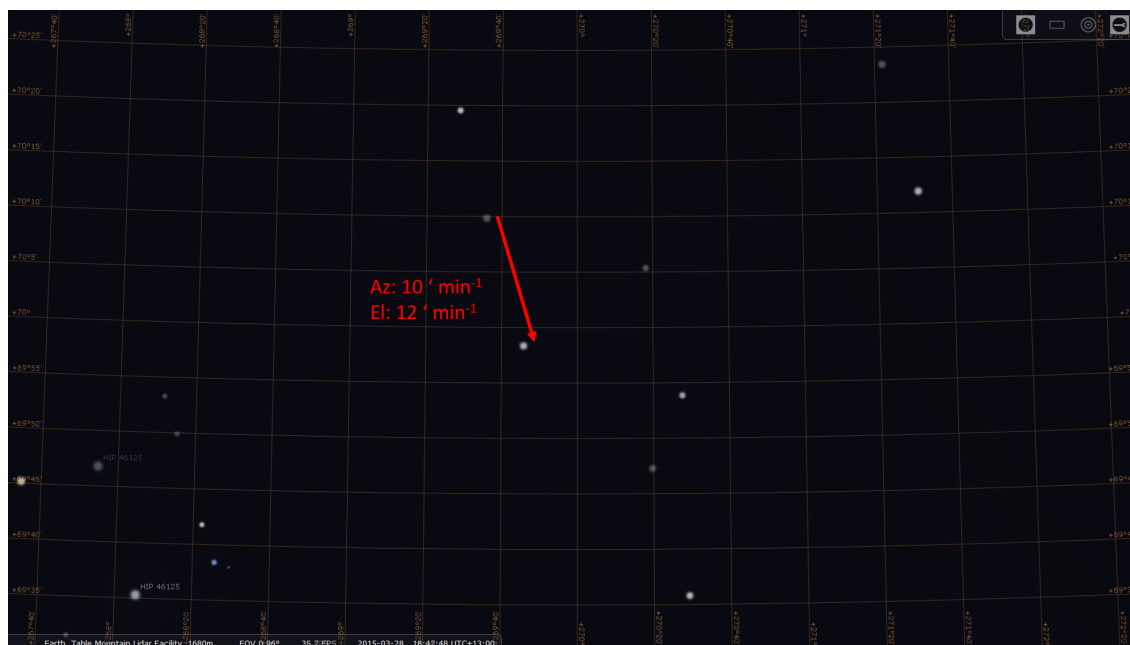


Figure B.8: Drift of star field predicted by Stellarium over sixty seconds while observing westward beam.

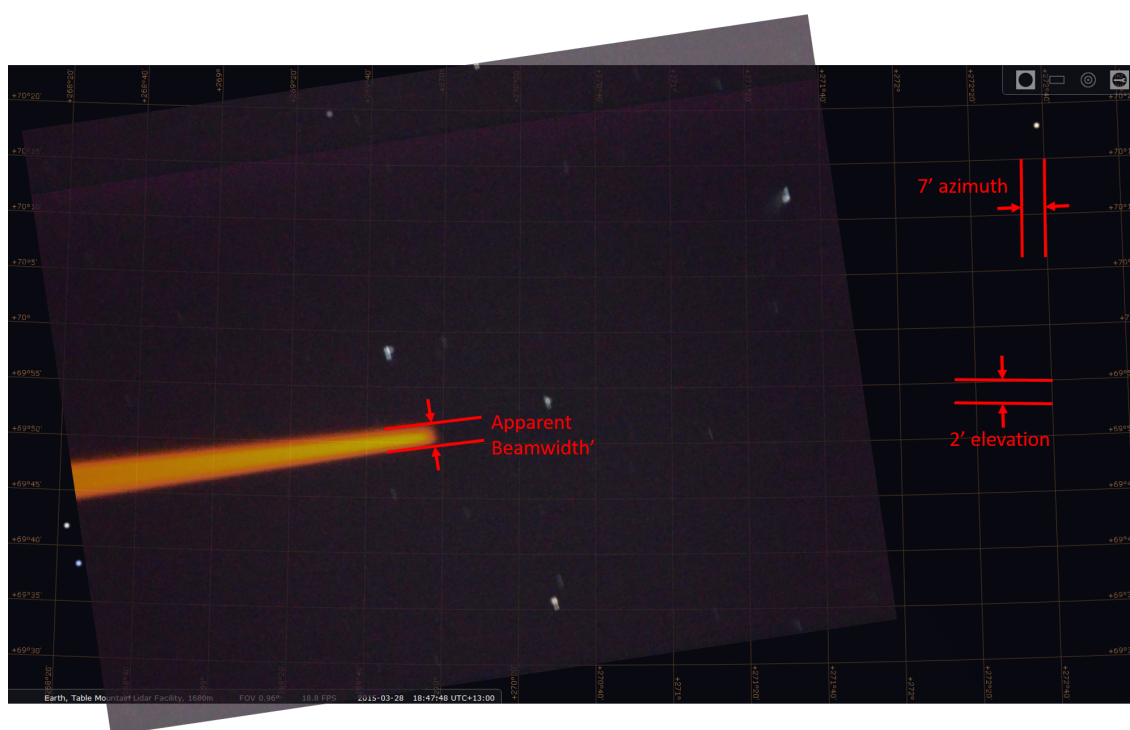


Figure B.9: Measurement of beamwidth of westward beam by comparison to Stellarium azimuthal grid.

coarse telescope alignment that can be refined by replacing the optical fiber output of the telescope with a camera to see where in the telescope's field of view the beam tip falls. Aligning the telescope to center the beam tip within the field of view completes the system off-zenith alignment. The signal levels obtained can be further optimized by adjusting the beam pointing very finely during data collection, although this may require a new confirmation of the beam alignment against the star field.

Appendix C

IDL Simulation Code

This IDL code simulates the effects of a magnetic field on the transmission of wavelengths near the Na D2a line through the heated Na vapor cell. It is based on an algorithm developed by Sean D. Harrell and David A. Krueger for simulating the Faraday anomalous dispersion filter, and was modified by Wentao Huang for the simulation of the Na-DEMOF filter.

```
;Code modified from original FaradayFilter3.pro on 20130910
;Found that the N or K was added a space after in this IDL version, so changed the
code to if atom eq 'X '
;Changed the output saving directory

;FaradayFilterOriginal.pro
;March 24, 2008
;Written by Sean D. Harrell and David A. Krueger
;This program calculates Faraday Filter transmission, Faraday Rotation, and
Susceptability for
;Sodium and Potassium vapor Faraday Filters
;This program accompanies "Sodium and potassium vapor Faraday filters re-visited:
Theory and applications"
;S. D. Harrell, C.-Y. She, Tao Yuan, David A. Krueger, H.L. Chen, S.S. Chen, Z.L.Hu
;In preparation for JOSA B
```



```

;Structure of program

;PRO Constants

;FUNCTION ComplexVoigt, delE, nuobs, nuDoppler, delnuNatural

;FUNCTION NaDensity,      tempV, tempP

;FUNCTION KDensity,      tempV, tempP

;PRO denweight,          ES1_2, kBoltz, hPlanck, tempV, rho0

;PRO F1F2delED1,        a, b, E, F1F2D1, rho0, delED1, rhoOD1

;PRO F1F2delED2,        a, b, E, F1F2D2, rho0, delED2, rhoOD1

;PRO Hamiltonian2X1_2,  muBB, muNB, AJ, BJ, E1_2, B1_2

;PRO Hamiltonian2P3_2, muBB, muNB, AJ, BJ, E3_2, B3_2, flag

; main program

PRO Constants

;initializes variables used in the program

COMMON Const, AJ2S1_2, AJ2P1_2, BJ1_2, AJ2P3_2, BJ2P3_2, gammaD1, gammaD2, $
gmuBBS1_2, gmuBBP1_2, gmuBBP3_2, constD1, constD2, nuDopplerD1, $
nuDopplerD2, LambdaD1, LambdaD2, Length, flag, multiplier, gI, $
MuN, gImuNB, kBoltz, tempV, tempP, hPlanck, Bfield, atom, abundance, imag

;choose whether to use Na or K for calculation

atom='N'

read, 'please choose sodium or potassium (sodium=N, potassium=K, cr=N)', atom

;read in filter parameters: magnetic field, tip and vapor temperatures, and cell
length

default = 'n'

```

```

Length= 4.0

if default eq 'n' then read, 'what vapor length (cm)?', Length
print, ' vapor length (cm) ', Length

Bfield=2300.

if ( default eq 'n' ) then $
read, ' Magnetic field? (Gauss) ', Bfield
print, ' Magnetic Field (Gauss) = ', Bfield

tempV=430. ;cell temperature
tempP=435. ;tip temperature

if ( default eq 'n' ) then begin
read, 'Cell Temperature? (K)', tempV
read, 'Tip Temperature? (K)', tempP
endif

print, ' Cell Temperature? (K)', tempV
print, ' Tip Temperature? (K)', tempP

;the following values are fundamental constants

MuBohr = 9.270154e-21 ;erg/Gauss = Bohr Magneton
hPlanck = 6.6260755e-27 ;erg sec = Planck's constant
MuN = 7.62259371e-7 ;GHz/Gauss = Nuclear Magneton
kBoltz = 1.380658e-23 ;J/K

MuGHperGauss= (MuBohr /hPlanck) * 1.0e-9 ;GHz/Gauss = Bohr Magneton in units
of GHz/Gauss

;the gJ values are independent of the species, since both Na and K have the same
J, S, and L values

```

;see paper, Appendix II

gJS1_2 = 2. & gJP1_2 = 2./3 & gJP3_2 = 4./3

gmuBBS1_2 = gJS1_2 * MuGHperGauss * Bfield

gmuBBP1_2 = gJP1_2 * MuGHperGauss * Bfield

gmuBBP3_2 = 1 * MuGHperGauss * Bfield ;gJP3_2 is included in

Hamiltonian2P3_2 program

;since there are more than one isotope for K, set up arrays for values that are different depending on the isotope

mass = replicate(0.0, 2)

abundance = replicate(0.0, 2) ; the first element of this array shouldn't be left at zero

AJ2S1_2 = replicate(0.0, 2)

AJ2P1_2 = replicate(0.0, 2)

BJ1_2 = replicate(0.0, 2)

AJ2P3_2 = replicate(0.0, 2)

BJ2P3_2 = replicate(0.0, 2)

gI = replicate(0.0, 2)

if atom eq 'K ' then begin ;calculate potassium constants

;values for mass, abundance, hyperfine constants, and gI for each isotope are a 1x2 array

;so i=0 is for K39, i=1 is for K41

mass(0) = 38.963707 * 1.6605402e-27 ;for the A=39 Isotope of K

abundance(0) = 0.9326 ;abundance for the A=39 Isotope of K

mass(1) = 40.961825 * 1.6605402e-27 ;for the A=41 Isotope of K from Krane

abundance(1) = 0.0673 ;abundance for the A=41 Isotope of K from Krane

```

LambdaD1    = 770.108           ; (nm) potassium D1
LambdaD2    = 766.701           ; (nm) potassium D2

;hyperfine structure constants A and B
;There are two sets of values, for the two isotopes of K

;first the values for K39
AJ2S1_2(0)   = 0.2308598601     ; GHz = 230.8598601 MHz
AJ2P1_2(0)   = 0.027775         ; GHz = 27.775 MHz
BJ1_2(0)     = 0.0
AJ2P3_2(0)   = 0.006093         ; GHz = 6.093 MHz
BJ2P3_2(0)   = 0.002786         ; GHz = 2.786 MHz

;Now values for K41
AJ2S1_2(1)   = 0.1270069352     ; GHz = 127.0069352 MHz
AJ2P1_2(1)   = 0.015245         ; GHz = 15.245 MHz
BJ1_2(1)     = 0.0
AJ2P3_2(1)   = 0.003363         ; GHz = 3.363 MHz
BJ2P3_2(1)   = 0.003351         ; GHz = 3.351 MHz

;gamma = nat.linewidth=A/(2*pi)
;AD1  = 0.382e8 s^-1
;AD2  = 0.387e8 s^-1
gammaD1   = 0.00608             ; GHz = 6.08 MHz
gammaD2   = 0.00616             ; GHz = 6.16 MHz

;nuclear Lande-g factors
gI(0)    = 0.26099
gI(1)    = 0.1432543

```

```

;vapor density
VDensity = KDensity(tempV,tempP)
print, ' Vapor Density ', VDensity

;linestrength
S=51.6; atomic units (calculated from NIST website data)
endif

if atom eq 'N ' then begin ;calculate sodium constants
;again,values for mass, abundance, hyperfine constants, and gI for each isotope
are a 1x2 array
;since there is only one stable isotope, Na23, we'll only use the i=0 spot
;leave i=1 set to 0.0
mass(0) = 22.989768 * 1.6605402e-27 ; kg for sodium
abundance(0) = 1 ;only one stable isotope
LambdaD1 = 589.7558 ; (nm) sodium D1
LambdaD2 = 589.1582 ; (nm) sodium D2

;Hyperfine structure constants A and B
AJ2S1_2(0) = 0.8858130644 ; GHz = 855.8130644 MHz
AJ2P1_2(0) = 0.0944 ; GHz = 94.4 MHz
BJ1_2(0) = 0.0
AJ2P3_2(0) = 0.018572 ; GHz = 18.572 MHz
BJ2P3_2(0) = 0.002723 ; GHz = 2.723 MHz

```

```

;AD2=0.616e8 s^-1

;gamma=nat.linewidth=A/(2*pi)

gammaD1    = 0.00977 ;   GHz    = 9.77 MHz
gammaD2    = 0.00980 ;   GHz    = 9.80 MHz

;Nuclear Lande-g factor
gI(0) = 1.478392

;vapor density
VDensity = NaDensity(tempV,tempP)
print, ' Vapor Density ', VDensity

;linestrength
S=37.3; atomic units (calculated from NIST website data)
endif

;DopplerVel is the same as u in the JOSA B paper, equation 14
DopplerVel = replicate(0.0,2)
DopplerVel(0) = sqrt( 2.* kBoltz * tempV/ mass(0)) ;Note this is array
DopplerVel(1) = sqrt( 2.* kBoltz * tempV/ mass(1))

;convert this velocity into frequency
nuDopplerD1 = replicate(0.0, 2)
nuDopplerD2 = replicate(0.0, 2)
nuDopplerD1(0) = DopplerVel(0)/ LambdaD1 ; GHz = (m/sec)/nm
nuDopplerD2(0) = DopplerVel(0)/ LambdaD2
nuDopplerD1(1) = DopplerVel(1)/ LambdaD1 ; GHz = (m/sec)/nm

```

```

nuDopplerD2(1) = DopplerVel(1)/ LambdaD2

print, ' The default is exact calc for D2 excited state energies, i.e. flag = 1'
print, ' The high magnetic field approximation uses only diagonal 2P3/2
Hamiltonian terms'
print, ' If flag = 0 then the program will use the high magnetic field approx'
read, ' which value of flag do you want? (0=hiField, 1=exact) ', flag
print, ' flag (0=hiField, 1=exact) = ', flag
print, 'The default includes the small nuclear magnetic dipole terms, if
multiplier=0, these will be ignored'
read, 'which value of multiplier do you want? (0=ignore muN, 1=use muN) ',
multiplier

if (multiplier eq 1) then begin
print, 'Using nuclear dipole terms in calculation of eigenvalues.'
endif else begin
print, 'Ignoring nuclear dipole terms in calculation of eigenvalues.'
endelse

gImuNB = replicate(0.0,2)
gImuNB = gI *MuN *Bfield *multiplier

;constant terms in chi :=VDensity*imag*S0*(D1 or D2
factor)/2*epsillon0*hPlanckBar*sqrt(pi)*nuDoppler
;Include all factors independent of transition and integral, as detailed in the
Appendices
;the following calculates this constant for D1 and D2

```

;this is the same for Na and K

epsilon0 =8.854e-12 ; C²/(N*m²)

;S0=S*e²*a0²/2, e=1.602e-19 C, a0=bohrradius=0.5292e-10 m

echarge =1.602e-19 ;C = electron charge

a0 =0.5292e-10 ;m = Bohr radius

imag=complex(0,1.) ;imaginary unit

;break up the calculation to avoid overflows

c1 =VDensity*1.e6*imag*S/2

ca =echarge*a0

cb =epsilon0*hPlanck

cc =ca/cb

c2 =cc/(1.e-7/(2.*!pi))

c3 =echarge*a0

c4 =2.*sqrt(!pi)

;the D1 and D2 factors are from the 3-j and 6-j symbols-- See JOSA B paper Appendix

D1Factor =2./9.

D2Factor =4./3.

constD1 = COMPLEXARR(2)

constD1(0) =c1*c2*c3*D1Factor/(c4*nuDopplerD1(0)*1.e9)

constD1(1) =c1*c2*c3*D1Factor/(c4*nuDopplerD1(1)*1.e9)

constD2 = COMPLEXARR(2)

constD2(0) =c1*c2*c3*D2Factor/(c4*nuDopplerD2(0)*1.e9)

constD2(1) =c1*c2*c3*D2Factor/(c4*nuDopplerD2(1)*1.e9)

return

end

```

FUNCTION ComplexVoigt, delE, nuobs, nuDoppler, delnuNatural
;This function sets up the Faddeeva function (Complex function, of which the real
part is the Voigt)
X   = REFORM( ( nuobs - delE)/ nuDoppler ) ;removes all dimensions of size 1
Y   = 0.5* delnuNatural/   nuDoppler
if ( Y lt 0.0 ) then stop
XABS   = abs( X )
;now call the procedure which actually calculates the Faddeeva function
call_Procedure, 'HUMLICEK', XABS, Y, PRBFCT
ComVoigt   = PRBFCT
index = WHERE ( X lt 0.0, num )
if ( num gt 0 ) then ComVoigt(index) = CONJ(PRBFCT(index))
; real Faddeeva is even in freq
; imag Faddeeva is odd in freq
RETURN, ComVoigt
end

```

```

FUNCTION NaDensity, tempV, tempP
;This function is designed to calculate the Na vapor density which gives the
;number of atoms per cm3. It needs cell and tip temperatures in K.

term1=71.899-9217.2/TempP
term2=40693000/(TempP*TempP*TempP)
term3=0.0061264*TempP-9.6625*ALOG(TempP)

```

```
Den = (9.654e18/tempV)*exp(ALOG(10)*(term1+term2+term3))
return, Den
end
```

```
FUNCTION KDensity, tempV, tempP
;This function is designed to calculate the K vapor density which gives the
;number of atoms per cm3. It needs cell and tip temperatures in K.
```

```
term1=69.53-10486/TempP
term2=1.8658e8/(TempP*TempP*TempP)
term3=0.0027286*TempP-8.5732*ALOG(TempP)
```

```
Den = (9.654e18/tempV)*exp(ALOG(10)*(term1+term2+term3))

return, Den
end
```

```
PRO denweight, ES1_2, kBoltz, hPlanck, tempV, rho0
;this procedure calculates the density weighting factor in eq. 17
Energy=ES1_2*(1.e9)*(hPlanck*1.e-7) ;converts eigenvalues from frequency GHz to
energy in Joules
kBoltzT=kBoltz*tempV
Boltzfact=replicate(0.0,9) ;remember 0 element in array is unused
for i=1,8 do begin
Boltzfact(i)=exp(-Energy(i)/(kBoltz*tempV)) ; computes the Boltzmann Factor for
each ground state
```

```

endfor

Z=TOTAL(Boltzfact,/DOUBLE)      ;calculates Partition function

rho0 = replicate(0.0,9)

for i=1,8 do begin
rho0(i)=Boltzfact(i)/Z
endifor

end

PRO F1F2delED1, a, b, ED, rho0, F1F2, delE, rho0D1

;this procedure calculates the energy eigenvalues, and eigenket coefficients for
the D1 transition

F1F2      = Replicate(0.0,2,13) ;eigenket coefficients
delE      = Replicate(0.0,2,13) ;energy eigenvalues
rho0D1    = Replicate(0.0,2,13) ;ground state density weighting factor

;   first index:  0 = sigma-; 1 = sigma+ polarizations
;   second index: 1,2,...12 for the 12 transitions
;   (note the (*,0) is an ignored placeholder in the array)
;   for the eigenket coefficients the second index is given by
;
;           0      1      2      3 for
;   m_J values= -1.5  -0.5   0.5   1.5
; so only indices 1 and 2 are used for the D1 energy levels

;   so a2-   goes to a(2,1) and a2+   goes to a(2,2)   and
;   b5-   goes to b(5,1) and b5+   goes to b(5,2)
;   note that within 2S1/2 and 2P1/2 submanifolds the energies decrease as index
increases

;   note that E(2) > E(3); E(4) > E(5); E(6) > E(7) (taking + sqrt first)

```

; the $ED(i,j) = E_{excited}(i) - E_{ground}(j)$
 ; $\rho_{0D1}(i,k) = \rho_0(j=1..8)$, with j corresponding to $E_{ground}(j)$, i is sigma
 +/-, and k is same as $F1F2(*,k)$

; first the sigma - transitions

$$\text{delE}(0,1) = ED(2,1) \quad \& \quad F1F2(0,1) = b(2,1)^2 \quad \&$$

$$\rho_{0D1}(0,1) = \rho_0(1)$$

$$\text{delE}(0,2) = ED(3,1) \quad \& \quad F1F2(0,2) = b(3,1)^2 \quad \&$$

$$\rho_{0D1}(0,2) = \rho_0(1)$$

$$\text{delE}(0,3) = ED(4,2) \quad \& \quad F1F2(0,3) = a(2,2)^2 * b(4,1)^2 \quad \&$$

$$\rho_{0D1}(0,3) = \rho_0(2)$$

$$\text{delE}(0,4) = ED(5,2) \quad \& \quad F1F2(0,4) = a(2,2)^2 * b(5,1)^2 \quad \&$$

$$\rho_{0D1}(0,4) = \rho_0(2)$$

$$\text{delE}(0,5) = ED(4,3) \quad \& \quad F1F2(0,5) = a(3,2)^2 * b(4,1)^2 \quad \&$$

$$\rho_{0D1}(0,5) = \rho_0(3)$$

$$\text{delE}(0,6) = ED(5,3) \quad \& \quad F1F2(0,6) = a(3,2)^2 * b(5,1)^2 \quad \&$$

$$\rho_{0D1}(0,6) = \rho_0(3)$$

$$\text{delE}(0,7) = ED(6,4) \quad \& \quad F1F2(0,7) = a(4,2)^2 * b(6,1)^2 \quad \&$$

$$\rho_{0D1}(0,7) = \rho_0(4)$$

$$\text{delE}(0,8) = ED(7,4) \quad \& \quad F1F2(0,8) = a(4,2)^2 * b(7,1)^2 \quad \&$$

$$\rho_{0D1}(0,8) = \rho_0(4)$$

$$\text{delE}(0,9) = ED(6,5) \quad \& \quad F1F2(0,9) = a(5,2)^2 * b(6,1)^2 \quad \&$$

$$\rho_{0D1}(0,9) = \rho_0(5)$$

$$\text{delE}(0,10) = ED(7,5) \quad \& \quad F1F2(0,10) = a(5,2)^2 * b(7,1)^2 \quad \&$$

$$\rho_{0D1}(0,10) = \rho_0(5)$$

$$\text{delE}(0,11) = ED(8,6) \quad \& \quad F1F2(0,11) = a(6,2)^2 \quad \&$$

$$\rho_{0D1}(0,11) = \rho_0(6)$$

$$\begin{aligned} \text{delE}(0,12) &= \text{ED}(8,7) \ \& \ \text{F1F2}(0,12) = a(7,2)^2 \ \& \\ \text{rho0D1}(0,12) &= \text{rho0}(7) \end{aligned}$$

; now for the sigma + transitions

$$\begin{aligned} \text{delE}(1,1) &= \text{ED}(1,2) \ \& \ \text{F1F2}(1,1) = a(2,1)^2 \ \& \\ \text{rho0D1}(1,1) &= \text{rho0}(2) \end{aligned}$$

$$\begin{aligned} \text{delE}(1,2) &= \text{ED}(1,3) \ \& \ \text{F1F2}(1,2) = a(3,1)^2 \ \& \\ \text{rho0D1}(1,2) &= \text{rho0}(3) \end{aligned}$$

$$\begin{aligned} \text{delE}(1,3) &= \text{ED}(2,4) \ \& \ \text{F1F2}(1,3) = a(4,1)^2 * b(2,2)^2 \ \& \\ \text{rho0D1}(1,3) &= \text{rho0}(4) \end{aligned}$$

$$\begin{aligned} \text{delE}(1,4) &= \text{ED}(3,4) \ \& \ \text{F1F2}(1,4) = a(4,1)^2 * b(3,2)^2 \ \& \\ \text{rho0D1}(1,4) &= \text{rho0}(4) \end{aligned}$$

$$\begin{aligned} \text{delE}(1,5) &= \text{ED}(2,5) \ \& \ \text{F1F2}(1,5) = a(5,1)^2 * b(2,2)^2 \ \& \\ \text{rho0D1}(1,5) &= \text{rho0}(5) \end{aligned}$$

$$\begin{aligned} \text{delE}(1,6) &= \text{ED}(3,5) \ \& \ \text{F1F2}(1,6) = a(5,1)^2 * b(3,2)^2 \ \& \\ \text{rho0D1}(1,6) &= \text{rho0}(5) \end{aligned}$$

$$\begin{aligned} \text{delE}(1,7) &= \text{ED}(4,6) \ \& \ \text{F1F2}(1,7) = a(6,1)^2 * b(4,2)^2 \ \& \\ \text{rho0D1}(1,7) &= \text{rho0}(6) \end{aligned}$$

$$\begin{aligned} \text{delE}(1,8) &= \text{ED}(5,6) \ \& \ \text{F1F2}(1,8) = a(6,1)^2 * b(5,2)^2 \ \& \\ \text{rho0D1}(1,8) &= \text{rho0}(6) \end{aligned}$$

$$\begin{aligned} \text{delE}(1,9) &= \text{ED}(5,7) \ \& \ \text{F1F2}(1,9) = a(7,1)^2 * b(5,2)^2 \ \& \\ \text{rho0D1}(1,9) &= \text{rho0}(7) \end{aligned}$$

$$\begin{aligned} \text{delE}(1,10) &= \text{ED}(4,7) \ \& \ \text{F1F2}(1,10) = a(7,1)^2 * b(4,2)^2 \ \& \\ \text{rho0D1}(1,10) &= \text{rho0}(7) \end{aligned}$$

$$\begin{aligned} \text{delE}(1,11) &= \text{ED}(6,8) \ \& \ \text{F1F2}(1,11) = b(6,2)^2 \ \& \\ \text{rho0D1}(1,11) &= \text{rho0}(8) \end{aligned}$$

$$\begin{aligned} \text{delE}(1,12) &= \text{ED}(7,8) \ \& \ \text{F1F2}(1,12) = b(7,2)^2 \ \& \end{aligned}$$

```

rho0D1(1,12)=rho0(8)

return

end

PRO F1F2delED2, a, b, ED, rho0, F1F2, delE, rho0D2

;this procedure calculates the energy eigenvalues, and eigenket coefficients for
the D2 transition

F1F2      = Replicate(0.0,2,23) ;eigenket coefficients
delE      = Replicate(0.0,2,23) ;energy eigenvalues
rho0D2    = Replicate(0.0,2,23) ;ground state density weighting factor
;      first index: 0,1 for sigma- and sigma+ polarizations respectively
;      second index: 1,2,...22 for the 22 transitions
;      (note the (*,0) is an ignored placeholder in the array)
; for the a's and the b's
;      m_J value = -1.5   -0.5   0.5   1.5 has index
;                  0      1      2      3
;      so a2-   goes to a(2,1) and a2+   goes to a(2,2)   and
;      b7-1.5 goes to b(7,0) and b7-0.5 goes to b(7,1)
; note that within 2P3/2 submanifolds the energies increase as index increases
;      i.e. E(4) < E(5) < E(6) for 2P3/2
;      (assuming they are dominated by magnetic field term)
; note that within 2S1/2 and 2P1/2 submanifolds
;      the energies decrease as index increases
;      note that E(2) > E(3); E(4) > E(5); E(6) > E(7) (taking + sqrt first)
;      yes, they are ordered differently
;      the ED(i,j) = Eexcited(i) - Eground(j)

```

; rho0D1(i,k) = rho0(j=1...8), with j corresponding to Eground(j), i is sigma +/-, k is same as F1F2(*,k)

; first the sigma - transitions

$$F1F2(0,1) = b(4,1)^2 * (1/12.) \& delE(0,1) = ED(4,1) \& rho0D2(0,1)=rho0(1)$$

$$F1F2(0,2) = b(5,1)^2 * (1/12.) \& delE(0,2) = ED(5,1) \& rho0D2(0,2)=rho0(1)$$

$$F1F2(0,3) = b(6,1)^2 * (1/12.) \& delE(0,3) = ED(6,1) \& rho0D2(0,3)=rho0(1)$$

$$F1F2(0,4) = a(2,1)^2 * b(7,0)^2 * (1/4.) + a(2,2)^2 * b(7,1)^2 * (1/12.)$$

$$delE(0,4) = ED(7,2) \& rho0D2(0,4)=rho0(2)$$

$$F1F2(0,5) = a(3,1)^2 * b(7,0)^2 * (1/4.) + a(3,2)^2 * b(7,1)^2 * (1/12.)$$

$$delE(0,5) = ED(7,3) \& rho0D2(0,5)=rho0(3)$$

$$F1F2(0,6) = a(2,1)^2 * b(8,0)^2 * (1/4.) + a(2,2)^2 * b(8,1)^2 * (1/12.)$$

$$delE(0,6) = ED(8,2) \& rho0D2(0,6)=rho0(2)$$

$$F1F2(0,7) = a(3,1)^2 * b(8,0)^2 * (1/4.) + a(3,2)^2 * b(8,1)^2 * (1/12.)$$

$$delE(0,7) = ED(8,3) \& rho0D2(0,7)=rho0(3)$$

$$F1F2(0,8) = a(2,1)^2 * b(9,0)^2 * (1/4.) + a(2,2)^2 * b(9,1)^2 * (1/12.)$$

$$delE(0,8) = ED(9,2) \& rho0D2(0,8)=rho0(2)$$

$$F1F2(0,9) = a(3,1)^2 * b(9,0)^2 * (1/4.) + a(3,2)^2 * b(9,1)^2 * (1/12.)$$

$$delE(0,9) = ED(9,3) \& rho0D2(0,9)=rho0(3)$$

$$F1F2(0,10) = a(2,1)^2 * b(10,0)^2 * (1/4.) + a(2,2)^2 * b(10,1)^2 * (1/12.)$$

$$delE(0,10) = ED(10,2) \& rho0D2(0,10)=rho0(2)$$

$$F1F2(0,11) = a(3,1)^2 * b(10,0)^2 * (1/4.) + a(3,2)^2 * b(10,1)^2 * (1/12.)$$

$$delE(0,11) = ED(10,3) \& rho0D2(0,11)=rho0(3)$$

$$F1F2(0,12) = a(4,1)^2 * b(11,0)^2 * (1/4.) + a(4,2)^2 * b(11,1)^2 * (1/12.)$$

$$delE(0,12) = ED(11,4) \& rho0D2(0,12)=rho0(4)$$

$$F1F2(0,13) = a(5,1)^2 * b(11,0)^2 * (1/4.) + a(5,2)^2 * b(11,1)^2 * (1/12.)$$

```

delE(0,13)= ED(11,5)      &   rhoOD2(0,13)=rho0(5)
F1F2(0,14)= a(4,1)^2* b(12,0)^2* (1/4.) + a(4,2)^2* b(12,1)^2* (1/12.)
delE(0,14)= ED(12,4)      &   rhoOD2(0,14)=rho0(4)
F1F2(0,15)= a(5,1)^2* b(12,0)^2* (1/4.) + a(5,2)^2* b(12,1)^2* (1/12.)
delE(0,15)= ED(12,5)      &   rhoOD2(0,15)=rho0(5)
F1F2(0,16)= a(4,1)^2* b(13,0)^2* (1/4.) + a(4,2)^2* b(13,1)^2* (1/12.)
delE(0,16)= ED(13,4)      &   rhoOD2(0,16)=rho0(4)
F1F2(0,17)= a(5,1)^2* b(13,0)^2* (1/4.) + a(5,2)^2* b(13,1)^2* (1/12.)
delE(0,17)= ED(13,5)      &   rhoOD2(0,17)=rho0(5)
F1F2(0,18)= a(6,1)^2* b(14,0)^2* (1/4.) + a(6,2)^2* b(14,1)^2* (1/12.)
delE(0,18)= ED(14,6)      &   rhoOD2(0,18)=rho0(6)
F1F2(0,19)= a(7,1)^2* b(14,0)^2* (1/4.) + a(7,2)^2* b(14,1)^2* (1/12.)
delE(0,19)= ED(14,7)      &   rhoOD2(0,19)=rho0(7)
F1F2(0,20)= a(6,1)^2* b(15,0)^2* (1/4.) + a(6,2)^2* b(15,1)^2* (1/12.)
delE(0,20)= ED(15,6)      &   rhoOD2(0,20)=rho0(6)
F1F2(0,21)= a(7,1)^2* b(15,0)^2* (1/4.) + a(7,2)^2* b(15,1)^2* (1/12.)
delE(0,21)= ED(15,7)      &   rhoOD2(0,21)=rho0(7)
F1F2(0,22)= (1/4.)          &   delE(0,22) = ED(16,8)      &
rhoOD2(0,22)=rho0(8)

```

; now for the sigma + transitions

```

F1F2(1,1) = (1/4.)          &   delE(1,1) = ED(1,1)      &   rhoOD2(1,1)=rho0(1)
F1F2(1,2) = a(2,1)^2* b(2, 2)^2* (1/12.)+ a(2,2)^2* b(2,3)^2* (1/4.)
delE(1,2) = ED(2,2)          &   rhoOD2(1,2)=rho0(2)
F1F2(1,3) = a(3,1)^2* b(2, 2)^2* (1/12.)+ a(3,2)^2* b(2,3)^2* (1/4.)
delE(1,3) = ED(2,3)          &   rhoOD2(1,3)=rho0(3)
F1F2(1,4) = a(2,1)^2* b(3, 2)^2* (1/12.)+ a(2,2)^2* b(3,3)^2* (1/4.)

```


$$\begin{aligned}
\text{delE}(1,4) &= \text{ED}(3,2) && \& \text{rhoOD2}(1,4)=\text{rho0}(2) \\
\text{F1F2}(1,5) &= a(3,1)^2 * b(3,2)^2 * (1/12.) + a(3,2)^2 * b(3,3)^2 * (1/4.) \\
\text{delE}(1,5) &= \text{ED}(3,3) && \& \text{rhoOD2}(1,5)=\text{rho0}(3) \\
\text{F1F2}(1,6) &= a(4,1)^2 * b(4,2)^2 * (1/12.) + a(4,2)^2 * b(4,3)^2 * (1/4.) \\
\text{delE}(1,6) &= \text{ED}(4,4) && \& \text{rhoOD2}(1,6)=\text{rho0}(4) \\
\text{F1F2}(1,7) &= a(5,1)^2 * b(4,2)^2 * (1/12.) + a(5,2)^2 * b(4,3)^2 * (1/4.) \\
\text{delE}(1,7) &= \text{ED}(4,5) && \& \text{rhoOD2}(1,7)=\text{rho0}(5) \\
\text{F1F2}(1,8) &= a(4,1)^2 * b(5,2)^2 * (1/12.) + a(4,2)^2 * b(5,3)^2 * (1/4.) \\
\text{delE}(1,8) &= \text{ED}(5,4) && \& \text{rhoOD2}(1,8)=\text{rho0}(4) \\
\text{F1F2}(1,9) &= a(5,1)^2 * b(5,2)^2 * (1/12.) + a(5,2)^2 * b(5,3)^2 * (1/4.) \\
\text{delE}(1,9) &= \text{ED}(5,5) && \& \text{rhoOD2}(1,9)=\text{rho0}(5) \\
\text{F1F2}(1,10) &= a(4,1)^2 * b(6,2)^2 * (1/12.) + a(4,2)^2 * b(6,3)^2 * (1/4.) \\
\text{delE}(1,10) &= \text{ED}(6,4) && \& \text{rhoOD2}(1,10)=\text{rho0}(4) \\
\text{F1F2}(1,11) &= a(5,1)^2 * b(6,2)^2 * (1/12.) + a(5,2)^2 * b(6,3)^2 * (1/4.) \\
\text{delE}(1,11) &= \text{ED}(6,5) && \& \text{rhoOD2}(1,11)=\text{rho0}(5) \\
\text{F1F2}(1,12) &= a(6,1)^2 * b(7,2)^2 * (1/12.) + a(6,2)^2 * b(7,3)^2 * (1/4.) \\
\text{delE}(1,12) &= \text{ED}(7,6) && \& \text{rhoOD2}(1,12)=\text{rho0}(6) \\
\text{F1F2}(1,13) &= a(7,1)^2 * b(7,2)^2 * (1/12.) + a(7,2)^2 * b(7,3)^2 * (1/4.) \\
\text{delE}(1,13) &= \text{ED}(7,7) && \& \text{rhoOD2}(1,13)=\text{rho0}(7) \\
\text{F1F2}(1,14) &= a(6,1)^2 * b(8,2)^2 * (1/12.) + a(6,2)^2 * b(8,3)^2 * (1/4.) \\
\text{delE}(1,14) &= \text{ED}(8,6) && \& \text{rhoOD2}(1,14)=\text{rho0}(6) \\
\text{F1F2}(1,15) &= a(7,1)^2 * b(8,2)^2 * (1/12.) + a(7,2)^2 * b(8,3)^2 * (1/4.) \\
\text{delE}(1,15) &= \text{ED}(8,7) && \& \text{rhoOD2}(1,15)=\text{rho0}(7) \\
\text{F1F2}(1,16) &= a(6,1)^2 * b(9,2)^2 * (1/12.) + a(6,2)^2 * b(9,3)^2 * (1/4.) \\
\text{delE}(1,16) &= \text{ED}(9,6) && \& \text{rhoOD2}(1,16)=\text{rho0}(6) \\
\text{F1F2}(1,17) &= a(7,1)^2 * b(9,2)^2 * (1/12.) + a(7,2)^2 * b(9,3)^2 * (1/4.) \\
\text{delE}(1,17) &= \text{ED}(9,7) && \& \text{rhoOD2}(1,17)=\text{rho0}(7)
\end{aligned}$$

```

F1F2(1,18) = a(6,1)^2* b(10,2)^2* (1/12.)+ a(6,2)^2* b(10,3)^2*(1/4.)
delE(1,18) = ED(10,6)      &   rhoOD2(1,18)=rho0(6)
F1F2(1,19) = a(7,1)^2* b(10,2)^2* (1/12.)+ a(7,2)^2* b(10,3)^2*(1/4.)
delE(1,19) = ED(10,7)      &   rhoOD2(1,19)=rho0(7)
F1F2(1,20) = b(11,2)^2* (1/12.) & delE(1,20) = ED(11,8)      &
rhoOD2(1,20)=rho0(8)
F1F2(1,21) = b(12,2)^2* (1/12.) & delE(1,21) = ED(12,8)      &
rhoOD2(1,21)=rho0(8)
F1F2(1,22) = b(13,2)^2* (1/12.) & delE(1,22) = ED(13,8)      &
rhoOD2(1,22)=rho0(8)

return
end

```

```

PRO Hamiltonian2X1_2, muBB, gImuNB, AJ, BJ, E1_2, B1_2
;this procedure calculates the eigenvalues and eigenstate coefficients
;for the 2S1/2 and 2P1/2 states
;Energy eigenstate |mI,mJ>

H      = replicate(0.0,9,9) ; Hamiltonian
E1_2   = replicate(0.0,9)   ; eigenvalues
B1_2   = replicate(0.0,9,4)  ; associated eigenstate coefficients
; have only 8x8 quantum matrix but
; we won't use the H(i,j) where i = 0 and/or j = 0

; have to diagonalize (2,3) and (4,5) and (6,7)
; this will be done using an IDL function EIGENQL:
; Result = EIGENQL( A [, /ABSOLUTE] [, /ASCENDING] [, /DOUBLE]

```

```

;          [, EIGENVECTORS=variable] [, /OVERWRITE | , RESIDUAL=variable] )
; the EIGENVECTORS keyword is set equal to a named variable that will contain the
computed
; eigenvectors in an n-by-n array. The ith row of the returned array
; contains the ith eigenvector.

```

```
H(1,1) = 0.5*muBB -1.5*gImuNB +(3/4.)*AJ
```

```
E1_2(1) = H(1,1)
```

```
H(2,2) = -0.5*muBB -1.5*gImuNB -(3/4.)*AJ
```

```
H(3,2) = AJ * 0.5 * sqrt(3.)      &   H(2,3) = H(3,2)
```

```
H(3,3) = (1/4.)*AJ + (1/2.)*muBB -0.5*gImuNB
```

```
A          = fltarr(2,2) ; dummy matrix to pass to EIGENQL
```

```
for i = 0, 1 do begin                ; 2 by 2
```

```
for j = 0, 1 do A(i,j) = H(i+2,j+2)
```

```
endfor
```

```
Eigenval = EIGENQL( A, EIGENVECTORS= Vect) ; default is descending eigenvalues
```

```
E1_2(2:3) = Eigenval
```

```
for i = 0, 1 do B1_2(i+2,1:2) = Vect(*,i)
```

```
; second index of Vect specifies which eigenvector
```

```
H(4,4) = -(1/4.)*AJ - (1/2.)*muBB -0.5*gImuNB
```

```
H(5,4) = AJ                &   H(4,5) = H(5,4)
```

```
A          = fltarr(2,2)
```

```
H(5,5) = -(1/4.)*AJ      + (1/2.)*muBB +0.5*gImuNB
```

```

for i = 0, 1 do begin
; 2 by 2
for j = 0, 1 do A(i,j) = H(i+4,j+4)
endfor

Eigenval = EIGENQL( A, EIGENVECTORS= Vect) ; default is descending eigenvalues
E1_2(4:5) = Eigenval

for i = 0, 1 do B1_2(i+4,1:2) = Vect(*,i)

H(6,6) = +(1/4.)*AJ - (1/2.)*muBB +0.5*gImuNB
H(7,6) = AJ * 0.5 * sqrt(3.) & H(6,7) = H(7,6)
H(7,7) = -(3/4.)*AJ + (1/2.)*muBB +1.5*gImuNB
A = fltarr(2,2)

for i = 0, 1 do begin
; 2 by 2
for j = 0, 1 do A(i,j) = H(i+6,j+6)
endfor

Eigenval = EIGENQL( A, EIGENVECTORS= Vect) ; default is descending eigenvalues
E1_2(6:7) = Eigenval

for i = 0, 1 do B1_2(i+6,1:2) = Vect(*,i)

H(8,8) = (3/4.)*AJ - (1/2.)*muBB +1.5*gImuNB
E1_2(8) = H(8,8)

return

end

PRO Hamiltonian2P3_2, muBB, gImuNB, AJ, BJ, EP3_2, B3_2, flag
;this procedure calculates the eigenvalues and eigenstate coefficients
;for the 2P3/2 state
;Energy eigenstate |mI,mJ>

```

```

H      =  replicate(0.0,17,17) ; Hamiltonian
EP3_2  =  replicate(0.0,17)      ; eigenvalues
B3_2   =  replicate(0.0,17,4)    ; associated eigenstate coefficients
; have only 16x16 quantum matrix but
; we won't use the H(i,j) where i = 0 and/or j = 0

; must diagonalize (2,3) and (4,5,6) and (7,8,9,10) and (11,12,13) and (14,15)
; this will be done using an IDL function EIGENQL:
; Result = EIGENQL( A [, /ABSOLUTE] [, /ASCENDING] [, /DOUBLE]
;               [, EIGENVECTORS=variable] [, /OVERWRITE | , RESIDUAL=variable] )
; the EIGENVECTORS keyword is set equal to a named variable that will contain the
computed
; eigenvectors in an n-by-n array. The ith row of the returned array
; contains the ith eigenvector.

H(1,1)  = 2.*muBB-(3/2.)*gImuNB +(9/4.)*AJ +(1/4.)*BJ
EP3_2(1) = H(1,1)

H(2,2) = (2/3.)*muBB-(3/2.)*gImuNB+(3/4.)*AJ-(1/4.)*BJ
H(3,2) = (1.5*AJ +0.5*BJ) * flag          &      H(2,3) = H(3,2)
H(3,3) = 2.*muBB-(1/2.)*gImuNB+(3/4.)*AJ-(1/4.)*BJ

A      = fltarr(2,2) ; Dummy matrix to send to EIGENQL
for i = 0, 1 do begin          ; 2 by 2

```

```

for j = 0, 1 do A(i,j) = H(i+2,j+2)
endfor

Eigenval  = EIGENQL( A, /Ascending, EIGENVECTORS= Vect)
EP3_2(2:3) = Eigenval

for i = 0, 1 do B3_2(i+2,2:3) = Vect(*,i)
; second index of Vect specifies which eigenvector

H(4,4) = -(2/3.)*muBB-(3/2.)*gImuNB-(3/4.)*AJ-(1/4.)*BJ
H(5,4) = AJ*Sqrt(3.) * flag           &   H(4,5) = H(5,4)
H(5,5) = (2/3.)*muBB-(1/2.)*gImuNB+(1/4.)*AJ+(1/4.)*BJ
H(6,4) = BJ/2. * flag                 &   H(4,6) = H(6,4)
H(6,5) = AJ*Sqrt(3.) * flag           &   H(5,6) = H(6,5)
H(6,6) = 2.*muBB+(1/2.)*gImuNB-(3/4.)*AJ-(1/4.)*BJ

A      = fltarr(3,3)
for i   = 0, 2 do begin                ; 3 by 3
for j = 0, 2 do A(i,j) = H(i+4,j+4)
endfor

Eigenval  = EIGENQL( A, /Ascending, EIGENVECTORS= Vect)
EP3_2(4:6) = Eigenval

for i = 0, 2 do B3_2(i+4,1:3) = Vect(*,i)

H(7,7) = -2.*muBB-(3/2.)*gImuNB-(9/4.)*AJ+(1/4.)*BJ
H(8,8) = -(2/3.)*muBB-(1/2.)*gImuNB-(1/4.)*AJ+(1/4.)*BJ
H(9,9) = (2/3.)*muBB+(1/2.)*gImuNB-(1/4.)*AJ+(1/4.)*BJ

```

```

H(10,10)= 2.*muBB+(3/2.)*gImuNB-(9/4.)*AJ+(1/4.)*BJ
H(8,7) = (1.5*AJ-0.5*BJ) * flag      & H(7,8) =H(8,7)
H(9,7) = BJ/2. * flag                & H(7,9) =H(9,7)
H(10,7) = 0.                        & H(7,10) =H(10,7)
H(9,8) = 2.*AJ * flag                & H(8,9) =H(9,8)
H(10,8) = BJ/2. * flag                & H(8,10) =H(10,8)
H(10,9) = (1.5*AJ-0.5*BJ) * flag     & H(9,10) =H(10,9)

A      = fltarr(4,4)
for i   = 0, 3 do begin                ; 4 by 4
for j   = 0, 3 do A(i,j) = H(i+7,j+7)
endfor

Eigenval = EIGENQL( A, /Ascending, EIGENVECTORS= Vect)
EP3_2(7:10) = Eigenval
for i = 0, 3 do B3_2(i+7,0:3) = Vect(*,i)

H(11,11) = -2*muBB-(1/2.)*gImuNB-(3/4.)*AJ-(1/4.)*BJ
H(12,12) = -(2/3.)*muBB+(1/2.)*gImuNB+(1/4.)*AJ+(1/4.)*BJ
H(13,13) = (2/3.)*muBB+(3/2.)*gImuNB-(3/4.)*AJ-(1/4.)*BJ
H(12,11) = AJ*Sqrt(3.) * flag          & H(11,12) =H(12,11)
H(13,11) = BJ/2 * flag                 & H(11,13) =H(13,11)
H(13,12) = AJ*Sqrt(3.) * flag          & H(12,13) =H(13,12)

A      = fltarr(3,3)
for i   = 0, 2 do begin                ; 3 by 3
for j   = 0, 2 do A(i,j) = H(i+11,j+11)

```

```

endfor

Eigenval      = EIGENQL( A, /Ascending, EIGENVECTORS= Vect)
EP3_2(11:13) = Eigenval

for i = 0, 2 do B3_2(i+11,0:2) = Vect(*,i)

H(14,14) = -2*muBB+(1/2.)*gImuNB+(3/4.)*AJ-(1/4.)*BJ
H(15,15) = -(2/3.)*muBB+(3/2.)*gImuNB+(3/4.)*AJ-(1/4.)*BJ
H(15,14) = (1.5*AJ+0.5*BJ) * flag      & H(14,15) =H(15,14)

A          = fltarr(2,2)
for i      = 0, 1 do begin                ; 2 by 2
for j      = 0, 1 do A(i,j) = H(i+14,j+14)
endfor

Eigenval    = EIGENQL( A, /Ascending, EIGENVECTORS= Vect)
EP3_2(14:15) = Eigenval

for i = 0, 1 do B3_2(i+14,0:1) = Vect(*,i)

H(16,16)    = -2*muBB+(3/2.)*gImuNB+(9/4.)*AJ+(1/4.)*BJ
EP3_2(16)   = H(16,16)

return

END

;Voigt and Complex Error Function
; w(z)      = Faddeeva fn, complex probability fn, plasma dispersion fn
; w(z)      = (i/pi)Integral-inf to inf exp(-t*t)/(z - t) dt

```



```

; for z = x + i y and w(z)          = K(x,y) + i L(x,y)
; K(x,y) = (y/pi) Integral-inf to inf exp(-t*t)/((x - t)^2+y^2) dt
; K(x,y) = Voigt(y,x) in IDL library **NOTE the order of the arguments**

;A Comparison of Computational Methods
;F. Schreier; J. Quant. Spectros. Radiat. Transfer 48, 743-762 (1992)
;Abstract
;Several computational procedures for the Voigt function and complex error
; function are discussed and compared with respect to accuracy and
; running time. Vectorization of the codes is applied where possible.
; Computational speed varied over two orders of magnitude. Even without
; vectorization, restructuring of the source code can yield a significant
; acceleration. The computational effort for Fourier transform methods
; is estimated and compared with other methods. For applications involving
; least-squares-fitting the evaluation of the complex error function
; provides an efficient way to calculate both the Voigt function and its
; partial derivatives.
;The Optimized Humlicek w4 Algorithm

FUNCTION APPROX1, T
return, (T * .5641896) / (.5 + (T * T))
end

FUNCTION APPROX2, T,U
return, (T * (1.410474 + U*.5641896))/ (.75 + (U *(3.+U)))
end

FUNCTION APPROX3, T
return, ( 16.4955 + T * (20.20933 + T * (11.96482 +

```

```

T * (3.778987 + 0.5642236*T))))          $
/ ( 16.4955 + T * (38.82363 + T *          $
(39.27121 + T * (21.69274 + T * (6.699398 + T))))))
end

FUNCTION APPROX4, T,U
return, (T * (36183.31 - U * (3321.99 - U * (1540.787 - U          $
*(219.031 - U *(35.7668 - U *(1.320522 - U * .56419)))))) $
/ (32066.6 - U * (24322.8 - U * (9022.23 - U * (2186.18          $
- U * (364.219 - U * (61.5704 - U * (1.84144 - U))))))))))
end

PRO HUMLICEK, X,Y, PRBFCT
;*
;*      complex probability function for complex argument Z=X+iY      *
;*      real part = voigt function K(x,y)                               *
;*
;*      source:   j. humlicek, JQSRT 27, 437, 1982                     *
;*
;*      parameters:                                                    *
;*      NX      number of grid points = NX+1                          in *
;*      X      array of grid points                                    in *
;*      Y      Voigt function parameter, ratio of lorentz/doppler    in *
;*      PRBFCT complex array of function values                       out *
;*
;*      the stated accuracy is claimed to be 1.0E-04 by the author.   *
;*      r h norton has checked the accuracy by comparing values       *
;*      computed using a program written by b.h.armstrong, and        *

```

```

;*      the accuracy claim seems to be warranted.          *
;*                                                         *
;*****fgs 12/91*
NX      =      N_ELEMENTS(X) -1
PRBFCT  =      COMPLEXARR( N_ELEMENTS(X) )
IF (Y ge 15.) THEN begin          ;all points are in region I
For I=0,NX do begin                ; 100
T          = Complex(Y,-X(I))
PRBFCT(I) = APPROX1(T)
endfor                                ; 100
endif
IF ((Y lt 15.) and (Y ge 5.5)) THEN begin ;points are in region I or region II
For I=0,NX do begin                ; 200
T = Complex(Y,-X(I))
S = ABS(X(I)) + Y
IF (S ge 15.) THEN PRBFCT(I) = APPROX1(T)
if (s lt 15.) then begin
U      = T * T
PRBFCT(I) = APPROX2(T,U)
ENDIF
endfor                                ;200
endif
IF ((Y lt 5.5) and (Y ge 0.75)) THEN begin
for I=0,NX do begin                ;300
T = Complex(Y,-X(I))
S = ABS(X(I)) + Y
IF ( S ge 15. ) THEN PRBFCT(I) = APPROX1(T)

```

```

IF ( (S ge 5.5) and (S lt 15.) ) then begin
U      = T * T
PRBFCT(I) = APPROX2(T,U)
ENDIF

IF (S lt 5.5) THEN      PRBFCT(I) = APPROX3(T)

endfor

endif      ;300

if (Y lt 0.75 ) THEN begin
FOR I=0,NX do begin      ;400
T = Complex(Y,-X(I))
AX = ABS(X(I))
S = AX + Y

IF (S ge 15.0) THEN PRBFCT(I)= APPROX1(T)      ;region I
IF ((S lt 15.0) and (S ge 5.5) ) THEN begin      ;region II
U = T * T
PRBFCT(I)= APPROX2(T,U)

endif

IF ((S lt 5.5) and (Y ge (0.195*AX-0.176)) ) THEN $
PRBFCT(I)= APPROX3(T)      ;region III
IF ((S lt 5.5) and (Y lt (0.195*AX-0.176)) ) THEN begin      ;region IV
U = T * T
PRBFCT(I)= EXP(U) - APPROX4(T,U)

ENDIF

endfor      ;400

ENDIF

IF (Y EQ 0.0) THEN begin
for I=0,NX do begin

```

```

PRBFCT(I) = complex( EXP(-X(I)^2), IMAGINARY(PRBFCT(I)) )
endfor
endif
RETURN
END

; main program
COMMON Const
;set directory to save output text files
cd, 'C:\Users\NS-2R\My Documents\CIRES\Atomic Filters\FADOF\IDL\Outputs\DEMOF\'
extension = 'test'
print, 'files will be saved with the name "Faraday+extension"'
read, ' what extension do you want for output files? ', extension
journal, 'JAFaraday'+extension

call_Procedure, 'Constants' ;prepare variables used across the program

;calculate for each isotope (if Na, loop stops after 1 iteration)

;first prepare arrays
NumNu = 1201 ;number of 25 MHz steps for calc-- 1201 goes from -15 to +15
GHz
nuobs = .025 * ( INDGEN(NumNu) - (NumNu-1)/2. ) ;GHz-- 25MHz steps

chiD1 = COMPLEXARR(2,NumNu,2) ; complex susceptibility for two circular
polarizations and two isotopes
a1D1 = fltarr(NumNu) & a2D1 = fltarr(NumNu)

```

```

ddD1    = fltarr(NumNu)      & TrD1 = fltarr(NumNu)

TrbackD1= fltarr(NumNu)

chiD2    = COMPLEXARR(2,NumNu,2) ; complex susceptibility for two circular
polarizations and two isotopes

a1D2    = fltarr(NumNu)      & a2D2 = fltarr(NumNu)
ddD2    = fltarr(NumNu)      & TrD2 = fltarr(NumNu)
TrD2M   = fltarr(NumNu)      & TrD2P = fltarr(NumNu)
TrD2Faraday = fltarr(NumNu)
TrbackD2= fltarr(NumNu)

chiD1iso  = COMPLEXARR(2, NumNu) ;total susceptibility
chiD2iso  = COMPLEXARR(2, NumNu)

for iso=0,1 do begin ; loop over isotope
if abundance(iso) eq 0.0 then BREAK ;loop iterates only once for Na
; calc energies of ground state 2S1_2
call_Procedure, 'Hamiltonian2X1_2', gmuBBS1_2, gImuNB(iso), AJ2S1_2(iso),
BJ1_2(iso), ES1_2, BS1_2
; calc energies of excited state 2P1_2
call_Procedure, 'Hamiltonian2X1_2', gmuBBP1_2, gImuNB(iso), AJ2P1_2(iso),
BJ1_2(iso), EP1_2, BP1_2
; calc energies of excited state 2P3_2
call_Procedure, 'Hamiltonian2P3_2', gmuBBP3_2, gImuNB(iso), AJ2P3_2(iso),
BJ2P3_2(iso),      $
EP3_2, BP3_2, flag

;calculate density weighting factor
call_Procedure, 'denweight', ES1_2, kBoltz, hPlanck, tempV, rho0

```

```

; calc energy differences for D1
ED1      = fltarr(9,9)
for iex = 0, 8 do ED1(iex,*) = EP1_2(iex) - ES1_2(*)

; calc F1F2, delE, and rho0 for 12 sigma- and 12 sigma+ transitions of D1
call_Procedure, 'F1F2delED1', BS1_2, BP1_2, ED1, rho0, F1F2D1, delED1, rho0D1

for inu = 0, NumNu-1 do begin
for isig = 0, 1 do begin ; =0 for sigma- and =1 for sigma+
; sum over all 12 transitions
Integ = ComplexVoigt( delED1(isig,*), nuobs(inu), nuDopplerD1(iso), gammaD1)
for ichan = 1, 12 do begin
chiD1(isig, inu, iso) = chiD1(isig, inu, iso) +
rho0D1(isig, ichan)*F1F2D1(isig, ichan) *Integ(ichan)
endfor
chiD1(isig, inu, iso)=constD1(iso)*chiD1(isig, inu, iso)*abundance(iso)
endfor ; loop on isigma
endfor ; loop on freq

; calc energy differences for D2
ED2      = fltarr(17,9)
for iex = 0, 16 do ED2(iex,*) = EP3_2(iex) - ES1_2(*)

; calc F1F2 and delE for 22 sigma- and 22 sigma+ transitions of D2
call_Procedure, 'F1F2delED2', BS1_2, BP3_2, ED2, rho0, F1F2D2, delED2, rho0D2
;for calculating chi and transmission, see slides 11 and 12

```

```

for inu = 0, NumNu-1 do begin
for isig = 0, 1 do begin ; =0 for sigma- and =1 for sigma+
Integ = ComplexVoigt(deLED2(isig,*), nuobs(inu), nuDopplerD2(iso), gammaD2)
for ichan = 1, 22 do begin
chiD2(isig,inu, iso) = chiD2(isig,inu, iso) +
rho0D2(isig,ichan)*F1F2D2(isig,ichan) *Integ(ichan)
endfor
chiD2(isig, inu, iso)=constD2(iso)*chiD2(isig, inu, iso)*abundance(iso)
endfor ; loop on isigma
endfor ; loop on freq of observation inu
endfor ; loop on iso

```

;calculate isotope weighted chi

```
chiD1iso(0, *) = chiD1(0, *, 0) + chiD1(0, *, 1)
```

```
chiD1iso(1, *) = chiD1(1, *, 0) + chiD1(1, *, 1)
```

```
chiD2iso(0, *) = chiD2(0, *, 0) + chiD2(0, *, 1)
```

```
chiD2iso(1, *) = chiD2(1, *, 0) + chiD2(1, *, 1)
```

```
for inu=0, NumNu-1 do begin ;calculate D1 and D2 transmissions
```

```
;a1D1, a2D1, ddD1 are used to break up the calculation steps
```

```
a1D1(inu) = (!pi/LambdaD1)* Length*1.e7 * IMAGINARY( chiD1iso(1,inu) +
chiD1iso(0,inu) )
```

```
a2D1(inu) = (!pi/LambdaD1)* Length*1.e7 * IMAGINARY( chiD1iso(1,inu) -
chiD1iso(0,inu) )
```



```
ddD1(inu) = (!pi/LambdaD1)* Length*1.e7 * REAL_PART( chiD1iso(1,inu) -
chiD1iso(0,inu) )
```

;TrD1 is the transmission of light through two crossed polarizers (ie, Faraday filter)

;see eq. 15

```
TrD1(inu) = 0.25 * exp(-a1D1(inu)) * $
( exp(-a2D1(inu)) + exp(a2D1(inu)) -2.*cos(ddD1(inu)) )
```

;TrbackD1 is the transmission if the polarizers are parallel

```
TrbackD1(inu) = 0.25 * exp(-a1D1(inu)) * $
( exp(-a2D1(inu)) + exp(a2D1(inu)) +2.*cos(ddD1(inu)) )
```

; a1D2, a2D2, ddD2 are used to break up the calculation steps

```
a1D2(inu) = (!pi/LambdaD2)* Length*1.e7 * IMAGINARY( chiD2iso(1,inu) +
chiD2iso(0,inu) )
```

```
a2D2(inu) = (!pi/LambdaD2)* Length*1.e7 * IMAGINARY( chiD2iso(1,inu) -
chiD2iso(0,inu) )
```

```
ddD2(inu) = (!pi/LambdaD2)* Length*1.e7 * REAL_PART( chiD2iso(1,inu) -
chiD2iso(0,inu) )
```

;TrD2 is the transmission of light through two crossed polarizers (ie, Faraday filter)

;see eq. 15

```
TrD2(inu) = 0.25 * exp(-a1D2(inu)) * $
( exp(-a2D2(inu)) + exp(a2D2(inu)) -2.*cos(ddD2(inu)) )
```

;TrbackD2 is the transmission if the polarizers are parallel

```
TrbackD2(inu) = 0.25 * exp(-a1D2(inu)) * $
```

```

( exp(-a2D2(inu)) + exp(a2D2(inu)) +2.*cos(ddD2(inu)) )
endfor

;Faraday Rotation=dd/2 , to write in units of pi, Faraday Rotation=dd/(2*pi)
;see equation 5 and definition of dd above
FrotD1 = ddD1/(2*pi)
FrotD2 = ddD2/(2*pi)

openw, u10, 'Faraday'+extension, /Get_Lun
title = ' nuobs REchiD1- IMchiD1- REchiD1+ IMchiD1+ a1D1 a2D1 ddD1 FrotD1 TrD1
TrbackD1 '
title = title +'REchiD2- IMchiD2- REchiD2+ IMchiD2+ a1D2 a2D2 ddD2 FrotD2 TrD2
TrbackD2 '
form1= '(21(1x,e16.8))' ;format for values in output file
;print header on output file with information about vapor properties
if atom eq 'N 'then printf, u10, 'Faraday Filter Parameters for Sodium'
if atom eq 'K 'then printf, u10, 'Faraday Filter Parameters for Potassium'
printf, u10, 'Calculated with FaradayFilter3.pro'
printf, u10, 'Vapor Length (cm) ', Length
printf, u10, 'Magnetic Field (G) ', Bfield
printf, u10, 'Cell Temperature (K) ', tempV
printf, u10, 'Tip Temperature (K) ', tempP
;now print colum headings
printf, u10, title
;print data
for inu = 0, NumNu-1 do begin
printf, u10, format = form1, nuobs(inu), chiD1iso(0,inu), chiD1iso(1,inu), $

```

```

a1D1(inu), a2D1(inu), ddD1(inu), FrotD1(inu), TrD1(inu), TrbackD1(inu),$
chiD2iso(0,inu), chiD2iso(1,inu),$
a1D2(inu), a2D2(inu), ddD2(inu), FrotD2(inu), TrD2(inu), TrbackD2(inu)
endfor
free_Lun, u10
journal
print, "That's all folks!"

; Added by Wentao for NaDEMOF transmission calculation of D2
; Set each channel's input as 1 here
inu = 0
for inu=0, NumNu-1 do begin ;calculate transmissions
; - circular polarization
TrD2M(inu) = 1 * exp(-2 * (!pi/LambdaD2)* Length*1.e7 * IMAGINARY(chiD2iso(0,inu))
)
; + circular polarization
TrD2P(inu) = 1 * exp(-2 * (!pi/LambdaD2)* Length*1.e7 * IMAGINARY(chiD2iso(1,inu))
)
endfor

; Added by Wentao for Faraday filter transmission calculation of D2 On 20130916
inu = 0
for inu=0, NumNu-1 do begin ;calculate D2 transmission only
; Transmissin
;TrD2Faraday(inu) = 1/4 * (exp(-2 * (!pi/LambdaD2)* Length*1.e7 *
IMAGINARY(chiD2iso(0,inu))) + exp(-2 * (!pi/LambdaD2)* Length*1.e7 *
IMAGINARY(chiD2iso(1,inu))) - 2 * exp(-(!pi/LambdaD2)* Length*1.e7 *

```

```

(IMAGINARY(chiD2iso(0, inu))+IMAGINARY(chiD2iso(1, inu)))) * cos(!pi/LambdaD2)*
Length*1.e7 *(chiD2iso(0, inu)-chiD2iso(1, inu)))
TrD2Faraday(inu) = (exp(-2 * (!pi/LambdaD2)* Length*1.e7 *
IMAGINARY(chiD2iso(0, inu))) + exp(-2 * (!pi/LambdaD2)* Length*1.e7 *
IMAGINARY(chiD2iso(1, inu)))) - 2 * exp(-(!pi/LambdaD2)* Length*1.e7 *
(IMAGINARY(chiD2iso(0, inu))+IMAGINARY(chiD2iso(1, inu)))) * cos(!pi/LambdaD2)*
Length*1.e7 *(REAL_PART(chiD2iso(0, inu))-REAL_PART(chiD2iso(1, inu)))))/4
; Faraday rotation

endfor

openw, u3, 'NaDEMOF'+extension, /Get_Lun
title = ' nuobs TrD2- TrD2+ TrD2Faraday'
form1= '(21(1x,e16.8))' ;format for values in output file
;print header on output file with information about vapor properties
if atom eq 'N 'then printf, u3, '%NaDEMOF Parameters for Sodium'
printf, u3, '%Calculated with NaFaradayFilter.pro'
printf, u3, '%Vapor Length (cm) ', Length
printf, u3, '%Magnetic Field (G) ', Bfield
printf, u3, '%Cell Temperature (K) ', tempV
printf, u3, '%Tip Temperature (K) ', tempP
;now print colum headings
printf, u3, '% ', title
;print data
for inu = 0, NumNu-1 do begin
printf, u3, format = form1, nuobs(inu), TrD2M(inu), TrD2P(inu), TrD2Faraday(inu)
endfor

```

```
free_Lun, u3

; Plot the stuff
window,10
plot, nuobs, TrD2P
oplot, nuobs,TrD2M

; Plot the stuff
window,11
plot, nuobs, TrD2Faraday

; Plot the stuff
FaradayPlot = plot(nuobs, TrD2Faraday,TITLE='Faraday Filter Transmission', $
XTITLE='Frequency Offset (GHz)', YTITLE='Transmission', XRANGE=[-10,10])
FaradayPlot.Save, "Faraday.png", BORDER=10, RESOLUTION=300, /TRANSPARENT

end
```